Doctoral Dissertation
Doctoral Program in Energy Engineering (29th Cycle)

Alternative fuels and combustion modes to lower pollutant emissions from conventional internal combustion engines

By

Daniele Iemmolo

******

Supervisor(s):
Prof. Ezio Spessa. ,Supervisor
Prof. Daniela Misul Supervisor

Doctoral Examination Referees:
Prof. Michal Vojtíšek, PhD , Referee, Czech Technical University of Prague
Dr. Simona Silvia Merola, PhD. , Referee, Istituto Motori - CNR

Politecnico di Torino
2017

Declaration

I hereby declare that, the contents and organization of this dissertation constitute my own original work and does not compromise in any way the rights of third parties, including those relating to the security of personal data.

Daniele Iemmolo

2017

* This dissertation is presented in partial fulfillment of the requirements for **Ph.D. degree** in the Graduate School of Politecnico di Torino (ScuDo).

I would like to dedicate this thesis to my loving parents, friends and colleagues.

Acknowledgment

I would like to acknowledge Centro Ricerche Fiat and FPT Industrial for the financial and technical support that has been provided during the research activity.

Abstract

The present thesis covers the utilization of alternative fuels and combustion modes in production internal combustion engines to face the problem of pollution and energy diversification in the automotive sector. In particular, the first part deals with alternative fuels in conventional combustion mode in spark-ignition engines, whereas the second part concerns conventional diesel fuel with non-conventional PCCI combustion mode in compression-ignition engines.

More into details, the first part pertains to the usage of alternative fuels with conventional combustion in spark-ignition internal combustion engines, such as bio-gas and hydrogen-enriched compressed natural gas and, in particular, with the need to identify which kind of fuel blend is present in the vehicle tank, since engine performance and emission strongly depends on the fuel mixture composition being fed to the engine.

The production of hydrogen enriched compressed natural gas from biomass results in a wide range of possible gas mixtures, having a strong impact on engine performance and emissions. The research work conducted in the first part of this thesis focused on finding an algorithm capable of identifying which mixture is actually injected into the engine starting from data readily available from the engine control unit. The scenario in which the vehicle is fueled at the gas station with an unknown mixture composition has been replicated on test bench by using different fuels. Data acquired were used to build and validate the recognition method. Given a possible set of mixtures, the algorithm computes the relevant thermo-physical properties and using data from the engine control unit, like air-mass flow at the intake, estimates an injection duration. A subset of the sample blends that represents the possible variety of mixtures that could be present in the vehicle tank has been chosen. The mixture that shows the minimum error in terms of injection duration, from a comparison of the estimated injection duration with the one actuated by the engine control unit, is then identified as the actual one. The algorithm showed a

very good prediction capability with the test fuel blends, with a maximum uncertainty of 5% on hydrogen content on HCNG blends. The recognition algorithm converges after less than 10 different engine working conditions, expressed in terms of speed and load. The candidate set has been extended to a full factorial set of 2 million blends, to validate the ability of the recognition method to correctly match the real fuel.

The second part is devoted to the study of a premixed-charge compression ignition (PCCI) combustion mode in a 3.0L Euro VI heavy-duty diesel production engine, focusing on statistical techniques exploited to optimize pollutant emissions and performance. Furthermore, a preliminary study of pressure-based combustion control technique has been conducted to evaluate if it has all the necessary features to be implemented during PCCI operations.

This kind of non-conventional combustion has been achieved by anticipating the start of injection and recirculating high amounts of exhaust gas in the intake manifold. The result is a highly premixed and diluted charge, which lowers significantly the in-cylinder temperature during the combustion, thus avoiding the formation of soot and of nitrogen oxides in the charge. As a first step, preliminary tests have been run on different engine working points, in order to identify which control variables are the most influential and in which range they can be varied to achieve the PCCI conditions. As a second step, an experimental campaign has been conducted, following a Design of Experiment (DoE) approach. Based on these results, quadratic regression models have been fitted. The models have been then validated on experimental points, providing a good prediction capability. As a last step, single-objective and multi-objective optimizations have been performed, in order to find a proper combination of the input factors that satisfied the desired values for the outputs. Optimal points have been experimentally replicated and compared to the standard engine calibration. A strong reduction (up to 94%) of NO_x and soot has been observed, while penalties in CO and HC (up to 10 times compared to the standard calibration), bsfc (up to 13%), and CN have been noticed. The increment in CO and HC can be addressed by using a proper after-treatment system, while bsfc and CN represent the major drawbacks of this kind of combustion. Aiming to further optimize and control the combustion process, preliminary tests implementing a pressure-based approach to control the phasing of the combustion have been run in PCCI mode, showing good potentialities, especially as far as cyclic and cylinder-to-cylinder variation are concerned.

Contents

Chapter 1

Introduction

The Paris agreement entered into force in November 2016 and has been signed by the representatives of 195 countries; it represents a milestone in the history of greenhouse gas emissions mitigation, adaption and finance, being the world's first comprehensive climate agreement.

Each individual country has to give a so called "national determined contribution" to achieve the global goal of reducing greenhouse emission and to drive the fossil fuel divestment. The contributions should be reported every 5 years, and each further contributions should be more "ambitious" than the previous one.

In this framework, more and more stringent requirements in terms of greenhouse and pollutants emission have to be expected, so that the research community has been focusing on new kind of solutions to fulfill these goals.

In addition, according to the World Energy Outlook 2016 (WEA 2016) proposed by the International Energy Agency (IEA) [1], the global energy demand will increase sharply in the next years, with Asiatic countries giving a major contribution to this shift (Fig. 1.1). In particular the forecast sees China roughly consuming as much energy as European Union and North America together, with the transportation sector playing the major role on Chinese energy demand in 2040 (Fig. 1.2).

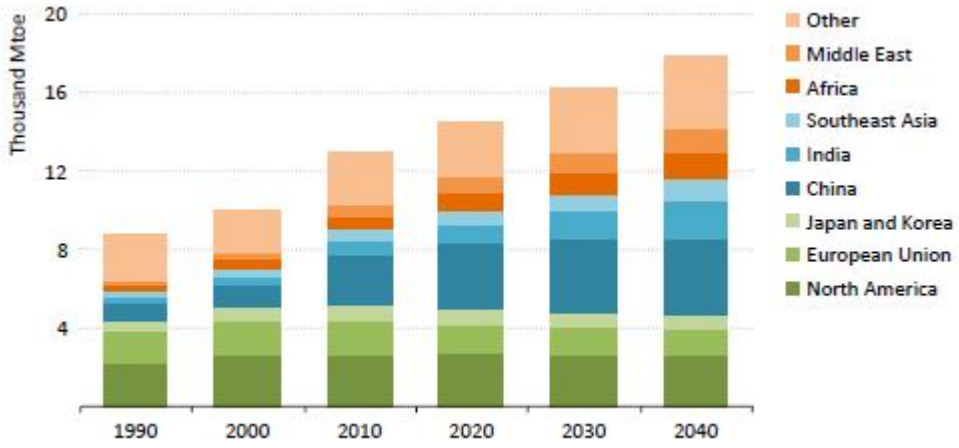

Figure 1.1 - Energy demand by region in the New Policies Scenario according to World Energy Outlook 2016 (WEA 2016) proposed by the International Energy Agency (IEA).

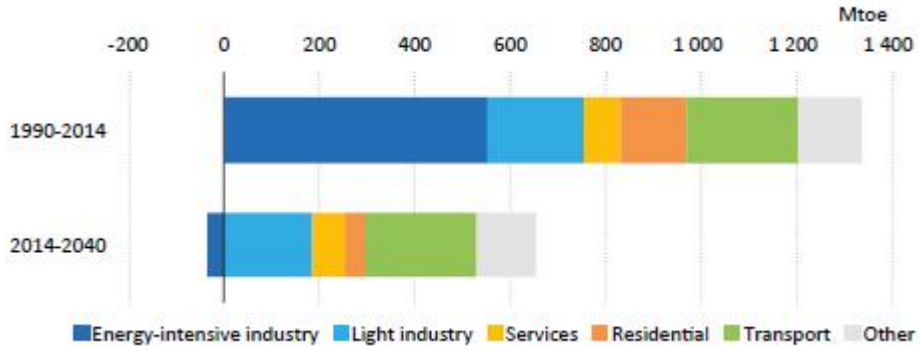

Figure 1.2 - Change in total final consumption in China in the New Policies Scenario according to World Energy Outlook 2016 (WEA 2016) proposed by the International Energy Agency (IEA).

According to the forecasts, renewables and natural gas will experience the most important relative increase in 2040 compared to 2014, but still oil will play the major role (Fig. 1.3).

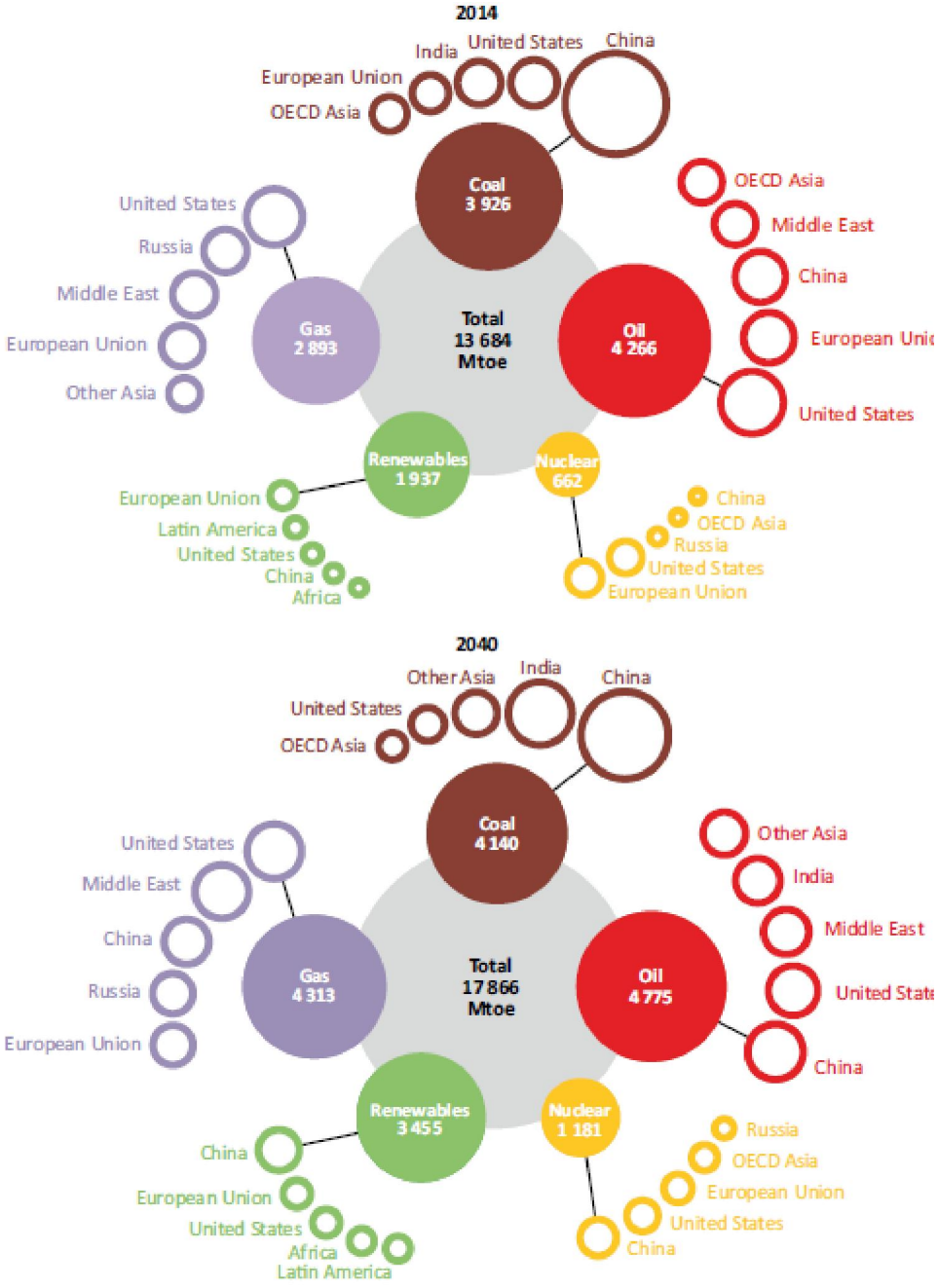

Figure 1.3 – Global primary energy mix in the New Policies Scenario according to World Energy Outlook 2016 (WEA 2016) proposed by the International Energy Agency (IEA).

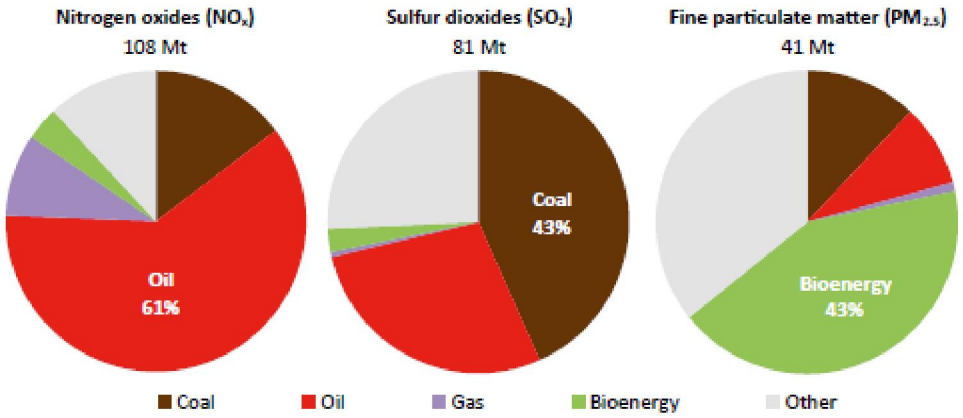

Figure 1.4 – Estimated anthropogenic emissions of the main air pollutants by source in 2015 according to World Energy Outlook 2016 (WEA 2016) proposed by the International Energy Agency (IEA).

It is important to stress that even if the energy mix shift moves the attention on the replacement of carbon sources, since the combustion of oil still represents the main source of pollutants emission in 2015 (Fig. 1.4), strong and innovative solutions on the combustion of oil products still remain an important goal to be achieved.

Among the possible solutions that can be employed in order to fulfill the more stringent demand in terms of pollutant emissions and energy diversification in the transportation sector, the usage of alternative fuels and the application of innovative combustion modes have been extensively investigated and still are under current research.

For the reasons above mentioned, the thesis hereby presented is made up of two main parts that cover issues related to energy diversification in the field of internal combustion engines, with the aim of analyzing and stress some aspects that have been considered really important and worth to be studied in details.

Among the wide range of possible alternatives to petroleum products, hydrogen enriched compressed natural gas (HCNG) and bio-methane are now widely considered as promising fuels, in terms of availability, cost and benefits, when employed in internal combustion engines (ICEs) [2-7]. It is worth to further highlight that the future development of alternative technologies strongly depends on the targets set by the governments in terms of energy saving and environment protection, both on international and local scale [8-10].

The possibility of extracting natural gas from biomass lowers the carbon footprint and prepares the ground for the establishment of a virtuous circle, based on renewable sources. Hydrogen can be derived as a by-product from biomass gasification [11] and it can be added to compressed natural gas (CNG) as an additive. The resulting fuel, referred to as HCNG, has proved to enhance performance and to reduce the overall pollutant and CO_2 exhaust emissions. The high hydrogen speed of flame improves the stability of the combustion process of the enriched blends [12, 13] and allows the lean operation limit to be extended, thus reducing the total exhaust unburned hydrocarbons (THC) and CO [14-16]. Working at leaner air/fuel (A/F) ratios leads to an overall reduction in the CO_2 exhaust emissions and counterbalances the higher NO_x production, which is caused by the augmented combustion temperature induced by the hydrogen addition [17,18]. Moreover, the addition of hydrogen, up to a certain level, increases the brake thermal efficiency, especially when working at lean A/F ratios [19-21]. However, when the H_2 volume fraction in the mixture is considerably increased, knock and backfire can occur, eventually resulting in a degradation of the engine performance [22]. It is worth mentioning that the main drawback of hydrogen as a fuel for ICEs is its low density, which results into a lower volumetric energy content than that of gasoline or methane. Thus, hydrogen enriched blends feature a significantly lower energy content at stoichiometric working conditions [23]. In addition, the iron deposits on the spark plug and cylinder liner are higher for HCNG than for CNG and so is the concentration of wear metals in the lubricating oil [24].

The effect of biogas composition on engine performance has been extensively investigated [25-27]. Along with methane, other inert species, such as carbon dioxide and nitrogen, can be present in a biogas. These species have a significant effect on the engine performance. They affect the engine behavior by reducing the power output as well as the combustion rate and stability [28]. Still, the inert species in natural gas-hydrogen mixtures can decrease the NO_x production and the knock tendency thanks to their dilution effect [29-31].

As mentioned above, one of the main concerns related to the production of biogas is the final composition of the mixture, which largely depends on the production process and on the nature of the biomass: unfortunately, it cannot be generally estimated a priori. Biogas can be produced with different methods and from a wide variety of natural sources [32-34]. In [32,33] a thorough review on biogas production from anaerobic membrane bioreactors is performed, addressing the issues related to the different achieved compositions. Similarly, [34,35] present the research outcomes for biogas production from seagrass and from the petrochemical industry wastewater, respectively. Once more, attention is paid to the varying compositions of the considered blends, which lead to different properties and characteristic. More specifically, different blends will produce different laminar speeds and different knock resistance, hence requiring or at least assessing for different engine control strategies. Considering the potential changes in the methane

number deriving from different compositions, the engine could be possibly downsized and modified to comply with a higher knock resistance. Such modification would require a reinforcement of some of the engine parts and could only be actuated provided that a reliable estimation of the efficiency increase was made. Despite the optimal engine design, researches should address the different strategies to be implemented in the engine control unit (ECU) to comply with the different compositions for a given engine. In fact, this is mostly likely to be the case throughout a national and international gas distribution network.

Therefore, in a foreseen scenario involving different blends of biogas, the recognition of the tank mixture composition after refueling becomes of paramount importance. Thus, the relevant ECU parameters, such as spark advance (SA) and boost pressure, will be properly adjusted. Results of the investigation reported in [36] highlighted the need for a fuel composition recognition methodology: it has been shown that feeding the engine with different gaseous blends, while maintaining the calibration set for CNG, can have an important impact on engine performance. Ideally, after the refueling of a vehicle, the recognition of the fuel mixture should be automatic, fast and readily available. It should rely on parameters available from the ECU, because in order to be cost effective, it should avoid the introduction of additional sensors. Moreover, it should be easy to implement, for any kind of spark-ignition (SI) engine that can be fed with different gaseous fuel blends, from pure methane to mixtures with hydrogen and/or inert species.

The identification of the fuel composition of biodiesel blends has already been addressed in previous works by other authors. In [37], three different methods were compared, using a numerical model of the engine: the first one was based on the estimation of the crankshaft torque, the second one on an exhaust NO_x sensor whereas the third one on a wide band exhaust oxygen sensor (UEGO). Errors of the bio-diesel fraction of 3.1%, 5.9% and 8%, respectively, arouse. A fuel recognition method was presented in [38]. This method was based on the estimation of the mixture fraction, defined as the mass of fuel per total mass of the A/F mixture, and on the exhaust oxygen concentration, as obtained from a UEGO sensor. The results highlighted a poor prediction capability, when the method was applied to evaluate the composition of biodiesel-diesel blends, while better results were achieved using ethanol-gasoline mixtures.

Focusing on gaseous mixtures, a method for the real time estimation of the hydrogen volume content in an SI engine, fueled with HCNG, is reported in [39]. This method is able to discern between three different kinds of mixtures (namely CNG, HCNG with a 30% concentration of H_2 in volume and HCNG with a 40% concentration of H_2 in volume), using the engine speed, and a parameter that represents the command contribution of the A/F ratio control system, as inputs. However, in order to have an acceptable result, the engine should run for at least 10 seconds, with a nearly constant rotational speed above 1200 rpm. Such an operating

mode could be set by the ECU, right after the refueling and the engine crank, by introducing a proper 'recognition phase' so as to force the engine to operate within some given constraints. Elsewise, such mode could be met when all the conditions for a correct mixture recognition by the algorithm are satisfied within a proper time window. The former mode sets important issues about the user experience, the latter makes it difficult to fulfill the fuel recognition conditions, especially when a real urban driving cycle is considered.

It is important to highlight that algorithms to identify the composition of the mixture stored in the vehicle tank are not implemented in standard ECU hardware. Hence, even if the engine can run on different fuels, the ECU is not able to adjust relevant parameters to optimize the combustion process. The lack of an automatic recognition of the fuel blend fed to the engine can pose a serious problem in the development of flexible fuel vehicles, which, according to author knowledge, has not been adequately addressed in previous works.

In the second chapter of the thesis, firstly the influence of difference gaseous blend on engine performance and combustion has been analyzed showing that the same engine calibration, namely a calibration optimized for CNG usage, is not suitable when different fuel blends of hydrogen, methane and inert gases are employed. As a second step an automatic method is proposed for the estimation of the fuel mixture composition before combustion, for test cells and especially for on-board applications. The purpose of this research is to provide a simple and fast method to identify which fuel blend is injected in the engine, relying on readily available ECU parameters. An SI combustion engine has been tested with several gaseous reference fuel blends, under CNG calibration, thus replicating a scenario in which the engine has just been refueled with a mixture of unknown composition. A set of sample gaseous blends has been considered and used as input in a regression model, which estimates the injection duration. Comparing this estimated value with the value set by the ECU under closed-loop lambda control (in order to have a stoichiometric A/F ratio in the engine), an error is calculated, and the mixture that minimizes this quantity can be identified as the one that is being injected.

In the third chapter of the thesis, the implementation of advanced combustion strategies is address. Increasingly stringent regulations concerning pollutant emissions and fuel consumption have stimulated in recent years the exploration of new strategies in internal combustion engine development. Particularly, as diesel engines are concerned, lowering particulate matter (PM) and nitrogen oxides (NOx) exhaust emissions has been a long-standing challenge and still remains a major issue [51].

After-treatment technologies such as selective catalytic reduction (SCR) devices, lean NOx traps (LNTs) and diesel particulate filters (DPFs) have been greatly developed and have proven effective in controlling NOx and soot emissions,

but durability issues, high economic costs and fuel consumption penalties are some of the problems which continue to weaken their widespread adoption.

Therefore, in-cylinder advanced combustion strategies such as Homogeneous Charge Compression Ignition (HCCI) and Premixed Charge Compression Ignition (PCCI) have been widely investigated, in order to simultaneously reduce engine-out NOx and soot emissions and, at the same time, minimize the utilization and the cost of the above-mentioned expensive additional equipment for gas after-treatment [52].

HCCI was one of the first advanced combustion concept to gain the attention of the researcher as an alternative to the conventional diesel process (see Table 3.1). It is based on achieving a homogeneous charge before the auto-ignition, whether injecting the fuel in the intake port or directly in the cylinder, and allowing sufficient time for the air and fuel to mix. Results of early works on this topic highlighted the potentiality to reduce both NO_x and PM emission, raising the possibility of reducing or eliminating after- treatment devices.

The most homogeneous mixture can be achieved when the interval between fuel injection and auto-ignition is as long as possible, i.e. injecting the fuel in the intake port. Even if this approach demonstrated to achieve very low values of NOx and PM, it does not represent a practical solution in modern diesel engines, due to the limited load range achievable, high unburned hydrocarbons emissions as well as high noise. In addition this technology offers a scarce flexibility since the start of combustion is very difficult to control and leads to a trade-off with fuel

efficiency.

Table 3.1 – Overview of some advanced diesel combustion technologies from early HCCI experiments [56].

Acronym	**Meaning**	**Location**
ATAC	Active thermo-atmosphere combustion	Nippon Clean Engine Research Institute
TS	Toyota-Soken combustion	Toyota/Soken
CIHC	Compression-ignited homogeneous charge	University of Wisconsin-Madison
HCCI	Homogeneous charge compression ignition	SwRI
AR, ARC	Active radical combustion	Honda
NADI	Narrow Angle Direct Injection	Institut Français Du Pétrole (IFP)
MK, M-fire	Modulated kinetics	Nissan
PREDIC	Premixed diesel combustion	New ACE
MULDIC	Multiple stage diesel combustion	New ACE
HiMICS	Homogeneous charge intelligent multiple injection combustion system	Hino
UNIBUS	Uniform bulky combustion system	Toyota
PCI	Premixed compression ignited combustion	Mitsubishi

Another approach is to inject the fuel directly in the cylinder, thus allowing more flexibility and opening the possibility to switch to conventional diesel process when the load becomes too high to be sustained. In this case some heterogeneity is introduced in the mixture resulting in a premixed charge, so that this kind of advanced combustion is known as premixed charge compression ignition (PCCI).

PCCI combustion can be achieved by using heavy amount of exhaust gas recirculation (EGR) and advancing or retarding fuel injection timing [52, 54-59]. Under these conditions, the combustion process and, as a consequence, the mechanism of pollutant formation are significantly different compared to conventional diesel combustion mode.

Fig. 3.1 [60] shows the so called Kamimoto-Bae diagram, in which the combustion process pathway is described in terms of local equivalence ratio Φ and local flame temperature. Three different kinds of combustion are highlighted: conventional diesel combustion, an ideal HCCI combustion, and PCCI combustion with direct injection and high EGR rates (often referred to as low-temperature combustion LTC). In conventional combustion the path of a fuel elements encounters the soot formation, the NO_x formation and the soot oxidation area. The formation of soot and its oxidation are visible in the flame luminosity image as orange flames. Ideal HCCI combustion is characterized by a lean and perfectly homogeneous charge, where the local equivalence ratio is the same as the average one. No soot is formed because of the lean mixtures, and the NO_x formation is largely inhibited since the combustion temperature remains low. However this kind of approach has severe consequences in terms of carbon monoxide (CO) and unburned hydrocarbons (HC) exhaust emissions as well as a limited load range. No soot luminosity is observed in this conditions. When PCCI conditions are achieved with high EGR rates, high flame temperatures are avoided so that the combustion process does not pass through soot and NO_x formation zones: no soot luminosity is shows even in this case but just cold 'blue' flames due to low temperature pre-reactions.

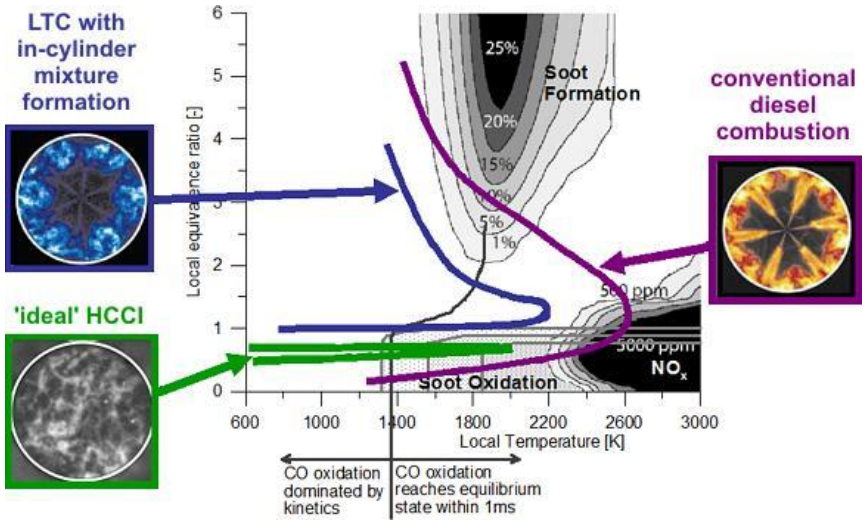

Figure 3.1 – Comparison of diesel combustion modes in local equivalence ration Φ and local flame temperature coordinates.

The research work of this thesis focused on "early injection" PCCI mode: the combined effect of shifting the injections to earlier times (the fuel is injected into

initially cooler and less dense gases, because injection occurs earlier in the compression stroke) and using heavy EGR rates (which reduces the oxygen concentration of the intake charge adding inert gases) lead to a slowed pre-ignition chemistry and higher ignition delay. This allows better pre-combustion mixing than conventional diesel combustion [54] avoiding the formation of rich mixture pockets within the cylinder, which is the main cause of soot generation [52]. Moreover, using heavy EGR rates leads to lower flame combustion temperatures and thus to lower NOx emissions [52, 61].

On the other hand, such a type of in-cylinder combustion process has to face different problems before being effective over the whole engine map of production applications. Due to heavily reduced oxygen content, low combustion temperatures and early injections, the formation of incomplete combustion products, such as CO and HC, can be significant, requiring higher conversion efficiency of the diesel oxidation catalyst [62]. In addition to this, due to sharp in-cylinder pressure rise, high noise level are generally related to the use of PCCI combustion [63], as well as penalties in fuel consumption [61].

In addition PCCI-like combustion modes are characterized by the fact that a significant amount of fuel is burned under premixed conditions. Hence the combustion rate and the ignition delay are governed by chemical kinetics of the mixture, so that controlling the combustion results quite complex, since fuel properties and in-cylinder conditions can strongly affect the process. In conventional diesel operations, even if the initial stage of the combustion is generally premixed, the majority of fuel burns under mixing-control conditions, in which the rate of mixing air and fuel governs the phenomenon, thus greatly simplifying the control of the heat release.

Many engine subsystems and control techniques have been studied in recent years to meet the requirements of emissions regulations. As far as diesel engines are concerned, real-time combustion control is one of the most widely researched application [64-72].

This technology can improve PCCI combustion performance, which is commonly affected by cycle-by-cycle and cylinder-by-cylinder variations, due to its pronounced sensitivity to changes in internal and external factors (ambient conditions, coolant temperature, EGR unbalance, engine component aging etc.). Besides, these combustion control techniques are of interest as they can dramatically reduce the time-consuming calibration of today's engine control

systems [66]. The conventional control architecture for modern ECU is map-based, requiring great experimental activity to be carried out in order to consider all possible engine operating conditions (e.g. taking into account transient corrections, multiple maps in function of the number of injections, etc.). With the adoption of innovative combustion control methods, exploiting the computational capabilities of modern ECUs, the main parameters related to engine performances could be determined in real-time on the basis of inputs directly measured on the engine itself [65-67].

In this context, being combustion phasing recognized to be one of the most important features affecting diesel combustion, MFB50 (i.e. crank angle at which 50% of the fuel mass fraction has burned) [64,65] and SOC (i.e., start of combustion) [69,70] represent the most frequently used parameters for such types of real-time controls. In some applications, other quantities, such as imep (indicated mean effective pressure) and maximum of HRR (heat release rate) [64] are considered, possibly in addition to abovementioned quantities.

Two different ways of controlling the MFB50 and the SOC in real-time are possible: pressure-based and model-based approaches. The former [64,65,67,69] needs a pressure transducer for the instantaneous measurement of in-cylinder pressure, from which the corresponding mass fraction burned X_b and the actual value of MFB50 are calculated. The latter is generally based on semi-empirical modeling of in-cylinder phenomena: one possibility is proposed in [70] based on the identification of the SOC by modeling and estimating the ignition delay, i.e. the length of the time interval between the SOI and the SOC in premixed diesel combustion. Another possible methodology is based on an improved accumulated fuel mass approach to estimate the heat release rate and the MFB50 by a low-throughput model which requires as inputs a set of engine quantities already measured or estimated by the standard ECU (such as engine speed, rail pressure, air mass, pressure and temperature in the intake manifold, fuel injected quantities and related injection timings) [71-73].

Another important benefit of combustion phasing control is related to the increased engine stability when new combustion concept such as Low Temperature Combustion (LTC) and Premixed Charge Compression Ignition (PCCI) are employed [65,68-70]. As already anticipated, within these operating conditions, in-cylinder processes become significantly different with respect to conventional diesel combustion mode. In particular, in case of operation with an engine designed for standard combustion and where the injection system is not specifically designed

for PCCI operation, it has been demonstrated that a huge variation may be obtained in terms of smoke and NO_x emissions thanks to the combustion temperature reduction.

In addition to the possible drawbacks for such a type of combustion mode above mentioned, high combustion instability can occur (especially related to the very high EGR rate used and uneven distribution among cylinders), thus making almost mandatory the use of combustion control to implement PCCI concept in real vehicles [65,70]. As a matter of fact, in these conditions the combustion is highly sensitive to variations of the intake conditions [68,70] and this may easily cause instability, i.e. wide cylinder-by-cylinder variations in terms of imep and MFB50 up to the occurrence of misfiring events. For speed and load transient operations, the different delay of the air path with respect to the fuel path determines that actual intake conditions may substantially deviate from steady-state calibrated values. This becomes especially critical for PCCI/HCCI combustion bringing to high pressure and imep fluctuations. Due to the slow dynamic behavior of the air path, closed-loop control on air path controllers/actuators cannot provide fast enough adaptation to the transient conditions. Therefore, combustion control may be effectively provided only through an accurate control of injection parameters in order to cope with requirements in terms of combustion and torque distribution stability, acoustic comfort and pollutant emissions.

In the third chapter of the thesis a preliminary study on the implementation of PCCI combustion on a traditional Diesel engine has been addressed, with particular attention on the statistical methodology exploited to efficiently plan experiments, build regression models and find optimal values of the control parameters to reach the best results.

Furthermore, different kinds of combustion controls have been applied under PCCI combustion operations, since in this condition the control of the combustion phasing results quite difficult to be implemented successfully, due the fact that a straightforward link between the start of injection and the start of combustion is no longer present as in traditional Diesel combustion mode.

Chapter 2

Performance analysis and fuel composition estimation in CNG engines fed with natural gas/biofuel/hydrogen blends

2.1 Preface

The present section contains a work reported in [36, 40], from which the contents has been partially retrieved. As already stated in the introduction, this first part of the present thesis deals with the usage of alternative fuels as a mean to address pollution and global warming problems. It is well known that the production of gaseous fuels from biomass results in a wide range of possible blends, with different chemical composition that cannot be estimated a priori. In a future scenario where different kind of fuel blends will be distributed at the pump station, it becomes really important to assess their impact on the engine in terms of performance and combustion behavior and to identify the composition of the gaseous mixture that is actually present in the vehicle tank.

Experimental tests on different working points, in terms of speed and load, were carried out on an internal combustion SI engine designed to run on CNG and fed with different gaseous mixtures. Firstly, an analysis of the engine performance was conducted in order to highlight that different mixtures fed to the engine strongly affect its combustion behavior, so that it becomes mandatory to recognize which kind of mixture is injected in the combustion chamber and consequently adjust the relevant ECU parameters. In fact, standard ECU hardware is not able to identify which fuel blend is present in the vehicle tank, it just relies on the lambda closed-loop control to set an injection duration in order to maintain a stoichiometric air/fuel ratio at the exhaust. Hence, as a second step, an algorithm capable of automatically estimate the composition of the gaseous blend actually fed to the engine has been

developed and assessed. The proposed method exploits commonly available ECU signals to identify, among a given set of mixtures, which blend, pertaining to a certain set, is the closest to the one actually fed to the engine in terms of chemical composition. The method has demonstrated to correctly estimate the real fuel mixture composition with a maximum error of 5% on the hydrogen volume content when HCNG mixtures are employed. The convergence is reached after less than 10 different engine working conditions, in terms of speed and load. A candidate set of 10 different sample blends has been initially considered and has been extended to a factorial set made up of more than 2 million blends, to further assess the capabilities of the proposed method.

2.2 Experimental set-up and tested blends

The engine that has been used for the present investigation is a turbocharged 1.4 liter passenger car engine, originally designed to run on CNG. The main specifications of the engine are listed in Table 2.1. The engine, coupled to a Borghi&Saveri eddy-current brake dynamometer, has been run on a test bench that was previously installed and instrumented [45,46].

The test bench is endowed with: a Hartmann and Braun ‘Sensyflow P’ hot-film air-mass sensor to measure the air flow rate to the engine; a Micro Motion ‘Elite’ Coriolis mass sensor [47], which is used to obtain an accurate measurement of the gaseous fuel mass flow rate; several thermocouples and piezoresistive transducers to measure the temperatures and the pressures, respectively, of the intake flow and the exhaust gases. Four Kistler ‘6052C’ piezoelectric transducers were installed on the head of the engine cylinders to acquire the pressure time-histories in each of the combustion chambers, thus allowing a thorough investigation to be made of the cylinder-to-cylinder variations. two NGK UEGO sensors, which evaluate the A/F ratio of the mixture (one dedicated to the rich mixtures, and the other to the lean mixture fields) in the exhaust pipe. The two UEGO sensors are the same, but different controllers are used to optimize the output in rich or lean conditions, namely the NGK TC-6100D for the rich mixtures and the NGK TC-6100C for the lean ones. The test facility includes an AVL ‘AMAi60’ pollutant analyzer, which is used to measure the THC, MHC, NOx, CO, CO2 and O2 gaseous emission levels in the exhaust gases.

The main engine operating quantities (such as brake torque, engine speed, air and fuel flow rates, exhaust emissions) were measured under thermal and mechanical steady-state working conditions. The pressure time-histories in the intake manifold (used for pegging in-cylinder pressures) and in the combustion

chambers were acquired, on a crank basis, every 0.1 °CA, over the whole engine cycle, for 100 consecutive cycles. The steady-state variables (e.g., pressures and temperatures in the intake and exhaust line pipes) were measured at a sample rate of 10 Hz and were averaged over a duration time of 1 min. All the measuring instruments were connected to a PC-based data acquisition system.

Table 2.1 – Tested engine characteristics

Engine Type	Fiat FIRE turbocharged T-Jet 1.4
Bore	72.0 mm
Stroke	84.0 mm
Compression ratio	9.8
Number of cylinders	4
Total displacement	1368 cm^3
Valves per cylinder	4
Combustion chamber	Pent-roof
Turbocharger	Wastegate controlled with a fixed geometry turbine
Injection	Port fuel
Fuel	Natural gas injected at 9 bar (relative pressure)
Injector type	Solenoid Injector Metatron E4 C601 110 R00014
Intake valve opening	377.7 °CA bTDC firing
Intake valve closing	125.7 °CA bTDC firing
Injection end	240-270 °CA bTDC firing

The engine was tested with reference blends of different composition, whose main average properties are reported in Table 2.2, in which α_{st}, LHV, R and γ are the stoichiometric A/F ratio, the lower heating value, the elastic coefficient and the isentropic index of the considered blend, respectively. These properties were calculated, for each blend of a given composition, considering the calculations reported in the Appendix of this section. The stoichiometric air/fuel ratio α_{st} depends on the stoichiometric combustion reaction. However, the combustion process is not directly involved in the recognition method, as highlighted in the following sections.

Table 2.2 – Composition (in volume percentage) and average properties of the tested reference fuel blends.

Species	**G20**	**HCNG15**	**HCNG25**	**HCNG30**	**G25**
Methane [vol. %]	≥ 97	≥ 83	≥ 72.5	≥ 67.5	≥ 82.5
Ethane [vol. %]	≤ 2	≤ 1.7	≤ 1.5	≤ 1.5	≤ 1.7
Propane [vol. %]	≤ 0.3	≤ 0.3	≤ 0.25	≤ 0.2	≤ 0.3
Butane [vol. %]	≤ 0.1	≤ 0.1	≤ 0.1	≤ 0.1	≤ 0.1
Carbon dioxide [vol. %]	≈ 0	≈ 0	≈ 0	≈ 0	≈ 0
Nitrogen [vol. %]	≤ 0.5	≈ 0.4	≈ 0.4	≈ 0.4	14 ± 0.5
Hydrogen [vol. %]	≤ 0.01	15 ± 0.5	25 ± 0.5	30 ± 0.5	≈ 0
Average properties					
α_{st} [–]	17.0	17.4	17.7	17.9	13.4
LHV [MJ/kg]	49.6	51.1	52.3	53.1	38.9
R [J/(kg·K)]	516	594	660	698	467
γ [–]	1.30	1.31	1.31	1.31	1.32
Gas density [kg/m^3] at 15 °C and 1 bar	0.673	0.585	0.526	0.497	0.741

According to the composition certificate of each tested blend, the volume content of each species is given as a maximum fraction when talking about impurities, such as ethane, propane and butane, while as a deviation from the nominal value when talking about main constituents, such as hydrogen in HCNG mixtures and nitrogen in G25. Hence, the actual fuel composition is known with an uncertainty. It is possible to verify how an increasing hydrogen content leads to higher values of α_{st}, R and LHV, while the presence of nitrogen in G25 strongly reduce their values. The gas composition has a minor effect on the isentropic index γ. In Table 2.2 the sulfur content is not reported, because according to the supplier's certificate, the presence of sulfur in the tested blends was extremely low (< 10 mg/m^3), which corresponds to ultra-low sulfur fuel. A very low concentration of sulfides is needed to avoid the formation of SO_x at the exhaust, which will lead to a poisoning of the after-treatment system. However, the presence of SO_x at the exhaust was not measured since standard exhaust emission analyzers for automotive applications where employed. Traces of corrosion due to the reaction of CO_2 and SO_x at the exhaust with water vapor were not found in the tested engine.

The experimental campaign was performed for the steady-state working points of the engine in the $1250 \leq n \leq 4600$ rpm and $0.5 \leq bmep \leq 14$ bar ranges. The test

Table 2.3 – Experimental test points (blue cells) in terms of load and speed.

Speed [rpm] / **Load [bar]**	1250	1500	1750	2000	2250	2500	2750	3000
0.5	■	■	■	■				
1	■	■	■	■				
2	■	■	■	■	■	■	■	
3	■	■	■	■	■	■	■	■
4	■	■	■	■	■	■	■	■
5	■	■	■	■	■	■	■	■

matrix was refined over a range of low engine speeds and loads (Table 2.3), which generally typifies the engine conditions right after vehicle refueling. In fact, whenever the vehicle is refuelled with biogas at a gas station, the fuel tank is refilled with a blend featuring an unknown composition. Once the engine is cranked, the ECU settings would anyhow be the ones corresponding to the original calibration, likely performed on CNG . Given that the control parameters should be promptly modified and that the engine is mostly likely to initially run at low loads and speeds, such conditions have been chosen as the main target for the investigation.

The considered blends were tested by adopting the original CNG ECU calibration, i.e. no adjustments to the parameters (such as SA and boost pressure) were considered when switching from one gaseous fuel to another. Given that biogas may retain a variable composition to a major extent, the performed experimental tests can be used to replicate a future scenario in which the engine is refueled at the gas station with a gaseous mixture holding an unknown composition. The ECU would just rely on the closed-loop lambda control to adjust the fuel injected quantity to match the stoichiometric A/F ratio.

2.3 Performance and combustion analysis

2.3.1 Results and discussion

The present section reports the results obtained for the engine running on the three among the fuel blends reported in Table 2.2, namely G20, G25 and HCNG30, at different loads and speeds for stoichiometric A/F ratios. The charts display the main performance- and combustion-related parameters.

The values of the different parameters have been obtained by properly averaging the data acquired within each cylinder over the test duration (Figs.2.1,2.2) as well as over the four cylinders throughout the experiment (“ensemble averaged-approach”) (Figs 2.3,2.4). As far as the combustion related parameters are concerned, the in-cylinder pressure has been analysed by means of a single-zone heat release model.

For each of the considered working points and for the engine running on G25 and HCNG30, the ECU parameters were kept to those pertaining to G20. Such a choice was meant to reproduce the actual ECU functioning after the vehicle refuelling: the ECU would not recognize the mixture composition and would hence stick to the previously implemented parameters. More specifically, the SA was set to the maximum brake torque (MBT) timing occurring for G20 operations. The tests

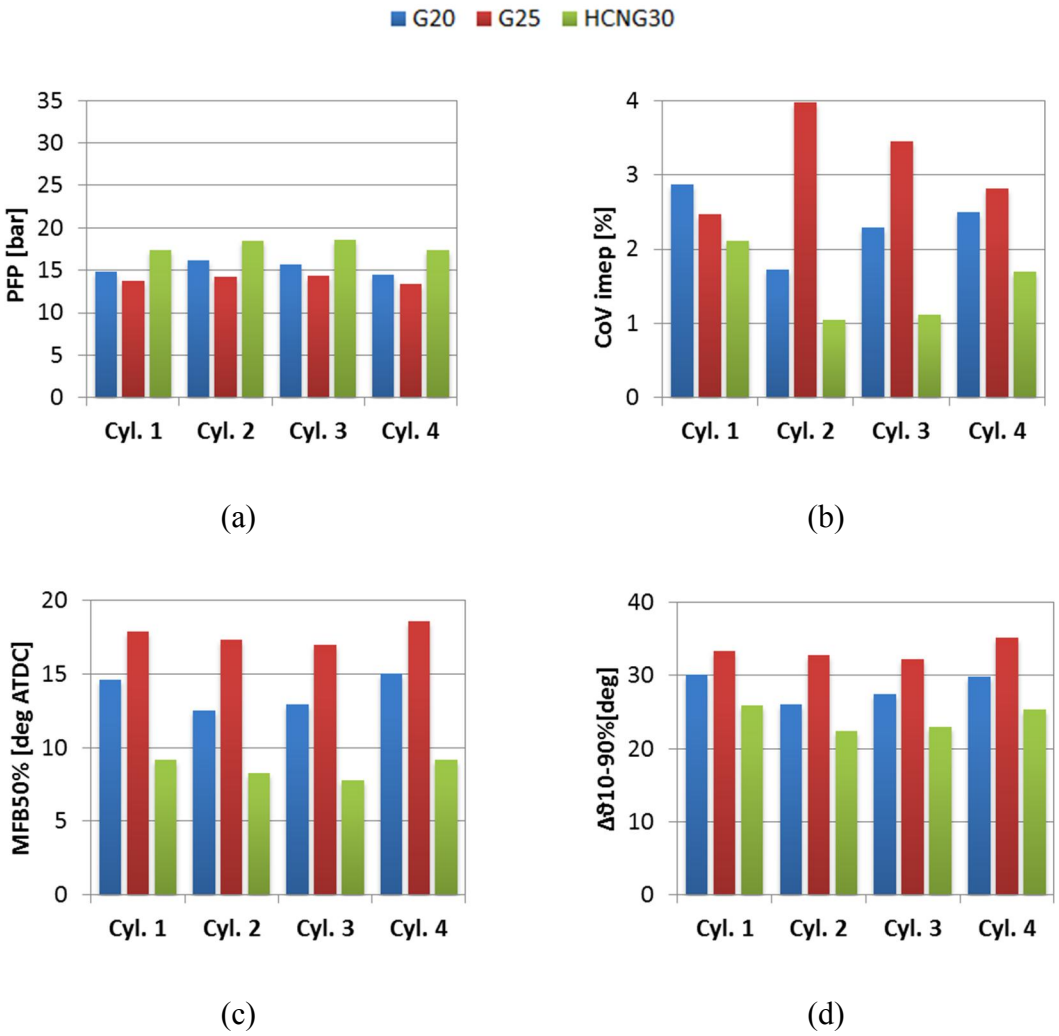

Figure 2.1 – Comparison amongst the cylinders for n=2000 rpm and bmep=2 bar.

were carried out by fixing the maximum coolant temperature at the engine inlet to 70°C. Such value has been chosen in order to reproduce the operating conditions that are mostly likely to occur when the engine is cranked after the vehicle refuelling. Moreover, given that the points in test matrix would not allow the cooling system for reaching the standard engine operating set-up (85°C) and given the need to comply with the constraint set by the impossibility to warm the coolant up, the diminished set point guarantees the different points to be acquired under equivalent engine conditions. The points will be shortly indicated considering the engine speed [rpm] and the bmep [bar] simply omitting the units.

The results in Figs. 2.1,2.2 focus on the comparison amongst the four cylinders output in terms of maximum in-cylinder pressure (peak firing pressure - PFP), CoV_{imep}, MFB50% and rapid burning interval ($\Delta\vartheta$10-90%) for different speeds and loads.

The charts report the results pertaining to two specific operating points, namely 2000x2 (Fig 2.1) and 3000x5 (Fig. 2.2). The different bars and colours address to

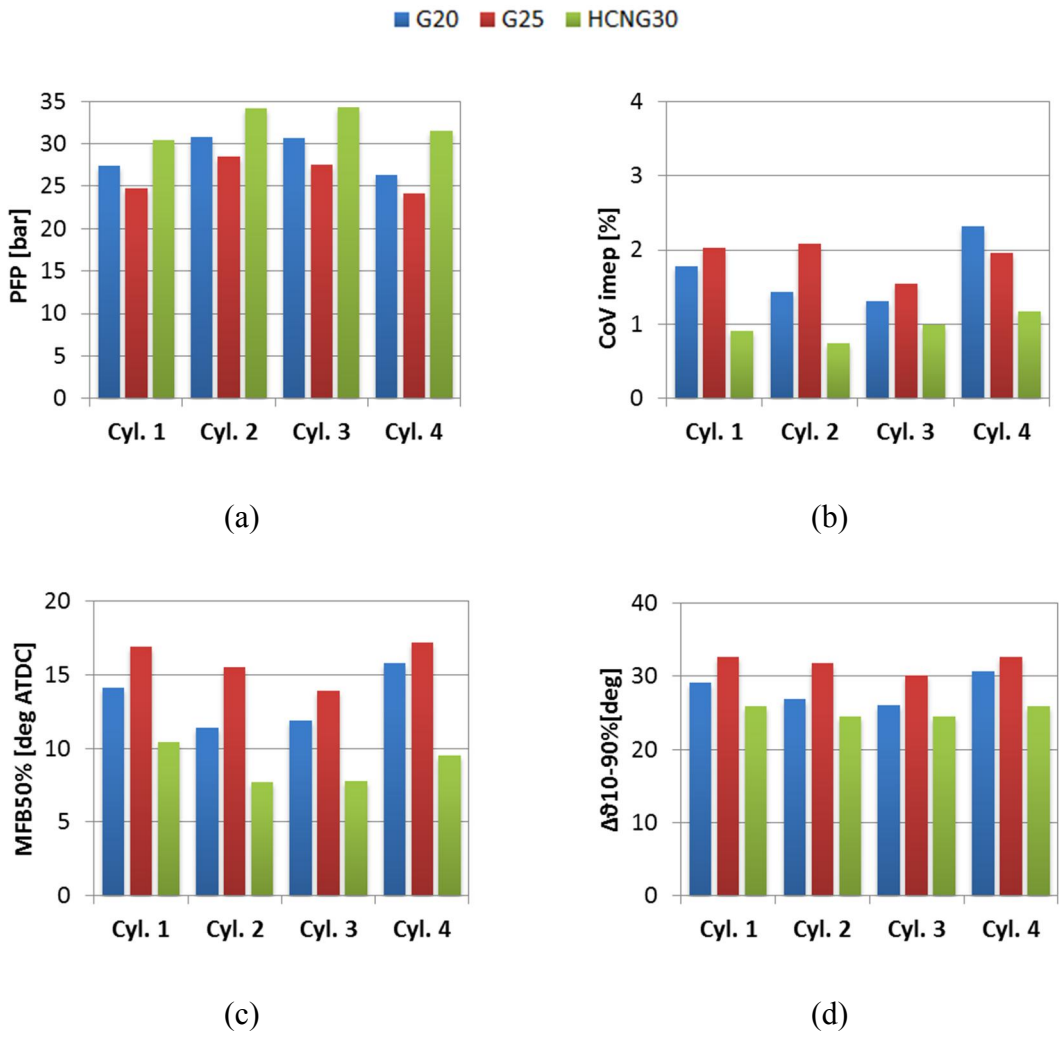

Figure 2.2 – Comparison amongst the cylinders for n=3000 rpm and bmep=5 bar.

the three considered fuel blends as depicted in the legend. Regardless of the specific operation point, such a choice results into a higher PFPs for the hydrogen enriched fuel (Figs. 2.1a, 2.2a). The increased flame laminar speed of hydrogen produces an early onset of the combustion process which will in turn overlap with the compression phase to a major extent, inducing higher in-cylinder pressures. The increased burning speed also reflects into reduced burning intervals (Figs. 2.1d, 2.2d) and hence into an increased operation stability (Figs. 2.1b, 2.2b).

The above mentioned results highlight the need to detect the proper ECU parameters according to the blend composition. Too high pressures would in fact result into excessive wear and consumption within the moving elements of the crank slider mechanism and could eventually bring to a failure. Such an issue has not to be taken into consideration in the speed and load range considered for the present investigation, but it might considerably affect the engine at different working points [44-46]. Increased temperatures would also lead to augmented thermal stresses, thus impairing the engine thermodynamic efficiency [47].

Opposite results are observed for the G25 fuelling due to the reduced laminar speed induced by the diluents in the mixture. Such a diminished speed in turn produces lower PFPs (Figs. 2.1a, 2.2a), retarded MFB50 values (Figs. 2.1c, 2.2c) and increased burning intervals (Figs. 2.1d, 2. 2d). Moreover, the scarce combustion repeatability seriously affects the cycle-to-cycle variability, thus mining the point stability as depicted by the peaking CoV values of Figs. 2.1b, 2.2b. Such behavior is further magnified by the even lower coolant temperatures (T_{H2O}°≈°68°C) which characterize engine points at low speeds and low loads, e.g. 2000x2 in Fig 2.1. Once more, the results hint at the need for proper ECU parameters so as to make up for the excessively decreased performance induced by the G25 composition.

The results in Figs. 2.3, 2.4 refer to the ensemble-averaged values over a speed sweep for a nominal bmep=3bar. Fig. 2.3a confirms the conclusion drawn from the previous charts. Taking the G20 performance as a reference baseline, hydrogen addition increases the in-cylinder pressures at any speeds. Still, the untimed combustion phasing, together with the increased burning speed, results into an advanced combustion which in turn leads to lower in-cylinder temperatures at the exhaust valve opening. The exhaust temperatures at the turbine inlet are hence diminished (Fig. 2.3b), thus assessing for a reduced flow enthalpy and a lower exploitation of the turbocharger group. Such a trend is verified at any load and speed and would seriously interfere with the turbocharger group functioning, especially

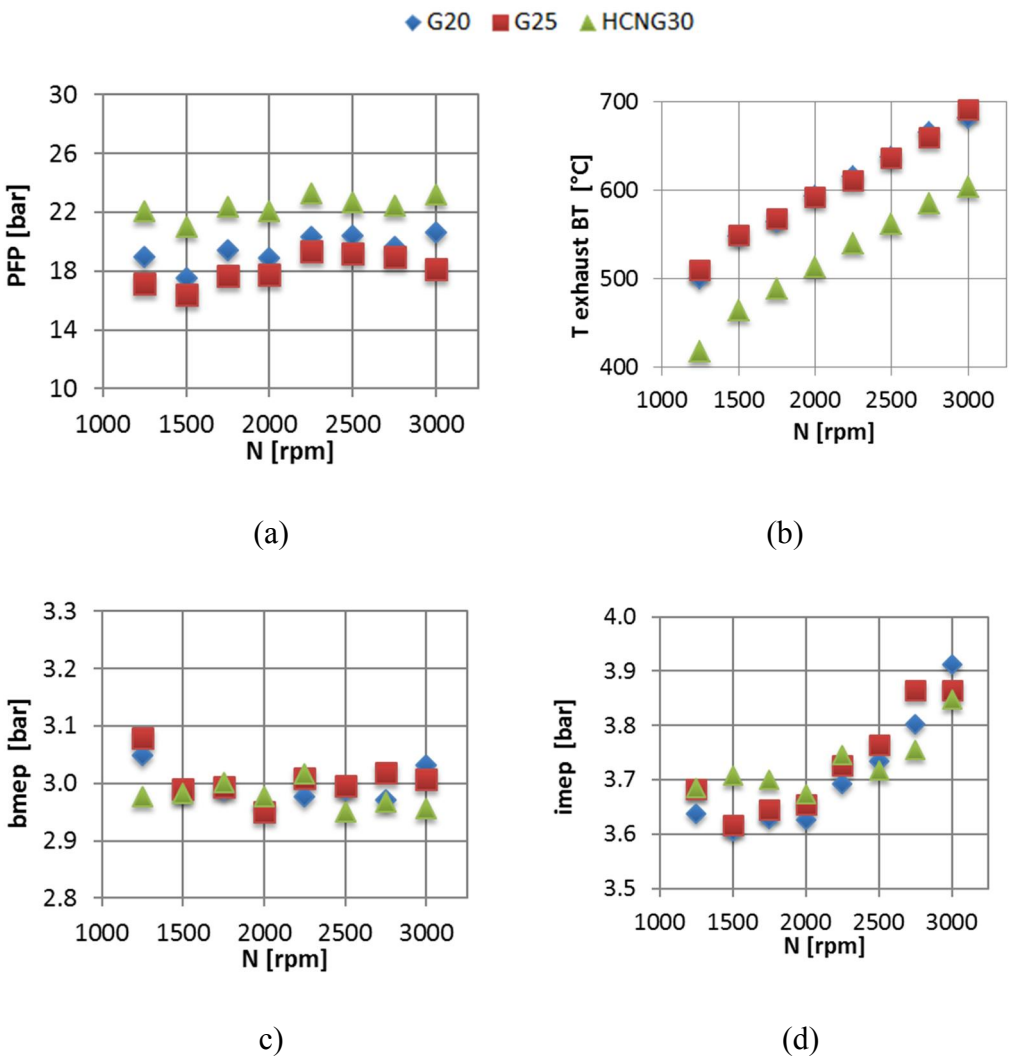

Figure 2.3 – Ensemble-averaged engine output over a speed sweep at nominal bmep=3bar.

at higher loads [48]. Contrariwise, the use of G25 induces lower in-cylinder pressures but scarcely affects the temperatures at the turbine inlet. Such behavior can be justified considering that the G20 timing produces a retarded G25 combustion which is responsible for the lower PFPs. Still, the combustion phasing and the increased rapid burning interval shift the combustion process towards the expansion phase and produce exhaust temperature equivalent to those pertaining to the G20 operations (Fig. 2.3b).

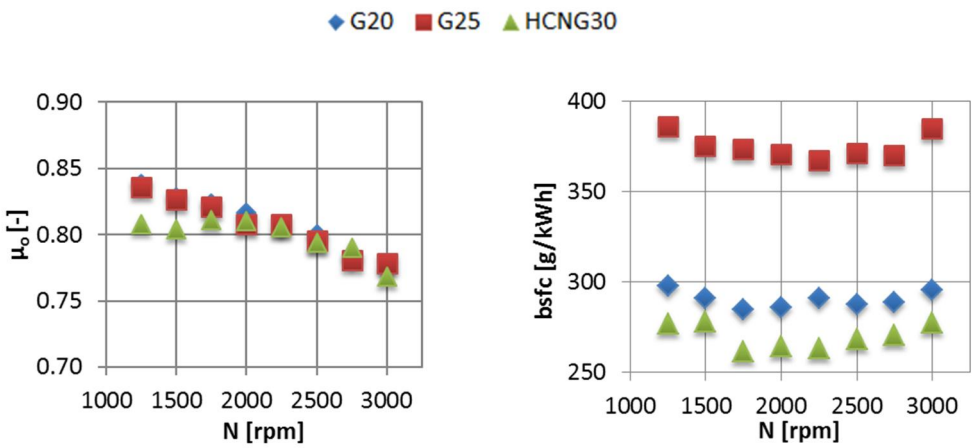

(a) (b)

Figure 2.4 – Engine mechanical efficiency and brake specific fuel consumption at bmep=3bar.

The charts in Figs 2.3c,d have been produced in order to assess for the preciseness of the engine points reproduced with the three blends in terms of bmep (Fig. 2.3c) as well as to allow for a thorough comparison of the engine efficiencies (see Fig. 2.4). The nominal bmep has been achieved within an average error ranging around 2% with a maximum value of 3% at 1250 rpm. This latter is due to the utilization of an eddy current brake not endowed with a closed loop control on the desired torque. Regardless of the nominal target, it is worth observing that the bmep values pertaining to the three blends are even closer one to another, thus giving consistency to the comparisons. Interesting conclusions can be inferred by combining the results from Fig. 2.3a to those in Figs. 2.3c,d for HCNG operations.

Low speed operations witness a higher influence of the in-cylinder pressure on the friction losses whereas the speed becomes a dominant factor as the engine speeds up. The increase in pressure produced by the hydrogen addition turns out to be higher in the low speed range, thus enhancing the previously mentioned effected and leading to the augmented imep values of Fig. 2.3d. Contrariwise, the HCNG imep values drop below the G20 ones in the high speed range as the raise in pressure is rendered ineffective by the increased influence of the speed on the losses. Such behavior is clearly depicted by the mechanical efficiency values of Fig. 2.4a. The small differences in the G25 imep values does not retain a true meaning but solely reflects the minor differences in the bmep of Fig. 2.3c. In fact, similar values for

the mechanical efficiency are found in Fig. 2.4a with the sound exception of the two extreme speeds. For n=1250 rpm the G25 bmep value reaches the highest threshold of the previously quoted interval (Fig. 2.3c) and, combining with the naturally lower pressures induced by the G25 operations, hence enhances the mechanical efficiency.

As expected, lower bsfc values (Fig. 2.4b) are attained for HCNG operations with respect to G20 fuelling whereas increased values stem for the G25 functioning due to the reduced energy content of the injected mass.

2.4. Fuel composition estimation

2.4.1 Model development

Considering conventional SI engines, the desired engine torque at fixed *n* speed is achieved acting on the throttle valve. The fuel injection system provides the corresponding stoichiometric fuel quantity, for most of the operating conditions, to comply with the optimization of the three-way catalyst. The closed-loop lambda control implemented in the ECU sends to each of the fuel injectors an electrical pulse, which has a duration that will be referred to as injection time t_{inj}. In the following, measurements units that have not been specified were evaluated in international system units.

It is possible to characterize an injector, for a given blend and keeping the pressure and temperature upstream of the injector constant, as well as the battery voltage V_{batt} used to provide the electrical pulse to the injector, by evaluating the injected mass, as a function of the injection time, through the following empirical regression equation [49]:

$$m_{inj} = \dot{m}_{inj,ss}\left(t_{inj} - offset\right) \tag{1}$$

in which:

m_{inj} is the injected fuel mass per cycle and per cylinder;

$\dot{m}_{inj,ss}$ is the steady-state flow rate when the injector is at the maximum opening position;

offset is a value that takes into account the time required to open and close the injector.

When the fuel composition, its conditions in the injection system, or the battery voltage are varied, Eq. (1) is still valid, but new $\dot{m}_{inj,ss}$ and *offset* values have to be recalculated accordingly to characterize the injected mass.

If a gaseous fuel is considered, the blend composition has a notable effect on the density of the fuel, as well as on its energy per unit mass, as expressed by LHV (see Table 2.2). In particular, it is expected that blends with a higher molecular mass will have a higher injected mass for a given injection time. It is worth observing that inert species (such as N_2 or CO_2), which may be present in the blend, contribute to the injected mass, but not to the energy available inside the cylinder.

As the fuel composition determines the corresponding injection time, a reverse procedure can be considered, in which the blend composition is identified from the injection time. However, an evaluation of the percentages of all the constituents of the blend is not straightforward. Therefore, the proposed procedure estimates the injection time for a number of sample blends, and then evaluates which of them are closer to the injection time measured by the ECU for the actual fuel in the vehicle tank, whose composition is not known in real applications.

Tests with several reference blends at different steady-state engine conditions (in terms of torque and engine speed) were conducted in the experimental campaign, as illustrated in Section 2.2. An almost linear dependence of the injected mass on the injection time, as described by Eq. 1, can be observed in Fig.2.5. It is also possible to note that the blend composition affects the slope of each line. In particular, two different blends of fuel G20 (virtually corresponding to the same composition) were considered. These tests were performed with different battery voltage levels, in order to take into account the corresponding influence on the injected mass.

The injected mass m_{inj} of fuel per cycle and per cylinder (Fig. 2.5) can be calculated from the engine speed n and the fuel mass flow $\dot{m}_f$. In the considered application, this latter is measured by the Coriolis mass flowmeter installed upstream of the fuel injection system of the engine (see Section 2.2), according to the following equation:

$$m_{inj}\left[mg\right] = \frac{\dot{m}_f\left[kg/h\right]}{3600 \cdot N_{cyl} \cdot \frac{n\left[rpm\right]}{2 \cdot 60}} \cdot 10^6 \qquad (2)$$

N_{cyl} is the number of cylinders of the engine, each of which is fed with virtually the same amount of fuel. The injected mass is proportional to the density of the blend. Therefore, according to the perfect gas law, the lower the value of R in Table 2.2, the higher the fuel density and the higher the injected mass at the fixed injection time shown in Fig 2.5.

In order to have a fast procedure, which could be possibly implemented in an ECU for real-time calculations, the injector can be characterized as a nozzle working under a steady-state adiabatic condition. The gaseous fuel flow in the fuel system considered in the present application can always be considered as chocked, due to the values of the absolute pressure upstream (around 10 bar in the considered injection system downstream of the fuel pressure regulator) and downstream of the injector (generally in the 0.5-2.5 bar range in the intake manifold).

Therefore, the flow rate from the nozzle, reported in Eq. 1, can be written as follows [47,50]:

$$\dot{m}_{inj,ss} = A_{eff,ss} \frac{p_{rail}}{\sqrt{R \cdot T_{rail}}} \sqrt{\gamma \left(\frac{2}{\gamma+1} \right)^{\frac{\gamma+1}{\gamma-1}}} = A_{eff,ss} \cdot \frac{p_{rail}}{\sqrt{T_{rail}}} \cdot K = A_{eff,ss} \cdot G \tag{3a}$$

$A_{eff,ss}$ is the effective restricted flow-area of the chocked nozzle when a steady-state flow (in which the injector is at the completely open position) is considered and p_{rail}, T_{rail} are the pressure and the temperature, respectively, in the rail of the injection system. In Eq. 3, K is a parameter that depends only on the fuel composition, while parameter G also depends on the working conditions.

The actual injection phase is dynamic. It has an opening and a closing phase, and the restricted flow-area, which is initially zero, increases to a maximum value and then goes back to zero at the end of the injection. Therefore, Eq. 3a can be rewritten considering the dynamic injection phase:

$$\dot{m}_{inj} = A_{eff} \frac{p_{rail}}{\sqrt{R \cdot T_{rail}}} \sqrt{\gamma \left(\frac{2}{\gamma+1} \right)^{\frac{\gamma+1}{\gamma-1}}} = A_{eff} \cdot \frac{p_{rail}}{\sqrt{T_{rail}}} \cdot K = A_{eff} \cdot G \tag{3b}$$

in which A_{eff} is the mean effective restricted flow-area during the injection phase, which encompasses the instantaneous transient phenomena. The longer the injection time, the longer the duration of the period at which the nozzle is in the completely open position, and, therefore, the lower the percentage influence of the

opening and closing phases: as a consequence, A_{eff} is expected to increase with the injection time t_{inj} and to reach the $A_{eff,ss}$ value.

It is possible to correlate the injected mass m_{inj} per cycle and per cylinder to the flow rate $\dot{m}_f$, measured by the fuel flowmeter, and to the average flow rate $\dot{m}_{inj}$ during the injection phase:

$$m_{inj} = \frac{\dot{m}_f}{N_{cyl}} t_{cycle} = \dot{m}_{inj} t_{inj} \tag{4}$$

in which t_{cycle} is the time required to complete an engine cycle. As the injector is only open for a part of the whole cycle, it results that $t_{inj} < t_{cycle}$ and $\dot{m}_{inj} > \dot{m}_f / N_{cyl}$.

Combining Eqs. 3b and 4, it is possible to write:

$$\frac{m_{inj}}{G} = A_{eff} \cdot t_{inj} \tag{5}$$

Each of the terms on the left hand side of the equation is related to the blend composition and to the working conditions whereas the right hand side of the equation only depends on the ECU injection time and is hence unaffected both by the blend composition and by the working conditions. The data in Fig. 2.5a are replotted in Fig. 2.5b, considering Eq. 5. As expected, the dispersion among the blends is much lower in Fig. 2.5b, given that almost all the experimental points lie on the same straight line. The residual dispersion can be attributed not only to the experimental uncertainty but also to possible uncertainties in the composition of the blend as well as to differences in the battery voltage during the actuation of the injector.

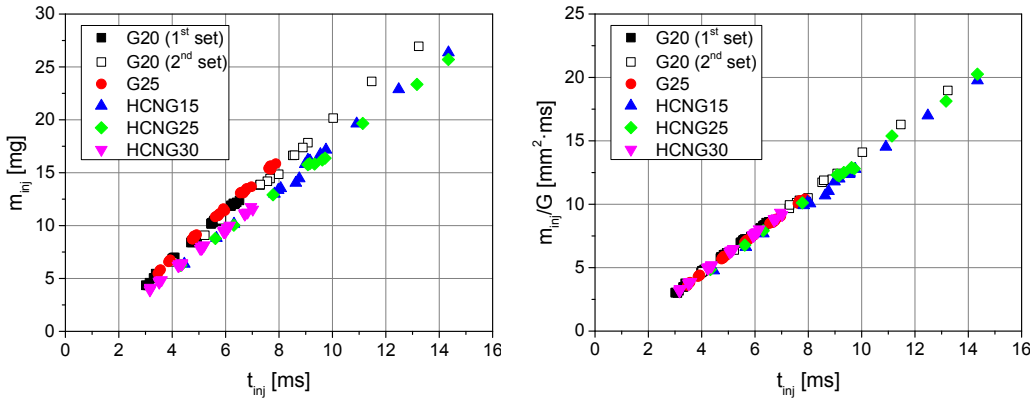

(a) (b)

Figure 2.5 - Injected mass of fuel, per cycle and per cylinder (a) and injected mass of fuel, per cycle and per cylinder divided by the term G (b), as a function of the injection time for the different reference blends

A random subset, referred to as *model data*, corresponding to about 40% of the data reported in Fig. 2.5, has been used to characterize the injector. A linear regression of the m_{inj}/G parameter was evaluated as a fitting function of the injection time and battery voltage:

$$\left(\frac{m_{inj}}{G}\right)_{fit} = A + B \cdot t_{inj} + C \cdot V_{batt} \tag{6}$$

The coefficient of determination, R^2, of the above linear regression was higher than 0.99 and could therefore be considered to be a very good approximation of the *model data*. The remaining data, which were not used for the model construction, were instead used for the model validation (see Section 2.4.4) and are therefore referred to as *validation data*. Outliers were excluded when the regression model was fitted, according to the 'externally studentized' residuals analysis. Such statistical technique is based on the evaluation of the residual of each point divided by an estimate of the standard deviation computed without considering that specific point ('external studentization'). Test point with a value above a given threshold (3 in the present case) were considered to be eligible as outliers and excluded if they were actually caused by experimental errors. According to Eq. 1, coefficient A is negative, since t_{inj} has to be much higher than 0 to provide even a small amount of injected fuel. It is worth noting that, should the effect of a change in V_{batt} be neglected, the variation in t_{inj} would be wrongly attributed to a variation of the blend

composition rather than to a different dynamic response of the injector. For instance, it was found that a voltage variation of 5% leads to a t_{inj} variation of about 1.7%, which can also be obtained for a hydrogen content variation of 4% in a binary CH_4-H_2 blend.

Considering a mean reference voltage (calculated as an average of all the experimental data reported in Fig. 2.5), Eq. 6 is simplified and an equation that corresponds to Eq. 1 is practically obtained. Combing it with Eq. 5, the following corrected relationship holds:

$$\left(\frac{m_{inj}}{G}\right)_{cor} = D + B \cdot t_{inj} = A_{eff} \cdot t_{inj} \tag{7}$$

Therefore, the mean effective area A_{eff} results to be inversely dependent on the injection time, as reported in Fig. 3:

$$A_{eff} = \frac{D + B \cdot t_{inj}}{t_{inj}} = B + \frac{D}{t_{inj}} \tag{8}$$

As expected, A_{eff} asymptotically increases with injection time t_{inj}. In fact, the relative influence of the opening and closing times decrease when t_{inj} increases. Fig. 2.6 plots the values of A_{eff} pertaining to the *model data* obtained from Eq. 5 for each experimental test and those derived by the regression curve from Eq.8. Systematic deviations from the regression curve (e.g. HCNG15 in Fig. 2.6) are due to battery voltage differences with respect to the mean reference value.

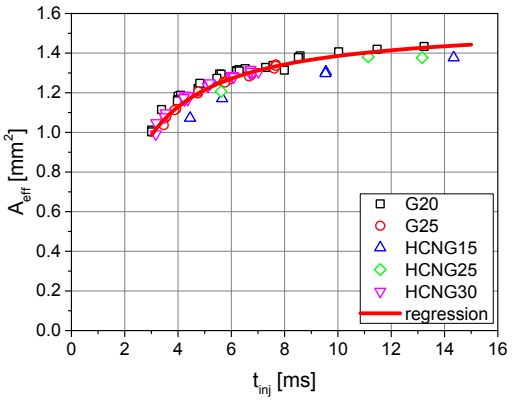

Figure 2.6. Mean effective area A_{eff} as a function of the injection time t_{inj} evaluated considering the *model data* and the regression obtained from Eq. 8.

2.4.2 Model implementation

The ECU sets the injection time, $t_{injECU,}$ necessary to inject the correct amount of the unknown blend in order to have a stoichiometric air/fuel ratio in the engine under closed-loop control for each working point of the engine.

A set of different sample gaseous blends of known composition, reported in Table 2.4, can be chosen as representative of the possible wide variety of blends that can be fed to the engine, and this set is used as input to the regression model. The fuel properties (i.e., α_{st}, R and γ) of each sample blend, are evaluated through the calculations reported in the **Appendix**. Therefore, it is possible to calculate the injection time, $t_{inj,}$ that would correspond to the actual injected mass of fuel, m_{inj}. By comparing the calculated t_{inj} for each blend with the t_{injECU} set by the ECU, it is possible to check whether that blend is 'compatible' with the unknown one actually fed to the fuel system.

The value of t_{inj} can be calculated according to Eq. 4 as:

$$t_{inj} = \frac{m_{inj}}{\dot{m}_{inj}}$$

in which the numerator is evaluated on the basis of experimental values, according to Eq. 2, and the denominator is evaluated according to Eq. 3b. However, this procedure is iterative, as A_{eff} in Eq. 3b depends on the injection time that has to be evaluated (Fig 2.6):

$$t_{inj} = \frac{m_{inj}}{G \cdot A_{eff}\left(t_{inj}\right)} \tag{9}$$

The iterative procedure can be avoided if t_{inj} is computed considering the injector model represented by Eq. 6:

$$t_{inj} = \frac{1}{B}\left(\frac{m_{inj}}{G} - A - C \cdot V_{batt}\right) \tag{10a}$$

in which m_{inj} is calculated from the test cell fuel flowmeter using Eq. 2. Alternatively, m_{inj} can be computed starting from the mass air flow, using either the test cell or the engine flowmeter (MAF), and dividing it by the stoichiometric A/F ratio (as the engine is considered to operate under closed loop feedback control). Therefore, it is possible to write:

$$m_{inj} = \frac{m_{air}}{\alpha_{st}} \tag{11}$$

where m_{air} is the air mass per cycle and per cylinder, evaluated from the air flow rate fed to the engine, using a similar equation to Eq. 2.

Eq 10a can be rewritten as:

$$t_{inj} = \frac{1}{B}\left(\frac{m_{air}/\alpha_{st}}{G} - A - C \cdot V_{batt}\right) \tag{10b}$$

Finally, it is possible to evaluate the absolute error (*AE*) and relative error (*RE*) between the calculated t_{inj} and the measured t_{injECU} as:

$$AEt_{inj} = t_{inj} - t_{injECU} \tag{12a}$$

$$REt_{inj} = \frac{t_{inj} - t_{injECU}}{t_{injECU}} \tag{12b}$$

If the error is close to zero, the sample blend may have a similar composition to the actual (unknown) one that is injected into the engine. As the uncertainty relative to just one operating condition may provide a bad match of the sample blends, it is advisable to perform the calculation on several test points. Therefore, when *N* different experimental working points are taken into account, a root mean square error (*RMSE*) and a mean relative error (*MRE*) of t_{inj} can be defined, respectively, as:

$$RMSEt_{inj} = \sqrt[2]{\frac{\sum_{N}\left(t_{inj} - t_{injECU}\right)^2}{N}} \tag{13a}$$

$$MREt_{inj} = \frac{1}{N}\sum_{N}\frac{t_{inj} - t_{injECU}}{t_{injECU}} \tag{13b}$$

Fig. 2.6 reports a simplified flow-chart relative to the blend identification through the air measurement performed by means of the vehicle MAF. The engine tank is filled with a blend of unknown composition (red rectangle). For a given set of sample blends (blue rectangle) the corresponding composition is retrieved via look-up tables and the needed properties (γ , R , α_{st} in this case) are calculated and sent as input to the regression model of the injector. The regression model also receives the measurement of the air mass from the engine MAF (m_{air}), battery

voltage, p_{rail} and T_{rail} (which is not reported in the flowchart for the sack of brevity). For each sample blend an estimated injection time (t_{inj}) is then computed and sent as output. The estimated injection times for all the blends are then compared to the actual injection time from the ECU (t_{injECU}). Finally, the blend which minimizes the error between the actual and the estimated injection time – min(t_{inj}-t_{injECU}) – is identified as the closest one to the unknown blend present in the engine tank. It is worthwhile to mention that when the fuel-flow meter measurement is used instead of the engine MAF one, the regression model will receive as input the relevant properties (just γ, R in this case) and the injected fuel mass (m_{inj}).

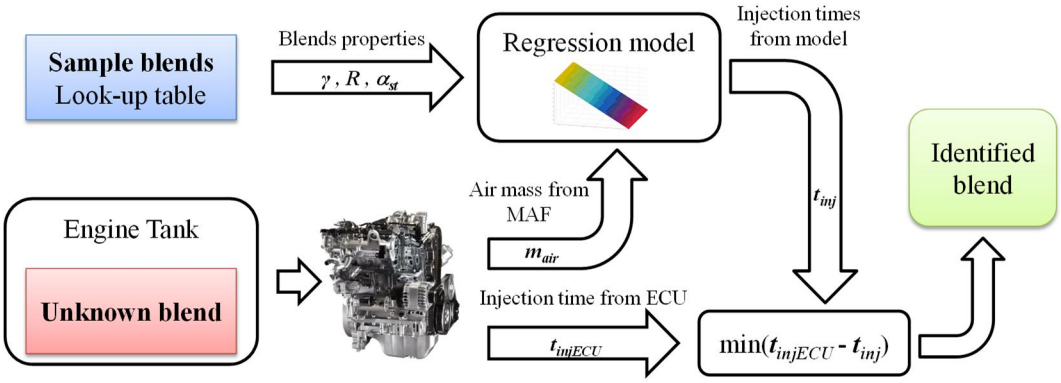

Figure 2.6 - Simplified flow-chart of the blend identification procedure.

2.4.3 Further considerations on the model

The model considers that a certain amount of fuel, $m_{inj,}$ is injected during the known injection time t_{injECU}. When the engine is working in the test cell, the amount of injected mass is experimentally measured by the fuel flowmeter, and m_{inj} can be calculated, even if the blend composition is unknown. Moreover, m_{inj} can be expressed as:

$$m_{inj} = \left(\frac{m_{inj}}{G} \right) G \tag{14}$$

and the ratio in parenthesis can be replaced by the regression model expressed by Eq. 6.

Hence, when a fuel blend is compared with another, assumed as a reference, and here indicated with an asterisk *, it is possible to write the following formula, considering m_{inj} as an assigned quantity in the procedure:

$$\left(A+B\cdot t_{inj}+C\cdot V_{batt}\right)\cdot\frac{p_{rail}}{\sqrt{T_{rail}}}K=\left(A+B\cdot t_{inj}^{*}+C\cdot V_{batt}^{*}\right)\cdot\frac{p_{rail}^{*}}{\sqrt{T_{rail}^{*}}}K^{*} \tag{15a}$$

By taking into account that the rail pressure and temperature are also known (and are independent of the considered blend):

$$\frac{t_{inj}+\dfrac{A+C\cdot V_{batt}}{B}}{t_{inj}^{*}+\dfrac{A+C\cdot V_{batt}^{*}}{B}}=\frac{K^{*}}{K} \tag{16a}$$

Therefore, an expected variation of injection time t_{inj} can be predicted when switching from one blend to another at fixed injected mass m_{inj}.

However, only the air flow rate is generally measured on the vehicle through a conventional engine MAF. Therefore, the comparison between different blends would need be done considering the quantity of injected fuel, m_{inj}, as no longer being assigned, but rather the air quantity m_{air} as being assigned. Considering Eqs. 11 and 14, Eqs. 15a and 16a would become, respectively:

$$\left(A+B\cdot t_{inj}+C\cdot V_{batt}\right)\cdot\frac{p_{rail}}{\sqrt{T_{rail}}}K\cdot\alpha_{st}=\left(A+B\cdot t_{inj}^{*}+C\cdot V_{batt}^{*}\right)\cdot\frac{p_{rail}^{*}}{\sqrt{T_{rail}^{*}}}K^{*}\cdot\alpha_{st}^{*} \tag{15b}$$

$$\frac{t_{inj}+\dfrac{A+C\cdot V_{batt}}{B}}{t_{inj}^{*}+\dfrac{A+C\cdot V_{batt}}{B}}=\frac{K^{*}\cdot\alpha_{st}^{*}}{K\cdot\alpha_{st}} \tag{16b}$$

From Eqs. 16a and 16b, it is theoretically possible to estimate the variation of the injection time when switching from one blend to another, when the measurements of the fuel flow and air flow are considered, respectively. It is worth noting that the considered procedure cannot distinguish between different blends for which the second members of Eqs. 16a and 16b are the same. More specifically, if the measurement of the fuel flow rate is considered, two blends cannot be distinguished if they have the same K value. Contrariwise, if the measurement of the air flow rate is considered, two blends cannot be distinguished if they have the same $K\cdot\alpha_{st}$ product. With reference to Table 2.5, a ratio higher than 1 for each of the two measurements, i.e. of the fuel or air flow rate, suggests that the injection

time will increase for the considered sample blend, with respect to the reference one. A ratio lower than 1 hints at a decrease in the injection time.

Ten different sample blends, whose composition is reported in Table 2.4, were considered initially.

It should be pointed out that the same of the tested blends (see Table 2.4) actually correspond by name to the reference blends reported in Table 2.2. As a matter of fact, they virtually feature the same compositions and might simply differ

Table 2.4 - Considered composition, in volume percentage, of the ten different sample blends.

	CH4	**GPL**	**G25**	**G25.1**	**HCNG5**	**HCNG10**	**HCNG15**	**HCNG20**	**HCNG25**	**HCNG30**
Methane [vol. %]	100	0	86	86	95	90	85	80	75	70
Ethane [vol. %]	0	0	0	0	0	0	0	0	0	0
Propane [vol. %]	0	50	0	0	0	0	0	0	0	0
Butane [vol. %]	0	50	0	0	0	0	0	0	0	0
Carbon dioxide [vol. %]	0	0	0	14	0	0	0	0	0	0
Nitrogen [vol. %]	0	0	14	0	0	0	0	0	0	0
Hydrogen [vol. %]	0	0	0	0	5	10	15	20	25	30

Table 2.5 - Comparison of different blends with respect to CH_4. K is expressed in International System units.

		CH_4	**GPL**	**G25**	**G25.1**	**HCNG5**	**HCNG10**	**HCNG15**	**HCNG20**	**HCNG25**	**HCNG30**
m_{inj} assigned	K	0.029	0.049	0.031	0.033	0.029	0.028	0.027	0.027	0.026	0.025
m_{inj} assigned	$\frac{K^*}{K}$	1	0.59	0.95	0.90	1.02	1.05	1.07	1.10	1.13	1.16
m_{air} assigned	$K \cdot \alpha_{st}$	0.504	0.765	0.415	0.388	0.496	0.488	0.480	0.472	0.464	0.455
m_{air} assigned	$\frac{K^* \cdot \alpha_{st}^*}{K \cdot \alpha_{st}}$	1	0.66	1.22	1.30	1.02	1.03	1.05	1.07	1.09	1.11

because of the accuracy of the mixture preparation process. When CH_4 is considered as a reference blend (indicated with an asterisk), the values in Table 2.5 are obtained with respect to the sample blends reported in Table 2.4.

In a similar way to what was done for the injection time, it is possible to calculate estimated values of the stoichiometric A/F ratio, from the measurement of either the fuel or the air flow rate, that correspond to:

$$\alpha_{calc} = \frac{\alpha_{st} \cdot m_{inj}}{\left(A + B \cdot t_{injECU} + C \cdot V_{batt}\right) \cdot G} \tag{17a}$$

$$\alpha_{calc} = \frac{m_{air}}{\left(A + B \cdot t_{injECU} + C \cdot V_{batt}\right) \cdot G} \tag{17b}$$

An error relative to α_{st} could then be evaluated in a similar way as to when Eqs. 12a,b are used, and the same results are reached.

2.4.4 Results and discussion

2.4.4.1 Model validation: set of sample blends

The method proposed in was then applied to the *validation data* in order to find the best match between each tested blend (reported in Table 2.2) and one of the sample blends (reported in Table 2.4). In fact, the procedure assumes that any real biogas fuel (possibly fed to the injection system of the engine) has to be represented by one sample blend of an appropriately selected set. It is worth stressing that, according to the present methodology, the characteristics of the real blends, which are not known by the engine ECU on real applications after refueling, are not used in the calculation to find the match.

A relative error, REt_{inj}, was calculated, between each sample and each real blend, for each experimental working condition (expressed in terms of engine speed and load) of the *validation data,* according Eq. 12b. The average error, $MREt_{inj,}$ of all the working conditions was then calculated according to Eq. 13b, and the results are reported in Fig. 2.7.

The lower the height of the bars in Fig. 2.7, the closer the sample blend is to the fuel blend considered in each graph. The different fuels and air measurements used for the calculations are reported in different colors.

In order to summarize the results depicted in Fig. 2.7, the associated sample blend that exhibits the lowest $MREt_{inj}$ for each real blend is reported in Table 2.6.

As can be seen, two incorrect matches can be found. These results are related to the measurement of the engine MAF, the accuracy of which is lower than that of the test cell instrumentation. It should be pointed out that, in such cases, the composition of the estimated sample mixture still results to be similar to the real one, with a maximum uncertainty of 5% in H_2 content when HCNG blends are considered. Anyway, the properties of the two mixtures are fairly similar, in terms of combustion velocity, knock resistance and energy content.

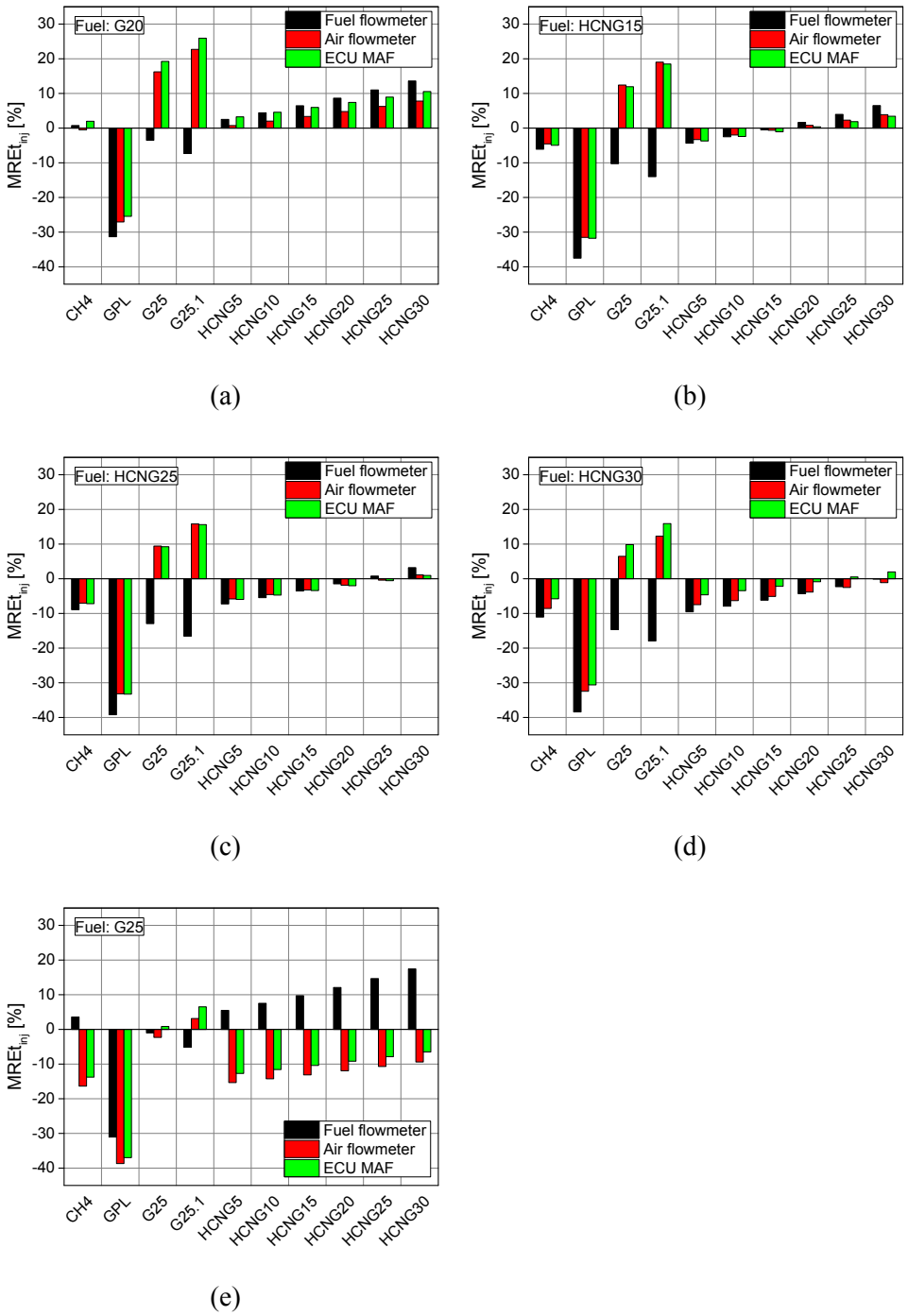

Figure 2.7 - Comparison of the different sample blends and the G20 (a), HCNG15 (b), HCNG25 (c), HCNG30 (d) and G25 (e) real blends.

Table 2.6 - Sample blends identified by means of the methodology for each real blend, according to the considered fuel or air flow measurement.

	G20	**G25**	**HCNG15**	**HCNG25**	**HCNG30**
Fuel flowmeter	CH4	G25	HCNG15	HCNG25	HCNG30
Air flowmeter	CH4	G25	HCNG15	HCNG25	HCNG30
Engine MAF	CH4	G25	HCNG20	HCNG25	HCNG25

Fig. 2.8 plots the relative error, $RE_{inj,}$ of each *validation data* test, ordered randomly, in solid symbols. The empty symbols with the line instead refer to the cumulative mean value of t_{inj} (*partial* MRE_{inj}), evaluated considering an increasing number of test points. As soon as the number of points starts to increase, the *partial* MRE_{inj} tends to rapidly converge to the mean value (red horizontal line) obtained considering all the experimental *validation data* tests. Deviation of each single test from the average value are due to errors introduced by uncertainties in the nominal composition of the tested blends, experimental uncertainties and regression fitting. Regardless of the blend composition, of the engine working conditions and of the methodology used for fuel or air measurement, convergence is generally reached with less than 10 test points.

Even though the composition of the real biogas fuel in the tank can vary over a wide range, the number of calibrations that have to be implemented in an ECU is limited, and each calibration should correspond to a mixture (or rather to a family of mixtures), whose behavior in the engine differs substantially from the others. Therefore, this consideration suggests that it may not be advisable to have a set with a large number of different sample blends for on-board applications.

The recognition algorithm proposed in this section has been evaluated off-line, to demonstrate if it features all the needed qualities to be implemented on-board in a following step. It is possible to state that the model is very accurate when measurements from test cell instrumentation are used for the calculation. Moreover, the model still proves to be reliable for higher uncertainties, such as those produced by the engine conventional automotive instrumentation, thus highlighting the

potential for on-board application. Furthermore, the fast convergence of the methodology provides an advantage for real-time application after tank refueling.

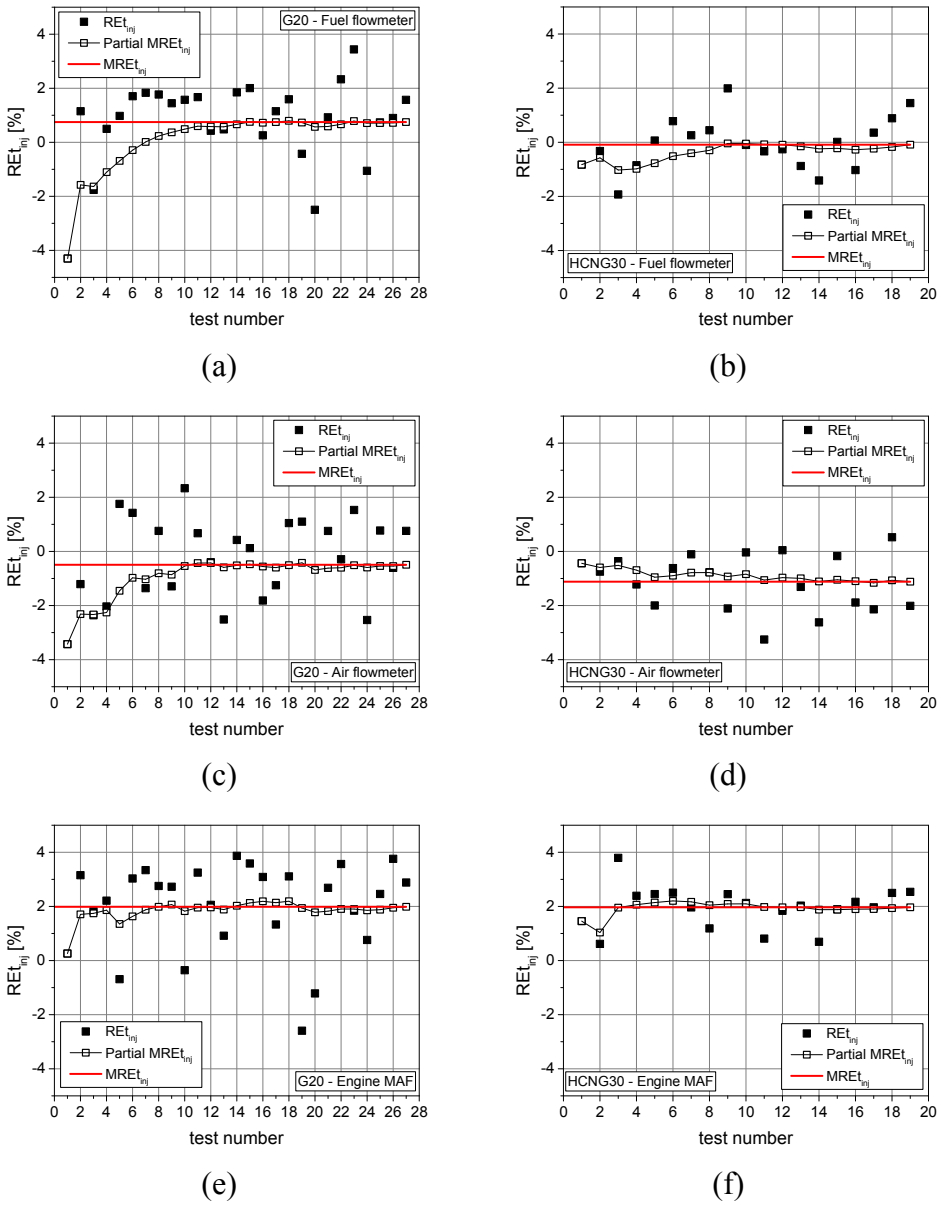

Figure 2.8 - Relative errors, $RE_{inj,}$ the corresponding cumulative *partial* MRE_{inj} and the final mean value MRE_{inj} related to the G20 and HCNG30 reference fuels.

2.4.4.2 Model validation: set of full factorial mixtures

This section presents the results obtained from a further model employment step, in which the calculation was extended to a set of full factorial mixtures, instead of a limited set of sample blends. Different volume percentage levels were considered for each species, according to the limits reported in Table 2.7. The percentage of methane is not reported in the table because it was evaluated as the complement, to 100, of the sum of the other species. Considering the values reported in Table 6, the full factorial set is made up of 2'335'230 different mixtures.

Table 2.7 - Minimum, maximum and step volume percentages considered for the full factorial mixtures.

	min	max	Step
Ethane	0	2	0.5
Propane	0	1	0.5
Butane	0	0.5	0.5
Carbon dioxide	0	15	0.5
Nitrogen	0	15	0.5
Hydrogen	0	40	0.5

The *validation data* were considered for each kind of measurement (i.e., test cell fuel, air flowmeter, engine MAF) following the same recognition method proposed for the set of sample blends. Results corresponding to the 10 'best mixtures' (i.e., corresponding to the 10 mixtures that showed the lowest $MREt_{inj}$ values within the factorial set) are reported in the radar plots in Figs 2.9, 2.10 and 2.11 for the G20, HCNG30 and G25 real fuels, respectively.

Each of the 10 'best mixtures' is represented by a seven-sided polygon, with the red perimeter and round symbols on the vertices representing the concentration in volume of the related species. A similar composition implies an almost overlap of the corresponding polygons. According to Figs. 2.8, 2.9 and 2.10, G20 is correctly detected by solely exploiting the air flow rate measurement (either from the test cell or the engine MAF in Figs. 2.9b and c). HCNG30 is accurately identified taking advantage of the fuel flow rate measurement in Fig. 2.10a. Finally, G25 is not univocally detected by any of the measurement devices, due to the high dispersion in the composition of the 10 'best mixture' in Figs 2.11a, b, c. This behavior is related to the fact that, as previously mentioned, the fuel flow rate and air flow rate measurements are not able to distinguish between mixtures with the same K and $K \cdot \alpha_{st}$ values, respectively.

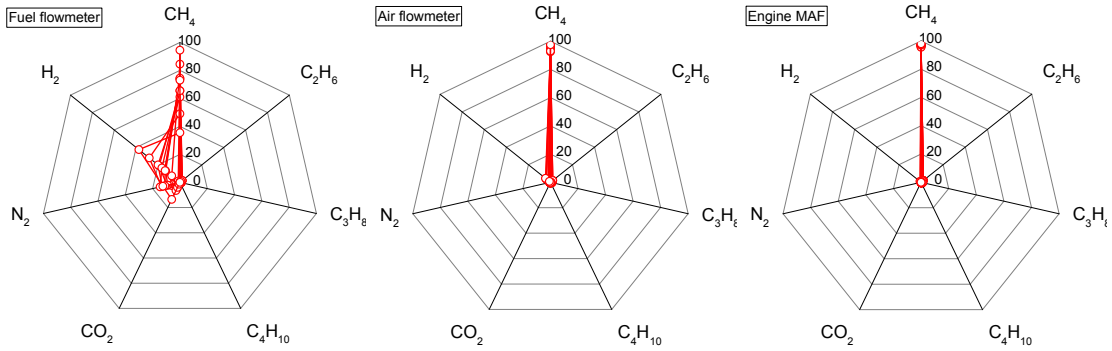

(a) (b) (c)

Figure 2.9 - Radar plot of the 10 'best mixtures' composition in vol. %, considering the G20 fuel with the different measurement devices: fuel flowmeter (a), air flowmeter (b), Engine MAF (c).

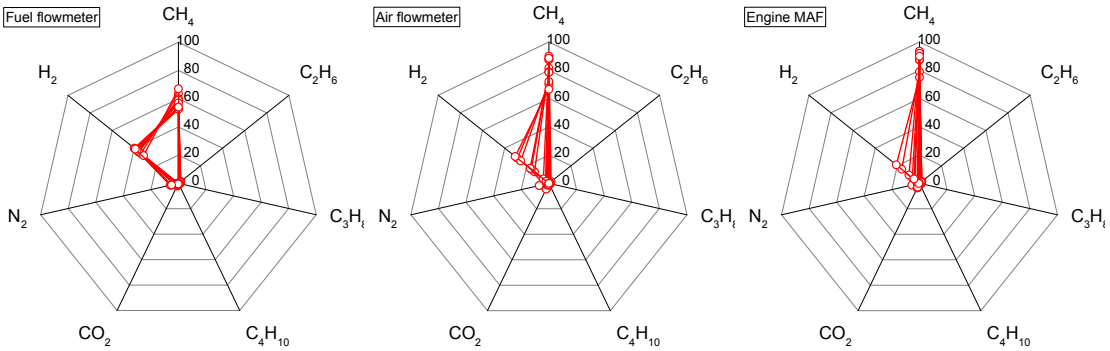

(a) (b) (c)

Figure 2.10 - Radar plot of the 10 'best mixtures' composition in vol. %, considering the HCNG30 fuel with the different measurement devices: fuel flowmeter (a), air flowmeter (b), Engine MAF (c).

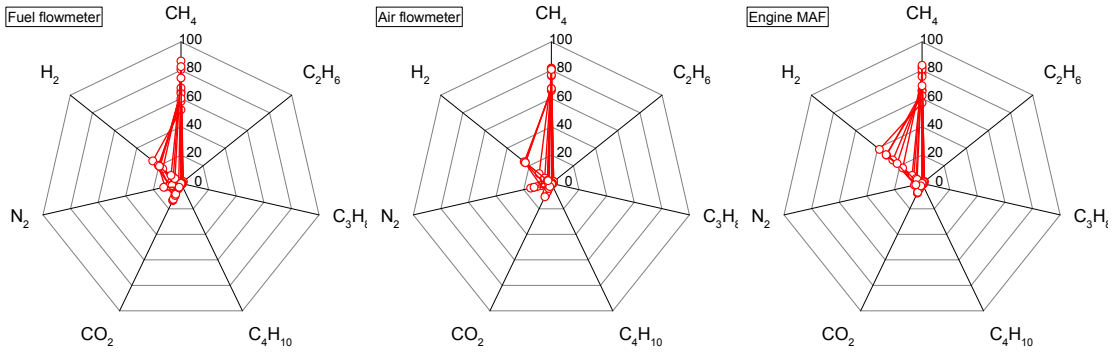

(a) (b) (c)

Figure 2.11 - Radar plot of the 10 'best mixtures' composition in vol. %, considering the G25 fuel with the different measurement devices: fuel flowmeter (a), air flowmeter (b), Engine MAF (c).

The colored area in the marginal plot in Fig. 2.12 represents the mixtures (2'335'230) considered in the full factorial set. The limits of the area in the vertical and the horizontal directions correspond to the extreme values of $K \cdot \alpha_{st}$ and K, respectively, whereas the upper and right histograms represent the probability distribution of the blends versus K and $K \cdot \alpha_{st}$, respectively. The percentage values of the probability distributions are not relevant, and have therefore not been reported in Fig. 2.12. The red points correspond to the ten sample blends shown in Table 2.4 (GPL is not present because it is outside the boundaries of the full factorial set, see Table 2.7). When one blend is close to the vertical (e.g. CH4) or the horizontal (e.g. HCNG30) limits of the area, a reduced number of mixtures have the same $K \cdot \alpha_{st}$ or K value, respectively, as can be discerned from the corresponding histogram. If the considered mixture is far from the limits (e.g. G25), there are several mixtures with different compositions that have the same K and $K \cdot \alpha_{st}$ values. Therefore, the probability of the 10 'best sample blends' having a significantly different composition from one another is really high, and each measurement device (air or fuel flowmeter) may not able to match the correct reference blend when considered on their own.

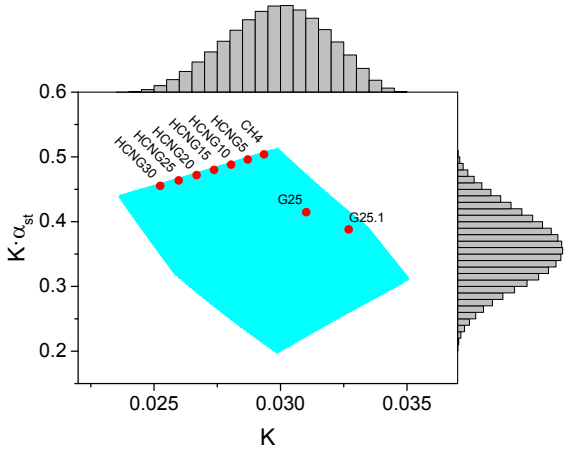

Figure 2.12 - Marginal plot that reports the probability distributions of the 2'335'230 blends as functions of K and $K \cdot \alpha_{st}$. The red points correspond to the reference blends shown in Table 2.4.

The two measurements have been combined, and the sum of the two $RMSEt_{inj}$ has been evaluated and plotted as a function of both K and $K \cdot \alpha_{st}$ in the contour plot in Fig. 2.13. The vertical red line represents all the mixtures that would provide the same minimum error, if the fuel measurement (which corresponds to the K value reported in the figure) were considered alone, whereas the blue horizontal line represents all the mixtures that would provide the same minimum error if the air measurement (corresponding to the $K \cdot \alpha_{st}$ value reported in the figure) were considered alone (in this case the test cell flowmeter was considered). The upper plot represents $RMSEt_{inj,}$ as a function of $K,$ along the horizontal blue line of the contour plot. Similarly, the plot on the right represents the $RMSEt_{inj}$ trend, as a function of $K \cdot \alpha_{st,}$ along the vertical red line of the contour plot. Therefore, when the two measurements are combined, the 10 'best mixtures' have a similar composition, as can be discerned from the contour plot shown in Fig. 2.13, and from the radar plot in Fig 2.14. In addition, it is possible to confirm that the composition of the real G25 fuel is not so different from the 10 'best mixtures' found by the method, as can be confirmed from the square point close to the intersection of the two straight lines in Fig. 2.13, and from the composition represented by the black polygon in the radar plot in Fig 2.14.

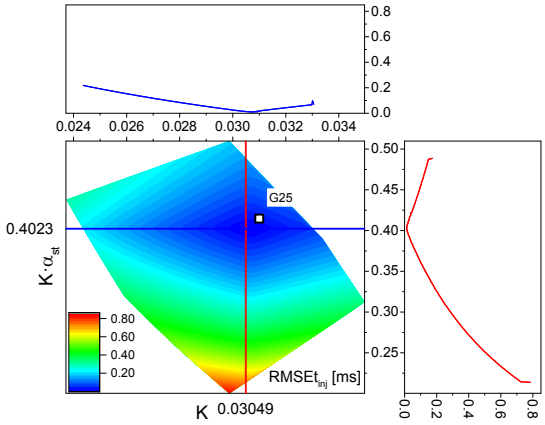

Figure 2.13 - Contour plot with the cumulative $RMSEt_{inj}$ in ms (obtained as the sum of the fuel and air flow rate measurements) as a function of K and $K \cdot \alpha_{st}$.

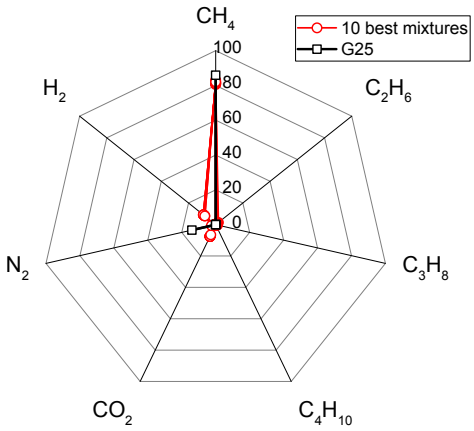

Figure 2.14 - Radar plot of the 10 'best mixtures' composition in vol. %, (round red points) found considering the G25 fuel with the two combined fuel flowmeter and air flowmeter measurements, and real composition of G25 (square black points).

2.4.4.3 Input variation analysis

In the present section a systematic variation of the inputs and the related consequences on the output will be investigated with reference to a binary fuel blend of hydrogen and methane, namely HCNG25 in this case. For other mixtures similar results were obtained. With reference to the section of the model implementation, the injection duration is evaluated as:

$$t_{inj} = \frac{1}{B}\left(\frac{m_{inj}}{G} - A - C \cdot V_{batt}\right)$$

So that for a given sample blend, for which the composition is fixed, the main contribution to the computed t_{inj} is due to V_{batt}, p_{rail}, t_{rail} (both accounted in the term G) and to m_{inj}. It is worth to further highlight that a direct measurement of the injected flow rate is available when the fuel flow meter is used as measuring device, while when an air flow rate measurement is exploited, its value has to be divided by the α_{st} evaluated from the sample blend.

Table 2.8 reports the relative mean deviation between t_{inj} calculated with the reference conditions, i.e. without any input perturbation, and with systematic error of -10% introduced on the relevant inputs. The systematic errors show similar effects independently from the method used for evaluating t_{inj}. Since p_{rail} affects the term G (ref. Eq.3a), see the appendix section for more details on G term, it represents the biggest contribution to a possible deviation in t_{inj}. This suggests that dynamic pressure waves that creates in the tube that connects the rail and the injector can interfere with the proposed method since the actual pressure upstream of the injector will not be the one captured by the rail pressure sensor. The sensitivity on the measured fuel and air quantity is quite remarkable, and it has a similar effect for the three flow measurement in terms of t_{inj} deviation, with a value around 8.36%. So that the method proved to be robust when different measurement methods are evaluated. Anyway, it is important to highlight that while test cell fuel flow meter has a certified accuracy of ±0.35% of the measured value and the test cell air flow meter of ±1% of the measured value, the engine MAF is the most inaccurate device, with an accuracy in the order of some percentage points (unfortunately precise calibration data were not available, because this is the engine sensor). This is also confirmed by results in Table 2.6, in which the method based on the engine MAF is actually the less precise one. The battery voltage effect shows a lower impact on t_{inj}, around 3%, when compared to the other analyzed effect. The regression function used to interpolate the signals and to compute the t_{inj} has been built taking into account a wide distribution of V_{batt}, so that even larger deviations

Table 2.8 – Mean deviations on t_{inj} between the reference case and a systematic error introduced on relevant inputs for the three tested methods.

	t_{inj} deviation [%]		
	Fuel flow meter	Air flow meter	Engine MAF
V_{batt}-10%	3.07	3.10	3.09
p_{rail}-10%	9.29	9.28	9.29
t_{rail}-10%	-0.54	-0.54	-0.54
m_{inj}-10%	-8.36	0.00	0.00
m_{air} -10%	0.00	-8.35	0.00
$m_{air,MAF}$ -10%	0.00	0.00	-8.36

on the battery voltage are reliably contemplated and they do not represent a major problem.

In addition, the nominal reference blend composition has an impact on the estimated t_{inj}. It has been verified that varying the H_2 volume content of just 0.5% from the nominal value of 25% produce a sensible error ranging from 0.15 to 0.23% on t_{inj}. It has been further computed that on binary HCNG mixture a variation of the H_2 volume content of 5% (which is the interval adopted for sample blend as reported in Table 2.4), implies a variation of t_{inj} of about 2.5%. This presupposes that, fixing the other inputs, the measured fuel or air mass rate should be acquired with a minimum accuracy of roughly 2.5% if a binary mixture has to be recognized correctly with a step of 5% on H_2 content. If the instrument is not accurate enough, as it could happen when the engine MAF is used, the admissible step of H_2 has to be increased.

The afore-mentioned effects are quantified on the blend identification algorithm side, while other uncertainties are introduced on the experimental side. The first, and most important one, is the real mixture composition that can vary significantly even when certified blends are employed, as in this case. It has been computed that, considering the ranges of constituents of the certified blend, varying the mixture composition within these ranges can lead to a maximum deviation of 6% in terms of α_{st}. In other words, the same certified mixture could produce an α_{st} with an error of ±3%. This effect is much bigger than the deviation introduced by the ECU oxygen sensor, that, when working in closed loop and stoichiometric conditions as in this case, establish a limit cycle in order to let the three-way catalyst work correctly, with oscillations around 1% with respect to the stoichiometric value. Tests have been made also in lambda open loop control, to check if strong corrective actions are implemented by the ECU when working in closed loop, but results does not show a major correction in terms of t_{inj}. Anyway, other possible adjustments of the ECU on the t_{inj} can interfere with the proposed method, especially during transient operations, but in this case they have been considered lower than other sources of error and hence they do not have been taken into account in the proposed work.

2.4.5 Appendix: blend properties calculations

The blends (see Table 2.2 and 2.4) are considered to be mixtures of different gaseous species of known composition. The molecular mass M, the specific heats at constant pressure c_p and volume c_v are assumed as known values of each generic chemical species x. In the present discussion, the following species have been considered in the composition of the different blends (but the calculation can easily be extended to a larger number of constituents): methane, ethane, propane, butane, carbon dioxide, nitrogen and hydrogen. a, b, c, d, e, f and g are the corresponding volume percentages, whose sum is equal to 100 for each blend.

Therefore, the stoichiometric A/F ratio α_{st} of each blend can be evaluated, considering the following combustion equation under stoichiometric conditions:

$$a \cdot CH_4 + b \cdot C_2H_6 + c \cdot C_3H_8 + d \cdot C_4H_{10} + e \cdot CO_2 + f \cdot N_2 + g \cdot H_2 + L \cdot (O_2 + \varphi N_2) \rightarrow \\ \rightarrow A \cdot CO_2 + B \cdot H_2O + D \cdot N_2$$

in which φ=3.773 is the ratio between the molecular nitrogen and oxygen in the combustion air. The capital letters represent unknown quantities that have to be evaluated.

A balance equation is written for each chemical species:

Carbon C: $A = a + 2b + 3c + 4d + e$

Hydrogen H: $2B = 4a + 6b + 8c + 10d + 2g$

Nitrogen N: $2D = 2f + 2L\varphi$

Oxygen O: $2e + 2L = 2A + B$

and the following is obtained:

$$B = 2a + 3b + 4c + 5d + g$$

$$L = \frac{2A + B - 2e}{2} = \frac{4a + 7b + 10c + 13d + g}{2}$$

$$D = f + L\varphi = f + \frac{4a + 7b + 10c + 13d + g}{2}\varphi$$

and hence

$$\alpha_{st} = \frac{L \cdot (M_{O2} + \varphi M_{N2})}{a \cdot M_{CH4} + b \cdot M_{C2H6} + c \cdot M_{C3H8} + d \cdot M_{C4H10} + e \cdot M_{CO2} + f \cdot N_2 + g \cdot M_{H2}}$$

The average molecular mass of the blend is evaluated from the corresponding volume percentage $[x]$:

$$\bar{M} = \frac{\sum_{x=a}^{g} [x] \cdot M_x}{100} = \frac{a \cdot M_{CH_4} + b \cdot M_{C_2H_6} + c \cdot M_{C_3H_8} + d \cdot M_{C_4H_{10}} + e \cdot M_{CO_2} + f \cdot M_{N_2} + g \cdot M_{H_2}}{100}$$

whereas the mass percentage $\{x\}$ of the generic species is:

$$\{x\} = \frac{[x] \cdot M_x}{\bar{M}}$$

Therefore, the lower heating value of each blend is:

$$LHV = \frac{\sum_{x=a}^{g} LHV_x \cdot \{x\}}{100}$$

In addition, it is possible to evaluate the gas constant, R, and the specific heat, c_p, for each blend:

$$R = \frac{\mathscr{R}}{\bar{M}}$$

where $\mathscr{R}$ = 8314.4 J/kmol is the universal gas constant

$$c_p = \frac{\sum_{x=a}^{g} c_{p_x} \cdot \{x\}}{100}$$

Finally:

$$\gamma = \frac{c_p}{c_v} = \frac{c_p}{c_p - R}$$

2.5 Final remarks

The research work proposed in the first part of this chapter focused its attention on the performance of a SI engine fuelled with different blends on methane and hydrogen enriched methane (HCNG) with the specific aim of highlighting the differences that would arise if the engine ECU should maintain the parameters for G20 operations. More specifically, attention was drawn to the effects carried by the use of different mixtures that would eventually reproduce the variety of compositions which characterize biogases.

Improved combustion parameters were achieved when hydrogen was added to methane. Still, the higher in-cylinder pressure determined by the advance combustion might bring to the failure of some of the crank slider mechanism components. Moreover, the improper phasing of the combustion process are likely to negatively affect the turbocharger group performance. Finally, a small deterioration in the engine mechanical efficiency was observed in the low speed range, mainly to be ascribed to the higher PFPs. Contrariwise, G25 operations were characterized by an evident decrease in the engine power performance connected to the replacement of methane with inert gases. Furthermore, the synergic effect of a retarded combustion together with a reduced burning speed shifted the

combustion process towards the exhaust valve opening, thus preserving the exhaust gas temperatures abatement which characterized HCNG operations.

Regardless of the specific modification in the engine output and in the combustion related parameters, the experimental results assessed for the need for dedicated ECU parameters capable of both making up for the drawbacks carried by the use of a different mixture with respect to the original one as well as better exploiting the mixture chemical and physical characteristic. Given the wide range of composition led by the biogas production, researchers should concentrate their effort into designing a solution to automatically detect the composition of the mixture the engine is running on so as to consequently and instantaneously adjust the ECU settings.

In the second part, a method has been presented for the estimation of the composition of natural gas/biogas/hydrogen fuel blends for CNG engines. As the composition of a real blend can vary to a great extent at the refueling pump and it is not known a priori, the behavior and performance of an engine can also be affected. Therefore, the evaluation of the composition is necessary to set the proper calibration in the engine ECU.

In order to replicate the actual condition after vehicle refueling and engine switch on, a CNG engine was fueled with 5 different fuel blends and was run at mainly low load and low speed in steady-state working conditions. As the number of calibration that can be implemented in the ECU is limited, a set of 10 sample blends was considered to replicate the broad range of fuels that could ideally be fed to the engine.

The method considers the injection time measured by the ECU and the fuel or air flow rate measurements performed at the test bench or through vehicle instrumentation. The injector was characterized by considering a subset of the available data to obtain a linear regression model, in which the injection time was evaluated as a function of the injected mass, rail pressure and temperature, battery voltage, and fuel properties. The remaining data were used to validate the model results.

The main outcomes of the recognition method can be summarized as:

- The method proved to be able to detect the correct match between the actual fuel and the corresponding sample blend. The model is really accurate when data from the test cell instrumentation are given as inputs

to the model. Taking into account data from a conventional mass air flowmeter for automotive applications, the methodology has proved to correctly recognize the actual fuel blend within the candidate set, with a maximum error of 5% on hydrogen volume content when HCNG mixtures are considered.

- The model has been applied to an increasing number of different steady-state working conditions ordered randomly, considering a first set of sample mixtures that featured quite evident differences in the optimal ECU parameters. Convergence was generally reached with less than 10 test points, regardless of which blend and working conditions were considered, and of whether the fuel or air flow measurements were used. Therefore, in the present version, the model provides a high potential for real-time on-board application on an engine ECU after tank refueling.
- The methodology has been further extended by considering a set of full factorial sample mixtures (2’335’230). It was shown that, for certain kinds of tested mixtures, e.g. G25, extremely different sample compositions can be compatible with the injection time of the real blend measured by the ECU when only one of the measurement devices is employed, namely the air or fuel flow rate. However, if these two different measurements are combined, a good match can be found between the sample and the real blend.

Chapter 3

Implementation of PCCI combustion mode in a conventional diesel engine

3.1 Preface

This second part of the thesis is dedicated to the implementation of PCCI combustion on a Euro VI heavy-duty production engine. The results hereby presented have been published in [74-76]. This work represents the first step to be accomplished with the aim of replacing the conventional engine hardware with an optimized configuration for PCCI combustion.

Advanced combustion strategies in diesel engines have been studied to simultaneously diminish particulate matter (PM) and nitrogen oxides (NOx) exhaust emissions in order to reduce the complexity of after-treatment systems.

The implementation of a premixed-charged compression ignition (PCCI) strategy is based on the lengthening of the ignition delay. In this work, a PCCI combustion mode, featuring a single "early injection" strategy, is applied to a Euro VI heavy-duty production engine, originally designed to run under conventional diesel combustion mode. Based on experimental evidence, the variables that mostly influence the ignition delay are the start of injection (SOI), the EGR rate and the fuel injection pressure.

Firstly, statistical techniques of the design of experiments have been applied in order to efficiently plan tests, analyze acquired data and provide cause-and-effect relationships about the observed phenomena. The experimental activity was realized accordingly to the following steps: (i) preliminary tests performed in order to identify which ECU variables were more relevant to reach the desired combustion mode and corresponding variation ranges; (ii) statistical design of experiments based on preliminary test results; (iii) execution of experiments on

engine test-bench; (iv) evaluation of regression models to predict desired outputs (emissions, fuel consumption, combustion noise) as a function of selected inputs; (v) model-based optimization to provide suitable input values to reach desired output targets; (vi) experimental validation of the model outputs and optimal points.

The outcomes relative to one engine working point (engine speed and load are n=1800 rpm and bmep=1 bar, respectively) are here presented to show the considered methodology. Thanks to the optimal calibration of the PCCI combustion, a significant reduction in NOx and soot emissions has been achieved (up to 90% and 99%, respectively). However, a fuel penalty of 9-13% and an excessive increase in HC and CO have been registered.

As a second step, different combustion control strategies have been experimentally tested. In particular, closed-loop pressure-based and open-loop model-based techniques, able to perform a real-time control of the center of combustion (MFB50), have been compared with the standard map-based engine calibration in order to highlight their potentialities. In the pressure-based technique, the instantaneous measurement of in-cylinder pressure signal is performed by a pressure transducer, from which the MFB50 can be directly calculated and the start of the injection of the main pulse (SOI_{main}) is set in a closed-loop control to reach the MFB50 target, while the model-based approach exploits a heat release rate predictive model to estimate the MFB50 value and sets the corresponding SOI_{main} in an open-loop control.

The experimental campaign used for testing the combustion controls involved both steady-state and transient tests. The three control techniques were compared in steady-state tests under various conditions, featuring standard as well as PCCI combustion mode, different kinds of fuels, a disturbance added to the pressure signals from in-cylinder transducers (to simulate the effect of an aged or low-cost pressure transducer) and an injector with a reduced mass flow rate mounted on one cylinder. The behavior of the three controls was tested in transient conditions as well, analyzing in particular fast load and speed ramps.

The above mentioned testing conditions were performed to evaluate the robustness of the pressure-based and model-based techniques compared to standard calibration map-based control and their outcomes in terms of engine operation stability.

The proposed real-time combustion control techniques provided fuel consumption and emissions in line with the conventional map-based control. In addition, they lead to an improvement in combustion stability, which can be an important issue especially when transient operations are considered or when non-conventional combustion modes, such as PCCI, are implemented.

3.2 Experimental set-up

The engine used in the present study, whose main specifications are listed in Table 3.2, is a single-stage turbocharged, four-cylinder, four-stroke heavy-duty Euro VI diesel engine by FPT Industrial (Fig. 3.2). The engine is equipped with a high-pressure common-rail injection system and a variable-geometry turbine (VGT). The EGR system is a short-route cooled system, where the EGR flow is driven by the pressure difference between the exhaust and the intake pipelines, adjusted by the EGR valve and an exhaust flap positioned downstream the turbine to increase the pressure in the exhaust, as the engine is not endowed with a throttle valve in the intake manifold.

The tested engine is fully instrumented with low-frequency piezo-resistive pressure transducers and thermocouples to measure, on a time basis, the pressure and temperature at different positions of the flow path (such as upstream and downstream the compressor, the turbine and intercooler, in the intake manifold and in the EGR circuit). Thermocouples are also installed to measure the temperatures in front of each cylinder in the intake and exhaust manifolds. Four Kistler 6058A high-frequency piezoelectric transducers are placed in glow-plug adapters to acquire for each cylinder, on a crank basis, the in-cylinder pressure time-histories, which are used as an input for the pressure-based MFB50 control by means of rapid prototyping device by AVL. The in-cylinder pressure traces are pegged on the basis of the intake pressure that is measured by means of a high-frequency Kistler 4007C piezo-resistive transducer, located in front of cylinder #1. On the same cylinder, but on the exhaust side a high-frequency cooled Kistler 4049B piezo-resistive transducer is also installed.

Table 3.2– Main specifications of the tested engine

Engine type	3.0L Euro VI 16V
Displacement	2998 cm^3
Bore / stroke	95.8 mm / 104 mm
Connecting rod	158 mm
Compression ratio	17.5
Valves per cylinder	4
Turbocharger	Single-stage with VGT
Fuel injection system	Common Rail, solenoid injectors

The experimental tests were carried out at the dynamic test bed installed at the Politecnico di Torino ICEAL (Internal Combustion Engines Advanced Laboratory). The test bench is equipped with a cradle-mounted AC dynamometer and an 'AVL KMA 4000' fuel flowrate system, used to continuously measure the engine fuel consumption with an accuracy of 0.1%; the raw engine-out gaseous emissions are measured by means of an 'AVL AMAi60' endowed with two complete trains equipped with devices for the simultaneous measurement of gaseous concentrations of HC, CH_4, NO_x/NO, CO, CO_2 and O_2 both at the intake and exhaust manifolds. Finally, for the soot measurement an 'AVL 415S' smokemeter is used for steady-state tests whereas an 'AVL 439' opacimeter is adopted for transient tests.

All of the abovementioned measurement devices are controlled by a PUMA Open 1.3.2 and IndiCom automation system. The CAMEO software is used for automatic tests, related for instance to design of experiments analysis.

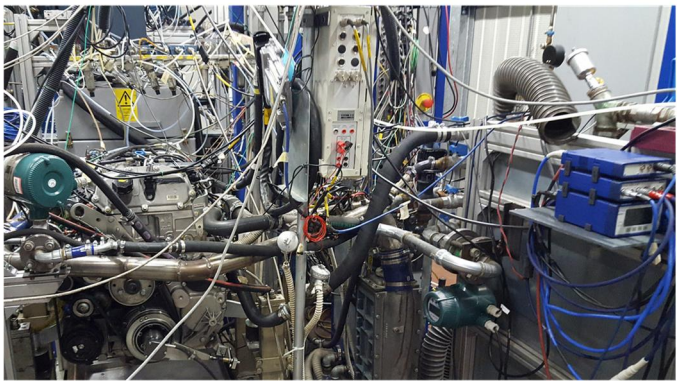

Figure 3.2 - FPT F1C 3.0L Euro VI diesel engine installed on the dynamic test bench at the Politecnico di Torino. The rapid prototyping device can be seen on the right.

3.3 Preliminary optimization of PCCI combustion mode

3.3.1 Model based calibration methodology

The increasing complexity of the phenomena involved in the engine technology makes the task of optimal calibration complex and challenging. As a result, there is a growing realization that model-based approaches, using modern Design of Experiments (DoE), statistical modeling and optimization techniques, can simplify and efficiently produce high quality calibrations for engines [77].

First of all, properly designed experiments have to be planned, since experiments can be expensive and time consuming. For this purpose, DoE is an efficient technique and can lead to significant reduction of the empirical data collection at the test bench. Experiments are expressed in terms of 'factors', which are the independent input variables varied at each test point in order to understand the effect on the dependent parameters, known as 'responses' [78]. After the selection of the most influent factors, based on the physical knowledge of the system under investigation, specific values, or 'levels', have to be determined, in order to specify a 'level-combination' for each experimental test which has to be run at the test bench: therefore, basically, an experimental design can be represented as a matrix, where each row represents an experimental run and each column gives a particular factor level [79]. A work involving experimental designs can choose between different types of design of experiments, for example classical (which include full factorial, central composite designs, etc.), space-filling, and computer-generated optimal designs [79]. In any case, the empirical tests obtained with DoE can be analyzed and provide proper data to create the statistical models that relate the experimental input factors to the measured response outcomes [80].

The next steps are to choose an approximating model and a fitting method. Many alternative models and methods exist, but probably the simplest is the Response Surface Methodology (RSM), with the use of second-order polynomial models as response surface approximating functions and of the least squares regression analysis as fitting methods [78].

If the built regression models show a good fit, they can be used to generate the optimal calibration, applying optimization techniques in order to find which input values are needed to obtain certain outputs within a feasible area bounded by properly setting constraints [77, 79].

In this study, a "V"-optimal experimental design algorithm and optimization techniques [77, 79] were applied at different steady-state speed and torque conditions, in order to define optimum calibrations of SOI, EGR rate and boost pressure to run the engine under PCCI combustion mode, meeting various constraint criteria. In particular, the focus has been to reduce the smoke and NO_x exhaust emissions from the engine accepting some penalties in terms of CO and HC exhaust emissions and bsfc. Results relative to one engine working point, namely at engine speed n = 1800 rpm and brake mean effective pressure bmep = 1 bar corresponding to 27 Nm in the tested engine, will be presented.

3.3.2 Preliminary experimental analysis on PCCI combustion

A preliminary test activity has been conducted in order to identify the main engine control variables which can be managed in order to obtain a PCCI combustion strategy.

In a conventional diesel combustion the mixture ignites where the local equivalent ratio is between 4 and 2 [61], i.e. in fuel-rich conditions. The target of PCCI combustion strategies is to ignite the charge at much lower local equivalent ratios in order to reduce the formation of soot and to reduce the combustion temperature to avoid the formation of NOx: in fact, soot is produced for local equivalent ratios higher than 2 and for temperature ranging from 1500 K to 2500 K while NOx are produced for temperatures above 2200 K [81]. According to the known literature [54, 82, 83], the realization of PCCI combustion conditions basically deals with the increase of the ignition delay, i.e. of the time period between the start of ignition (SOI) and the start of combustion (SOC). During this time interval the injected fuel atomizes, vaporizes and mixes with air before reaching the auto-ignition conditions. The duration of the ignition delay depends on charge

density, fuel and oxygen concentrations and in-cylinder temperature [55]. Given a certain engine working point, the oxygen concentration and in-cylinder temperature are strongly affected by the EGR rate. This definitely sets the EGR as the most important engine working parameter for the realization of PCCI combustion.

Considering direct injection engines, SOI timing also plays an important role. PCCI combustion strategies usually deal with a very early [55-58] or late [59] combustion events. In the first case the in-cylinder charge density and temperature at SOI are relatively low, which increases the time available for the charge to mix but also increases wall impingement phenomena, while in the latter case (late injection) the fuel is injected just after the TDC with high charge density, which further requires additional EGR to increase the ignition delay. The potentialities of these two strategies with respect to the reduction of the local equivalence ratio and of the combustion temperatures are clearly shown in [84]. The fuel injection pressure may have an impact as well since it affects the fuel atomization process, but it also has an effect on the liquid length penetration and therefore on wall impingement.

Moreover, a reduction in the intake air temperature and a pressure increase by means of the turbocharger would be beneficial to increase the ignition delay while reducing wall impingement [85]. Further improvements may be obtained by increasing the mixing rate through a design which enhances the swirl motion, and properly shaping the combustion chamber geometry and the injectors [58].

The experimental activity presented in this work was carried out on a commercial engine, with a defined geometry of the combustion chamber, of the injector flow path and of the turbo-group. Definitely the main engine control variables which can be used to manage PCCI combustion mode are the EGR rate and the injection timing. An early injection strategy with a single injection event has been chosen as starting activity. Furthermore, different levels of fuel injection pressure have been analyzed, but this variable has been found to have a minor effect in the considered range therefore it has not been taken into account in the following discussion. Preliminary tests were executed on the reference engine working points by gradually changing these variables with a “one-factor-at-time” (OFAT) approach [79]. The limit values of these variables which allow the realization of a PCCI-like combustion event have been then identified as a preliminary step for the DoE activity. Lower limits for SOI and EGR were set taking into account the trends in the engine-out concentrations of NOx and soot: in normal combustion these two pollutants have generally opposite trends, while in PCCI/HCCI combustion it is

possible to obtain a simultaneous reduction of both of them. Higher limits for SOI were set to limit the increase of HC and CO emissions. The upper EGR rate limit is imposed by two phenomena: first, the increase of EGR rate above a certain amount generates high combustion instability and high cylinder-to-cylinder variations (due to the increase of the EGR unbalance); second, because the increase of EGR rate to very high values is obtained by wide opening the EGR valve and, at the same time, highering the engine backpressure by means of a dedicated flap valve, which degrades fuel consumption and, after certain levels, increases the combustion instability and the occurrence of misfiring due to the increased difficulties in managing the inlet and outlet flows from the cylinders.

The results of the preliminary tests are discussed with reference to Figs. 3.3-3.7. All the data are referred to a single engine working point, namely 1800 x 1 (being the first number the engine speed in rpm and the second one the bmep in bar). The choice of this working point is due to the fact that the tested engine has not been design to run under PCCI operation so it became extremely difficult to achieve higher loads while maintaining a stable combustion performance at the same time. In addition, the production EGR cooler was not design to withstand such high levels of EGR mass rates in terms of cooling performance. Preliminary tests have been performed by means of exhaust flap position sweep, between 94.7 and 96.7 %, at a constant SOI level, between 16 and 30 °CA bTCD. In order to obtain the highest EGR rate at the maximum achievable value of boost pressure, the EGR valve has been kept wide open and the VGT rack was set to fully closed position. The rail pressure was kept constant at 580 bar. The engine-out pollutants are considered in terms of brake specific emissions, evaluated as the ratio between the pollutants flow rate and the brake power. For confidentiality reasons, the figures are normalized with respect to a reference condition, i.e. the engine values according to the base engine map featuring a conventional diesel combustion mode. Soot emissions are evaluated starting from the measurement of the filter smoke number (FSN) according to [86].

Fig. 3.3a shows the soot vs. NOx emissions for various values of SOI, where the SOI is expressed in terms of crank angle degrees before TDC (°CA bTDC), while Fig 3.3b correlates soot emissions with the EGR rate. At constant NOx emissions, soot is reduced by advancing the injection event due to the longer mixing time. Given a certain value of SOI, soot increases with decreasing NO_x up to a certain point where soot start decreasing simultaneously with NO_x. This is obtained for high EGR rates and the specific EGR value at which the standard trend is inverted

depends on SOI. If the start of injection is set to 16 °CA bTDC this inversion does not occur even at the maximum possible EGR rate, therefore this condition cannot be considered suitable for PCCI combustion. For earlier injection events, e.g. when SOI occurs at 20 or 24 °CA bTDC, the simultaneous decrease of the two pollutants is obtained for higher EGR rates than 66%. Further advancing SOI, e.g. at 28 or 30 °CA bTDC, the soot emissions are almost null and therefore the corresponding variations are not significant.

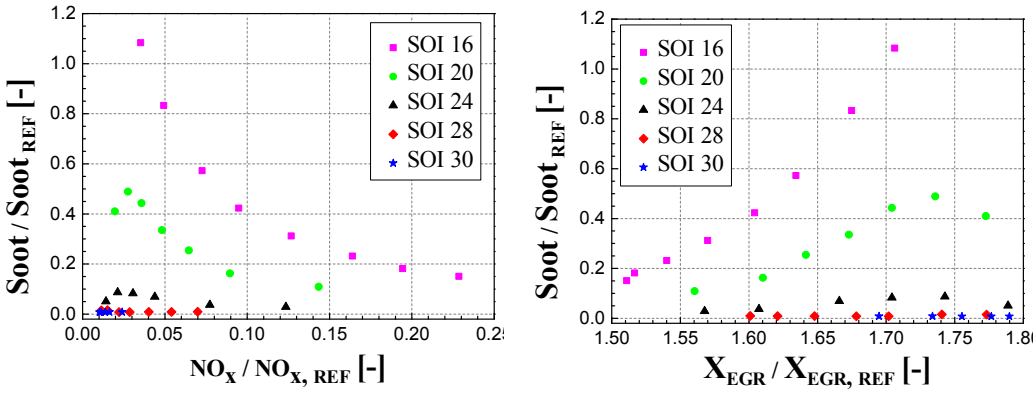

Figure 3.3 - . (a) Soot vs NO_x exhaust emissions at different SOI; (b) Exhaust soot emission vs EGR rate at different SOI

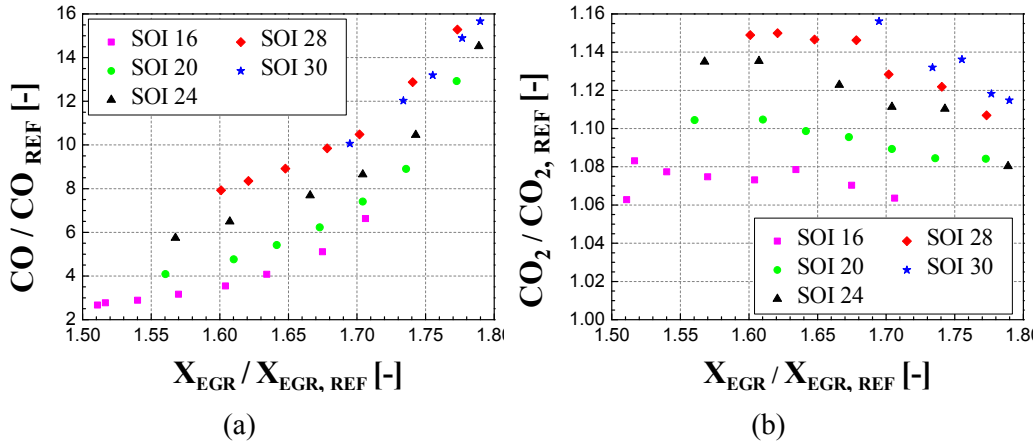

Figure 3.4 - . (a) Exhaust CO emission vs EGR rate at different SOI; (b) Exhaust CO_2 emission vs EGR rate at different SOI

On the other hand, Fig. 3.5a shows an increase in the brake specific fuel consumption with SOI due to an advance in the barycenter of combustion (ref. Fig. 3.6a), while the effect of the increase in the EGR rate is in general not significant for the tested conditions.

Moreover, the advanced injection in a low density and low temperature environment contributes to possible wall impingement and lean-charge pockets which determine an increase in CO (Fig 3.4a) and HC emissions which contributes to worsen the combustion efficiency. The HC emissions are not reported since they show a similar trend to that of CO, being HC roughly one fourth of CO: the increase in unburned hydrocarbons advancing the SOI reasonably may be also due to the increase in oil dilution phenomena and a general worsening of the fuel atomization process due to lower in-chamber density when the fuel is injected.

Furthermore the dilution effect of EGR contributes to the increase of HC and CO emissions. In these conditions, being HC and CO emissions extremely high, CO2 emissions (Fig. 3.4b) are not directly proportional to bsfc and tend to slightly decrease with the increase of the EGR rate for a given SOI value, although increasing the EGR rate produces an increase of the amount of CO_2 in the intake gases.

Figs. 3.5b-6 show the effect of EGR and SOI on the development of the combustion event in terms of barycenter of the mass fraction burned (MFB50), peak firing pressure (PFP) and combustion noise (CN). As a matter of fact, advancing the injection event cause an increase in the PFP while the increase in EGR slows the combustion development and reduces the corresponding PFP and the pressure rate, that highly affects the combustion noise (Fig. 3.6b); reduced variations are obtained for high values of EGR and high values of SOI. Furthermore, earlier SOI cause a shift of the combustion to lower crank angle values (as the MFB50 tends to be advanced), while the increase in the EGR rate tends to retard the combustion event; variations obtained changing the SOI for very early combustion events (e.g. curves related to SOI at 24, 28 and 30 degCA bTDC) are almost negligible. Therefore, a proper combination of the two control parameters can provide acceptable values of MFB50 (Fig. 3.6a).

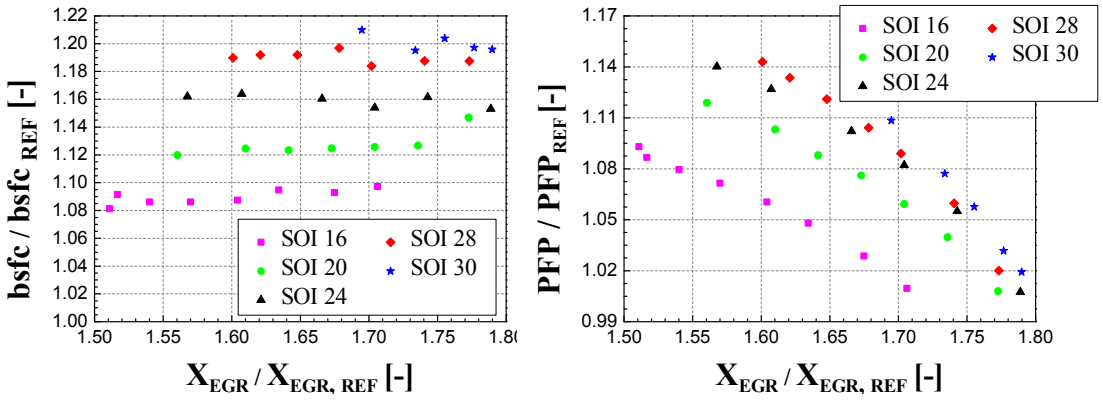

Figure 3.5 - (a) bsfc vs EGR rate at different SOI; (b) Peak firing pressure vs EGR rate at different SOI

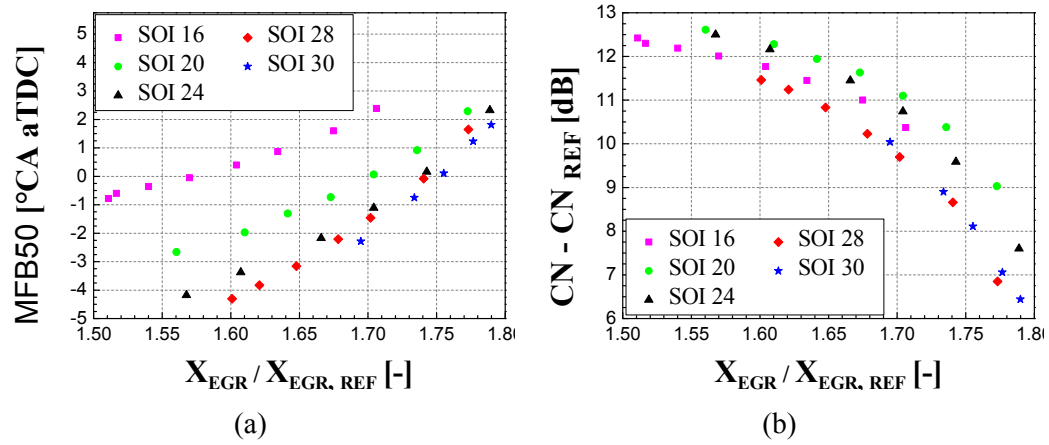

Figure 3.6 - (a) MFB50 vs EGR rate at different SOI; (b) combustion noise vs EGR rate at different SOI

Referring to the density of the intake charge, it is worth underlying that in real working conditions the favorable reduction of the intake temperature and the increase of the boost pressure are competing with the increase in the EGR rate. In fact, the higher is the amount of exhaust gas recirculated in the intake manifold, the higher would be the temperature of the air-EGR mixture (Fig. 3.7a). Moreover, since the engine is equipped with a short-route EGR system, the higher is the EGR rate the lower is the flow rate through the turbine blades and – as a consequence – the lower would be the work available for compressing the fresh air and therefore the lower would be the boost pressure (Fig. 3.7b).

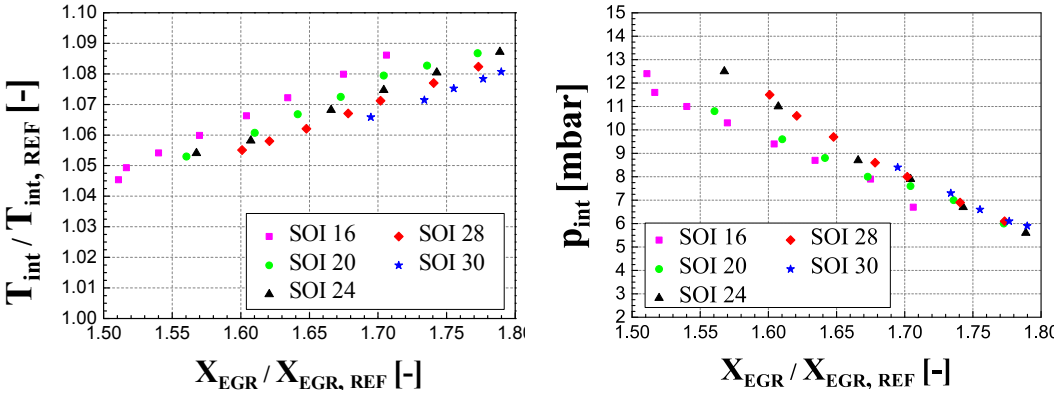

(a) (b)

Figure 3.7 - (a) Intake manifold temperature vs EGR rate at different SOI; (b) Intake manifold pressure vs EGR rate at different SOI

3.3.2 Design of experiments and Model-based optimization of PCCI combustion

According to the preliminary analysis above presented, the limit values of the input parameters for the execution of a DoE have been set and are reported in Table 3.3. The following input parameters were considered as the main ones appreciably affecting PCCI combustion: the rail pressure, the start of injection and the position of the backpressure flap valve to regulate the EGR rate, since the EGR poppet valve was fully open in all the PCCI working conditions. Given the limit values for each of these variables and provided a number of levels, a "V-optimal" design, which minimizes the values of the predicted error variance in the test plan, has been implemented by means of the Matlab software tool 'MBC model'. A number of 32 tests have been executed based on this DoE. Moreover a number of repetitions of the central point have been evenly run during the test plan in order to check possible drifts.

Table 3.3 - DoE inputs boundary values

Input	Lower Limit	Upper Limit
EGR flap position	85	95
SOI (°CA bTDC)	18	30
Rail pressure (bar)	500	700

The following variables were considered as relevant parameters: bsfc, brake specific emissions (NO_x, Soot, HC and CO), CN and MFB50. These have been set as output of the linear models which have been built fitting the experimental values as polynomial functions of the second order of the input control variables (rail pressure, SOI, EGR flap position). The Box-Cox transformation [87] has been applied where necessary in order to normalize the distribution of the residuals. Moreover the method of the "stepwise regression" [79] has been used to eliminate from the models those regressors which have a negligible effect on the output. Summary statistics of the obtained models are reported in Table 3.4. According to the reported statistical indexes the models show a good correlation with the experimental values. As an example of the results obtained with modeling, Fig. 3.8 depicts the predicted bsfc versus the experimental one. A space-filling DoE [79], which allows to cover almost homogeneously the 3-dimensional space generated within the limits of the three input variables. The validation root mean square error (RMSE), obtained comparing the validation tests with the models, is also reported in Table 3.4 and is generally very similar to the model RMSE.

Table 3.4 - Statistical summary for each response model

Response model	Parameters	R^2	R^2 adjusted	PRESS R^2	PRESS RMSE	RMSE	Validation RMSE
bs HC (g/kWh)	8	0.960	0.951	0.933	0.161	0.140	0.184
bs NO_x (g/kWh)	8	0.994	0.992	0.989	0.346	0.268	0.282
bs CO (g/kWh)	8	0.983	0.980	0.973	1.071	0.879	0.633
bs Soot (g/kWh)	10	0.880	0.837	0.749	0.002	0.001	0.001
bsfc (g/kWh)	8	0.938	0.925	0.913	2.537	2.392	3.616
CN (dB)	7	0.977	0.973	0.957	0.132	0.106	0.095
EGR rate (-)	6	0.996	0.995	0.994	0.411	0.369	0.494
MFB_{50} (°CA)	8	0.998	0.997	0.995	0.190	0.148	0.177

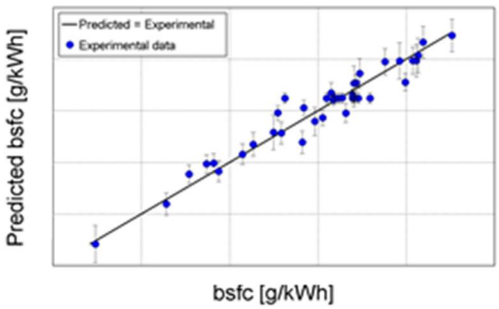

Figure 3.8 - *bsfc: predicted vs. experimental values*

Once the predictive models have been validated, a model-based optimization of the PCCI combustion in the studied engine working point has been realized. Different optimization strategies have been used and tested for comparison. In particular, the focus has been set on the minimization of the NOx emissions or of the bsfc, possibly setting some upper boundaries to other output parameters. A 'conjugated gradient optimization' method has been adopted in case of single-objective optimizations, while multi-objective optimizations have been computed employing a Normal Boundaries Intersection (NBI) algorithm. Details on the settings used for the various optimizations are reported in Table 3.5.

Table 3.5 - Euro VI point and optimization points parameters

Point	EGR valve	EGR flap	SOI	Rail pressure	Minimization	Constraints
	(%)	(%)	(°CA bTDC)	(bar)		(-)
Euro VI	100	71.4	6.9	583		
Opt 1	100	95.0	30	700	NO_x	
Opt 2	100	95.0	30	500	NO_x	$CO/CO_{REF} < 8.5$
Opt 3	100	91.5	18	500	bsfc	$NO_x/NO_{X,REF} < 0.5$ $Soot/Soot_{REF} < 0.4$
Opt 4	100	95.0	21	500	NO_x bsfc	$HC/HC_{REF} < 2$ $Soot/Soot_{REF} < 0.2$

Figs. 3.9-3.12 show a comparison between the optimized PCCI combustion modes with the base engine calibration featuring a conventional diesel combustion mode. The figures are referred to the results of the experimental tests executed on the base of the model-based optimization.

The first and second optimizations (Opt 1 and Opt 2) are obtained minimizing the NOx emissions, which produced a reduction of the NO_x brake specific emissions of more than 90% with respect to the base calibration (Euro VI) and a smokeless combustion thanks to an increase of the EGR rate to more than 60%. On the other hand, CO and HC emissions increase more than 2 times and 8 times with respect to the reference, respectively. Although the bsfc increases by 13% due to an advance of the barycenter of the combustion of more than 11 °CA.

The third optimization has been computed in order to minimize the brake specific fuel consumption and results to be the best trade-off obtained for the tested conditions: in this case it is possible to reduce the NO_x emissions by 60% and the soot by more than 80%, while the bsfc penalty is roughly lower than 10%, the increase in CO is contained to less than 3 times and the HC emissions are almost the same as the reference condition. According to the model-based optimization results, the fourth optimization point should minimize at the same time NO_x emissions and bsfc while limiting HC and soot emissions to constrained levels.

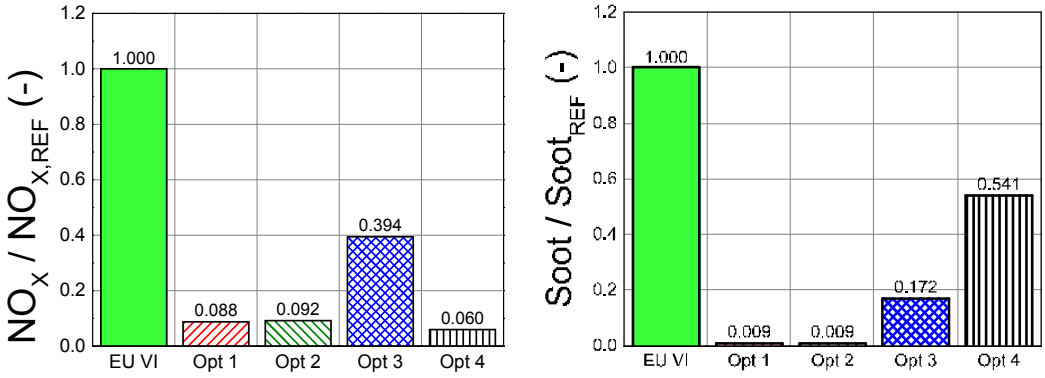

(a) (b)

Figure 3.9 - NOx and soot brake specific emissions: comparison between the base EU VI calibration and the optimized PCCI points

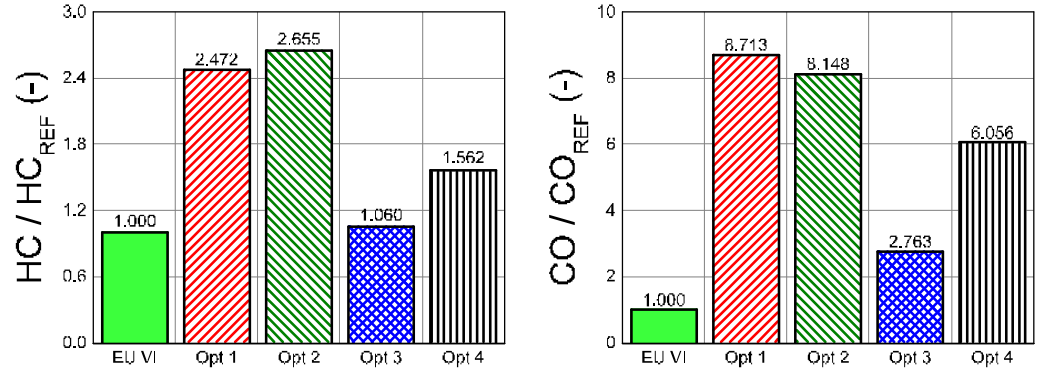

(a) (b)

Figure 3.10 - HC and CO brake specific emissions: comparison between the base EU VI calibration and the optimized PCCI points.

Experimental tests showed that the NOx levels are even lower than Opt 1 and Opt 2, while the bsfc is slightly higher than in Opt 3, and HC and CO are considerably lower with respect to Opt 1 and Opt 2 but much higher than Opt 3. Soot emissions are reduced by 46% with respect to the base point, but definitely far from the target of a PCCI-like combustion.

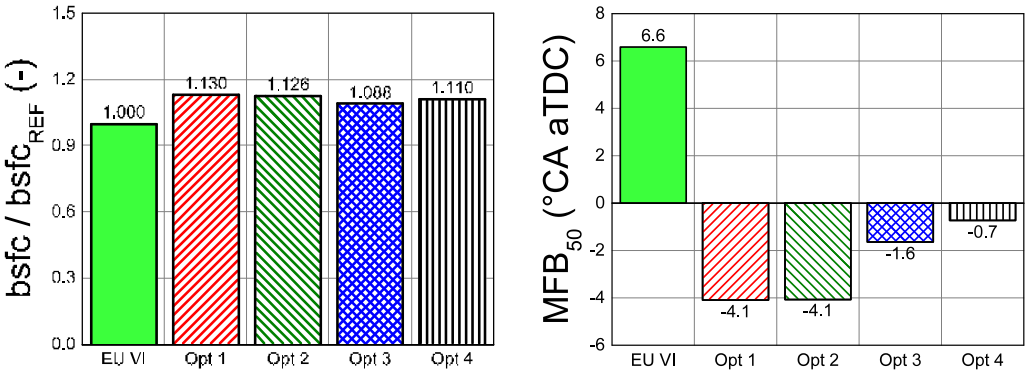

(a) (b)

Figure 3.11 - bsfc and MFB50: comparison between the base EU VI calibration and the optimized PCCI points.

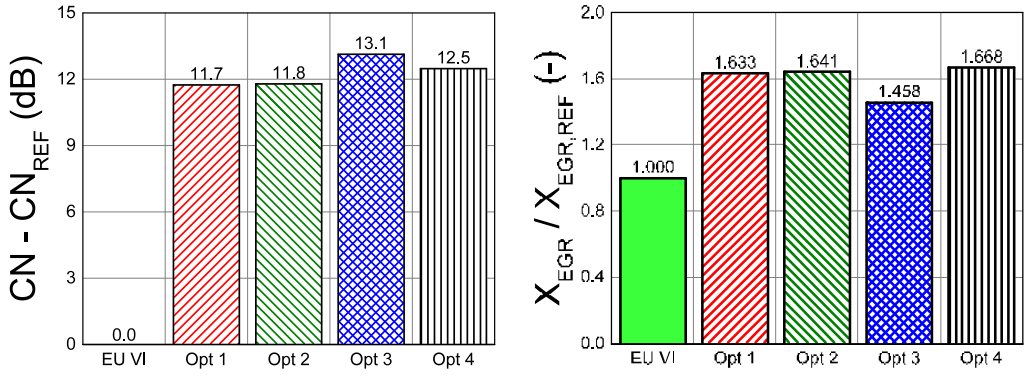

(a) (b)

Figure 3.12 - Combustion noise and EGR rate: comparison between the base EU VI calibration and the optimized PCCI points..

In all the tested conditions the combustion noise is considerably higher than in the reference condition, with an increase from 11.7 to 13.1 dB, which is in part due to the fact that the PCCI tests have been performed with a single injection strategy while the Euro VI calibration uses a triple injection strategy in the considered engine point. Moreover the advance in the combustion event and the longer ignition delay have to be accounted for as additional causes for the increase in combustion noise.

3.4 Application of combustion control techniques

3.4.1. Preface

The potentialities of LTC/PCCI combustion mode applied to the low speed – low load region on a diesel engine designed for a standard combustion mode have been discussed in the previous chapter by means of an optimization on steady-state tests performed according to design of experiments. The current version of the engine does not allow the operation in non-conventional combustion mode in a wide area of the map, while dedicated hardware modifications are going to be implemented in order to allow the calibration of PCCI combustion up to medium engine loads and on the whole engine speed range.

In this section, the effects of both model-based and pressure-based combustion controls are analyzed under steady-state and transient operations and compared to the standard map-based control. As a preliminary assessment of the developed techniques, most of the tests here presented refers to the application of the abovementioned models to traditional diesel combustion, while a set of steady-state tests also involved PCCI combustion mode operations. The robustness of the controls has been assessed in order to evaluate the effectiveness in different working conditions, such as considering different EGR rates and SOI, varying the fuel composition and disturbing the in-cylinder pressure signal during steady-state tests.

3.4.2 Pressure-based and model-based techniques for MFB50 control

The standard ECU calibration relies on a map-based approach, i.e. quantities are interpolated from look-up tables that mainly depend on the estimated fuel injected quantity (which is related to the engine load), the engine speed and other measured quantities, such as the intake air mass and the boost pressure. In particular, SOI maps depend on the total injected quantities and on the engine speed

as well as on the number of pilot injections. When transient operations are considered, the ECU applies several corrections to take into account of the delays in terms of injection pressure, boost pressure, EGR etc. Anyway, when SOI and ignition delay are no longer directly correlated, e.g in PCCI combustion mode, a new calibration of SOI would be necessary in order to achieve a correct MFB50 for all conditions, and transient operation corrections would become less effective. The calibration task would be much more time consuming and less robust compared to approaches that are able to control directly the MFB50, such as pressure-based and model-based controls.

The pressure-based control for the MFB50 stems from the measurement of the time-history of the in-cylinder pressure in the combustion chamber. The actual MFB50 value is obtained from the net energy release Q_{net}, which in turn is evaluated from the measured instantaneous in-cylinder pressure p and chamber volume V, on the basis of a single-zone approach, as follows:

$$dQ_{net} = \frac{\gamma}{\gamma - 1} pdV + \frac{1}{\gamma - 1} Vdp$$

where $\gamma = c_p/c_v = 1.37$. To have a short computational time a constant value of γ is chosen, even if, in a more refined calculation, γ would depend on the composition of the burned gas [71]. The integration of the dQ_{net} provides the net heat release profile Q_{net}, which is then normalized to its maximum value in order to get the mass fraction burned curve X_b and in particular to evaluate the MFB50, i.e. the crank angle at which the mass fraction burned is equal to 0.5. The evaluated cycle-by-cycle MFB50 is compared to the MFB50 target (i.e., $MFB50_{tgt}$) and the error between the target and the actual value is calculated. The SOI_{main} of the following cycle is then adjusted in order to minimize the MFB50 error, according to a closed-loop procedure described into details in [88]. In order to avoid instability problems of the controller, the entity of the correction on SOI_{main} is generally lower than the MFB50 error. As all the cylinders are instrumented with piezoelectric transducers, the MFB50 error calculation and the SOI correction can be performed not only cycle-by-cycle but also cylinder-by-cylinder.

The model-based control implements a procedure that evaluates a low-throughput predictive heat release curve based on a refined version of the accumulated fuel mass (AFM) approach [88]. As the MFB50 is not measured but estimated, the model is therefore of the open-loop type. The AFM approach

considers, at any time instant, that the rate of chemical energy released by the fuel is proportional to the energy associated with the in-cylinder accumulated fuel mass, i.e. the difference between the chemical energy of the injected fuel mass and the fuel released chemical energy. The model was assessed on steady-state tests evaluated on the considered engine (cf. the section experimental setup). In particular, a complete engine mapping (made up of 126 tests at different speeds and loads) and 12 EGR sweeps were considered. Therefore, the model is capable of predicting the effects of variations in engine speed, load and intake oxygen concentration on MFB50. The root mean square error (RMSE) between the predicted and the experimental MFB50 was around 0.8 °CA. The control is performed by means of the model inversion. The combustion predictive model is in fact able to simulate the heat release and the consequent MFB50 for a considered set of injection parameters and working conditions. The inverted model receives as an input the desired MFB50 target, and provides as output the corresponding SOI_{main} value that allows to obtain the desired target, adopting an iterative procedure with a fixed number of three iterations [88], capable of providing the desired SOI_{main} with an uncertainty lower than 0.2 °CA.

An overview of the three models is reported in Table 3.6.

Table 3.6 - Overview of the considered controls.

Control type	**Features**
Map-based	Standard ECU control based on SOI look-up tables.
Pressure-based	Closed-loop control on MFB50 evaluated cylinder-by-cylinder from the pressure signal.
Model-based	Open-loop control on MFB50 calculated from a predictive heat-release model.

Rapid Prototyping setup

The rapid prototyping (RP) setup is aimed at running new control strategies bypassing only the corresponding original ones present in the ECU, thus avoiding the need of completely reprogramming the ECU. For this purpose, an ETAS ES910 RP device has been used to implement the MFB50 controls. The control algorithms

were developed in Simulink and were deployed on the ETAS ES910 using the ETAS Intecrio software tool. In order to protect the engine, the functionalities of the new developed controls were initially tested in a Hardware-in-the-Loop configuration in which the RP device was connected to a real-time engine emulator running on a NI PXIe-8135 device [88]. In a following step, the RP device was directly connected to the engine ECU (see Fig. 3.2).

With reference to the setup for the pressure-based technique (Fig. 3.13a), a Kistler Kibox is used to calculate from the pressure signals acquired in all the cylinders the cycle-by-cycle real-time MFB50, using a single-zone model. The MFB50 values are sent in real-time to the RP device via CAN communication. The pressure-based control technique running on the RP device calculates the cycle-by-cycle SOI_{main} values needed to match the actual MFB50 for each cylinder to the target value. Then, it sends the updated SOI_{main} values to the engine ECU for each injector via ETK communication, thus bypassing the SOI_{main} values evaluated by the map-based control.

As far as the model-based technique setup (Fig. 3.13b) is concerned, the RP device receives the input signals needed for the low-throughput heat release model from the ECU via ETK. Then, the control algorithm calculates the SOI_{main} value, equal for all the cylinders, that allows the target MFB50 value to be reached, and sends this value to the ECU via ETK, thus bypassing the standard values derived from the ECU look-up tables.

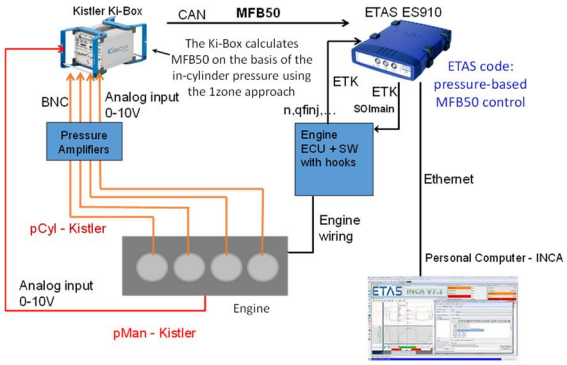

(a): RP setup for testing the pressure-based technique

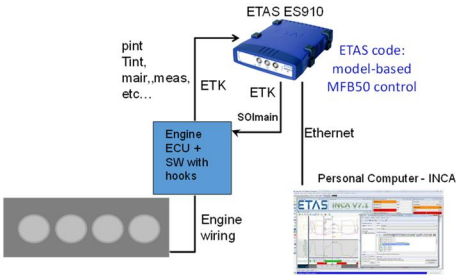

(b): RP setup for testing the model-based technique

Figure 3.13 - Scheme of the RP setup for the pressure-based (a) and model-based (b) MFB50 control techniques.

3.4.3 Results and discussion

The experimental activity on the FPT F1C 3.0L Euro VI diesel engine was performed under steady-state and transient conditions with the map-based control, the pressure-based and the model-based controls above described. The steady-state tests were relative to:

- Complete engine mapping with the three controls;
- SOI/MFB50 sweeps for three engine operating points with the map-based and the pressure-based control;
- EGR sweep up to reach unstable conditions under PCCI combustion mode for the map-based and the pressure-based control;
- Tests with different fuels, i.e. diesel, a 50%/50% blend diesel/JetA1 and a 100% JetA1 fuel;
- Tests with a disturbed pressure signal to simulate a degradation of the pressure signal or a pressure transducer of a lower quality;
- Tests with a reduced flow injector installed in one of the cylinders.

The transient tests were relative to fast load and speed ramps and to World Harmonized Transient Cycle (WHTC).

Engine mapping

The engine mapping tests were relative to about 85 engine points and were executed for each of the three controls at the following speeds: 850, 1000, 1200, 1400, 1600, 2000, 2500, 3000, 3500 rpm and the following loads: 7%, 12%, 25%, 37%, 50%, 62%, 75%, 87% and 100% of the maximum torque at each speed (Fig. 3.14).

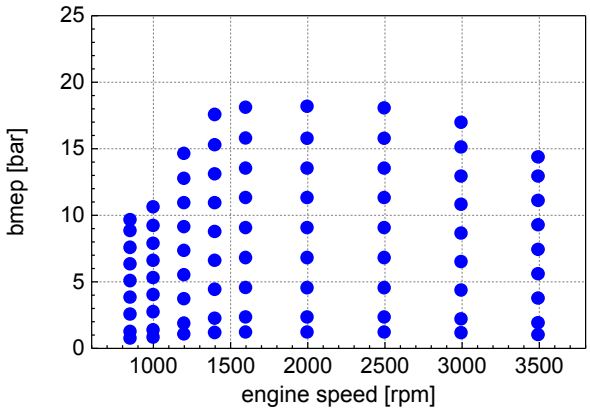

Figure 3.14 - Engine working points selected for engine mapping tests

The considered tests practically showed the same values in terms of bsfc and specific emissions (CO, HC, NO_x and soot) measured upstream of the after-treatment device and calculated from the emission analyzers. Therefore, pressure-based and model-based controls provided results aligned to the ones of the map-based calibration. In order to highlight the influence of the three controls on engine combustion stability, results pertaining to the coefficient of variation (CoV) of imep and PFP were analyzed. $CoV_{imep\ cyl}$ and $CoV_{PFP\ cyl}$ were evaluated cylinder-by-cylinder considering 100 consecutive cycles for each cylinder, while when referring to $CoV_{imep\ eng}$ and $CoV_{PFP\ eng}$, 400 pressure cycles, 100 cycles per cylinder, were evaluated. Therefore, $CoV_{imep\ cyl}$ and $CoV_{PFP\ cyl}$ take into account the cyclic variability, whereas $CoV_{imep\ eng}$ and $CoV_{PFP\ eng}$ can be thought as parameters that encompass both cycle-by-cycle and cylinder-by-cylinder variability. The highest values of CoV_{imep}, both considering each cylinder and the whole engine, are around 4% at the lowest loads whereas at high loads they become even lower than 1% considering the map-based control, thus showing a really stable cycle-by-cycle and

cylinder-by-cylinder behavior of the engine in all working conditions. The high cylinder-by-cylinder engine stability with the map-based strategy can be partially justified considering a very low dispersion of the EGR rate among the cylinders in most of the map, thanks to a proper design of the intake system specifically intended to reduce the EGR unbalance. As an example, Fig. 3.15 shows the EGR unbalance (evaluated according to [89]) relative to cylinder #1. This technique applies an enthalpy balance to the air and EGR flows which are mixing in the manifold:

$$\dot{m}_{EGR} c_{p,EGR} (T_{EGR} - T_{MAN}) = \dot{m}_{air} c_{p,air} (T_{MAN} - T_{air})$$

from which it is possible to obtain:

$$X_{EGR} = \frac{\dot{m}_{EGR}}{\dot{m}_{EGR} + \dot{m}_{air}} = \frac{(T_{MAN} - T_{air})}{(T_{MAN} - T_{air}) + \frac{(T_{EGR} - T_{MAN})}{c_{p,air}} c_{p,EGR}}$$

where T_{air} is the temperature of the air flow before mixing with EGR, T_{EGR} is the temperature of EGR before mixing with air and T_{MAN} is the temperature of the air-EGR mixture in the manifold. Applying to each single cylinder, i.e. considering the temperature in each runner or just upstream of the intake valves of each cylinder instead of the average manifold temperature, the EGR rate for each cylinder can be calculated.

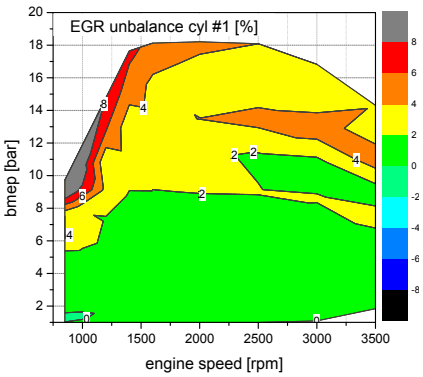

Figure 3.15 - EGR unbalance in the first cylinder with the map-based ECU strategy, evaluated as the difference between the cylinder-by-cylinder EGR rate and the average one, basing on the temperature of the intake air for each cylinder. Similar figures are obtained on the other cylinders

The $CoV_{imep\ cyl}$ and $CoV_{PFP\ cyl}$ showed similar values for the three controls. However, in the case of pressure-based control an appreciable decrease in the $CoV_{PFP\ eng}$ was generally found, especially at medium-high loads and speeds.

More in detail, Fig. 3.16a, b, c show the $CoV_{PFP\ eng}$ as a function of the engine load, comparing the three controls at three different engine speeds. For medium to high loads, it can be noted that the pressure-based control allows to achieve a reduction of the $CoV_{PFP\ eng}$ when compared to the other controls. As the cycle-by-cycle variability of PFP was verified to be low and very similar for all the controls, a reduction of $CoV_{PFP\ eng}$ can be mainly ascribed to a lower dispersion of PFP among cylinders. This is due to the fact that the pressure-based control sets the same MFB50 target for each cylinder, so that the angular position of PFP among cylinders results to be less scattered when compared to the other control methods. In other words, the pressure-based model can provide the potentiality to reduce cylinder-by-cylinder variations related to PFP by keeping the same MFB50 target for each cylinder. The effect of the implemented strategies on the cylinder-by-cylinder combustion timing can be observed with reference to Fig. 3.16d, which reports the difference between the maximum and the minimum MFB50 (averaged on 100 cycles) among the cylinders as a function of the brake mean effective pressure (bmep), comparing the map-based strategy to the pressure-based and to the model-based methods.

The graph reports the results obtained for various engine loads at 2000 rpm; similar trends are obtained for the other engine speeds. In particular, it can be noted that the combustion timing is not controlled at all when the map-based control and in the model-based are implemented, resulting in a maximum spread of 0.8 °CA between the cylinder which shows the most advanced combustion event and the one in which the combustion tends to be more retarded. On the other hand, the pressure-based method shows practically no cylinder-by-cylinder fluctuations, since the MFB50 is set to the same value for each cylinder. The dispersion of MFB50 between cylinders affects the dispersion of the angular position of PFP as well, thus increasing the afore-mentioned dispersion of $CoV_{PFP\ eng}$ among cylinders.

As a consequence of setting the same MFB50 target for each cylinder, the pressure-based control provided a slightly more uniform distribution of CN among cylinders, which is affected by the maximum value of the pressure derivative, and thus by the combustion timing. For instance, the cylinder that shows a more retarded MFB50 with respect to the other ones, will produce less noise since the combustion is shifted towards the expansion phase and the pressure derivative tends to decrease.

As an example, Fig. 3.17 shows the results relative to a speed section at 2000 rpm and different loads. However, the difference in terms of emissions was practically negligible, as can also be seen considering for example engine-out soot and NO_x emissions for the speed section at 2000 rpm, reported in Fig. 3.18. For confidentiality reasons emissions are reported in adimensional units, referring the values to the ones measured at bmep = 1 bar for the map-based control.

Similar results were found at different speed sections and load sections. The improved cylinder-by-cylinder uniformity is obtained although the EGR unbalance does not vary between the two controls (map-based and pressure-based): this shows that the cylinder-by-cylinder SOI correction applied through the pressure-based strategy allows a more precise control of the in-cylinder conditions regardless from other parameters which would normally affect the development of the combustion.

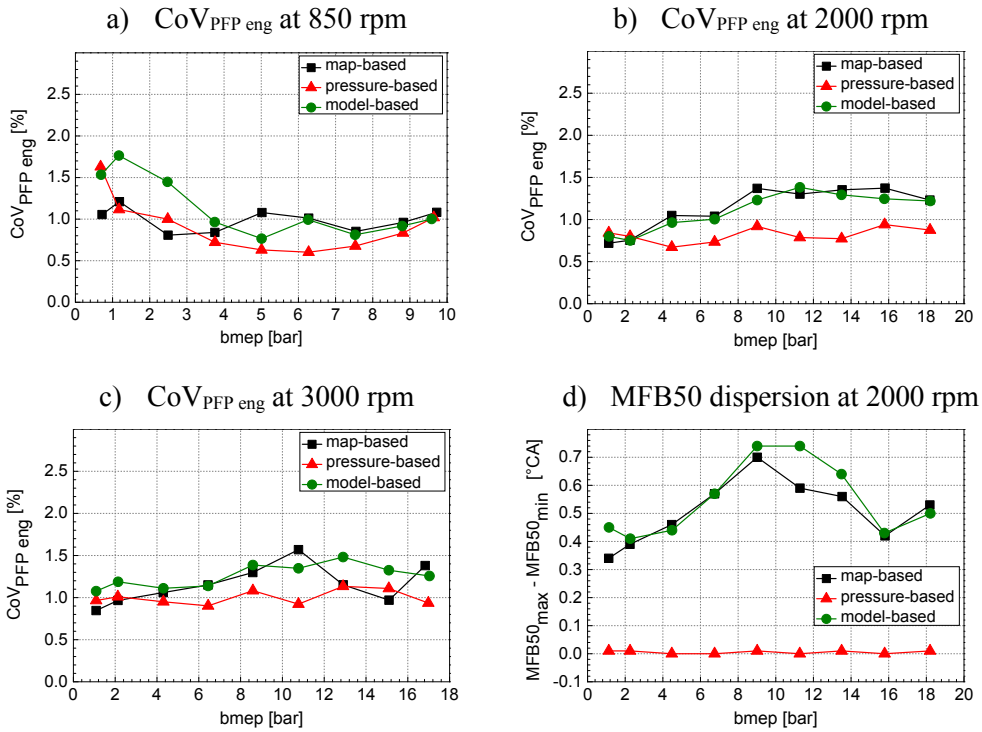

Figure 3.16 - Coefficient of variation of the peak firing pressure evaluated for the whole engine (a, b and c) and amplitude of the dispersion range of the MFB50 (d) on engine mapping tests: comparison among the map-based, the pressure-based and the model based controls. $CoV_{PFP\ eng}$ is shown on tests at various engine loads for three different engine speeds: a) 850 rpm; b) 2000 rpm; c) 3000 rpm. The dispersion of the MFB50 (d) is reported for 2000 rpm for various engine loads.

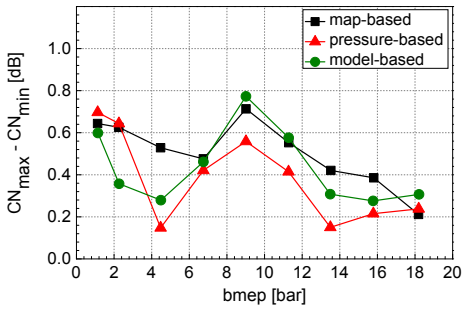

Figure 3.17 - Amplitude of the dispersion range of the combustion noise vs. engine load at 2000 rpm: comparison among the map-based strategy, the pressure-based control strategy and the model based one.

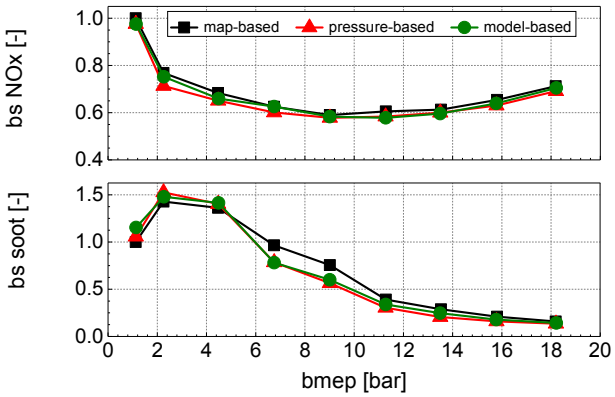

Figure 3.18 - Brake specific soot and NO_x emissions at 2000 rpm: comparison among the map-based strategy, the pressure-based control strategy and the model based one. The values are reported in adimensional units, referring all the values to the ones measured at bmep = 1 bar for the map-based control.

SOI/MFB50 sweeps

In the SOI/MFB50 sweep tests the map-based control and the pressure-based one were compared. At two different working points, namely 1400×4.4 (the number before the × symbol represents the engine speed in rpm whereas the other number is the bmep in bar), 3000 rpm at full load, a trade-off of SOI was considered for a single injection pattern (i.e. the pilot injections were disabled) for the map-based control and the corresponding values of MFB50, averaged on 100 cycles for each cylinder, were calculated. In the pressure-based control the average of the 4 values of MFB50 of the map-based control was set as a target for the pressure-based control.

The model-based method was not considered because the model was calibrated considering the base engine mapping at standard SOI and multiple injection pattern. A model-based control could be applied only after having acquired all the tests necessary for the calibration of the model in these working conditions.

As for mapping, similar results were obtained in terms of bsfc and emissions, as can be noted in Fig. 3.19, which reports engine-out soot and NO_x emissions in adimensional units, in which all the values are normalized according to the values measured at the reference SOI (the lowest value) for the map-based control. Also in these tests, a reduction in the $CoV_{PFP\ eng}$ was obtained by the pressure-based with respect to the map-based control, as shown in Fig. 3.20. On the other hand, similar dispersions in terms of CN were found applying the two controls, which cannot be compared to the results shown on the engine mapping since the former were performed with a triple-injection strategy while the latter presented a single injection.

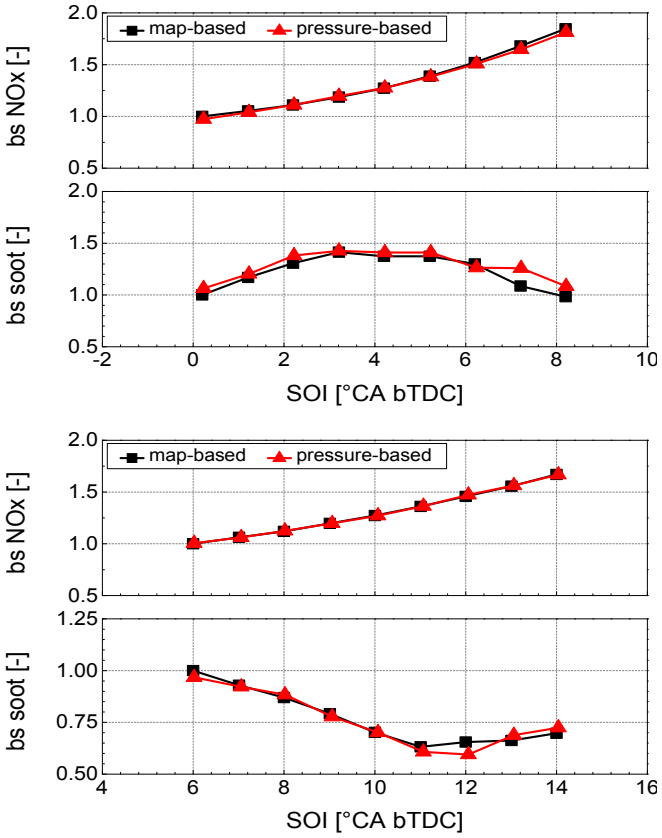

Figure 3.19 - Brake specific engine-out soot and NO_x emissions at 1400×4.4 and 3000 at full load (bottom): comparison between the map-based and the pressure-based control strategy.

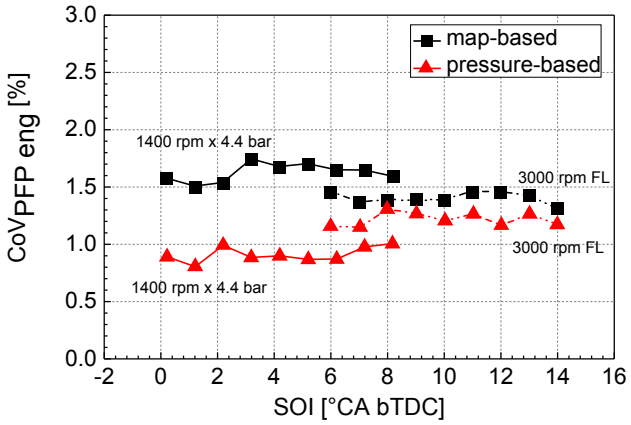

Figure 3.20 - Coefficient of variation of the peak firing pressure evaluated for the whole engine on SOI sweep tests for two engine points: comparison among the map-based strategy and the pressure-based control strategy.

EGR sweeps in PCCI combustion mode

Some PCCI tests were carried out as a preliminary test campaign, as the new release of the engine is designed to work under PCCI combustion mode. The comparison involved original control and pressure-based model. The tests were performed at 1600×2.2 with a high EGR (>60%) ratio and an advanced (in the compression stroke) single injection pattern in order to obtain a PCCI combustion regime. In order to achieve such high EGR rates, the EGR poppet valve was kept fully open and the flow rate of the recirculated exhaust gas was increased by raising the engine backpressure (i.e., the pressure difference across the EGR poppet valve) by means of the actuation of the already mentioned exhaust flap placed downstream of the turbine.

Tests were performed in the following way: in the original control, the SOI was fixed at 23 °CA bTDC, while in the pressure-based model MFB50 values were set to the average value from the different cylinders obtained during EGR sweep tests with map-based control. In both control modes, the EGR sweep was performed by progressively closing the exhaust flap, until combustion instability was reached.

Table 3.7 summarizes the conditions of the performed tests, where the SOI values in the case of the pressure-based method were obtained as a result of the strategy once set the target MFB50 (notice that a 100% exhaust flap position

corresponds to a totally closed flap). Due to the specific combustion mode implemented, soot and NO_x values were close to zero in every test condition, while similar values of bsfc, CO and HC were obtained for both controls, as it has been obtained in the previous tests.

A detailed analysis on the effects of the PCCI combustion mode on the engine-out emissions is not reported here since it is out of the scope of this section. A more detailed study has been carried out on this topic in Chapter 3.4. A similar approach will be applied on the new engine version designed for PCCI, aiming to exploit the benefits of this mode up to mid-high engine loads and high engine speed while reducing the drawbacks.

Table 3.7 - Test conditions for EGR sweeps in PCCI combustion mode.

Exhaust flap position	Map-based	Pressure-based				
	SOI (°CA bTDC)	target MFB50 (°CA	SOI (°CA bTDC)			
			Cyl #1	Cyl #2	Cyl #3	Cyl #4
94.5%	23	0.1	23.5	23.2	23.1	21.6
95.0%	23	1.8	23.7	23.2	23.1	21.2
95.2%	23	3.2	23.8	23.1	23.0	20.9
95.3%	23	4.3	23.6	22.8	22.7	20.5
95.4%	23	5.1	23.5	22.6	22.6	20.3
95.5%	23	6.6	23.9	22.7	22.6	20.3
95.5%	23	7.5	23.4	22.3	22.2	19.9
95.6%	unstable	7.5	27.4	25.1	25.1	22.3

$CoV_{imep\ eng}$ and $CoV_{PFP\ eng}$ were lower for pressure-based, with a lower CN dispersion among the cylinders. With reference to Fig. 3.21a and 3.21b, it can be observed that similar values are obtained with the two controls for the lower-end of the considered working range, while significant reductions are obtained for higher values of the flap position, i.e. in the conditions in which the combustion tends to be more unstable. As a consequence, pressure-based control also allowed to operate the engine with the flap in a more closed position, by maintaining the engine working point limit more stable. This allow to obtain a stable combustion even with large EGR rates in PCCI operation, which increases the chances of application of this combustion mode as a mean to reduce in-cylinder formation of NO_x e PM. Moreover, a significant reduction on the dispersion in the combustion noise CN is observed, as depicted in Fig. 3.21c: for each point the difference among the cylinder which shows the maximum CN and the one with the minimum CN is reported.

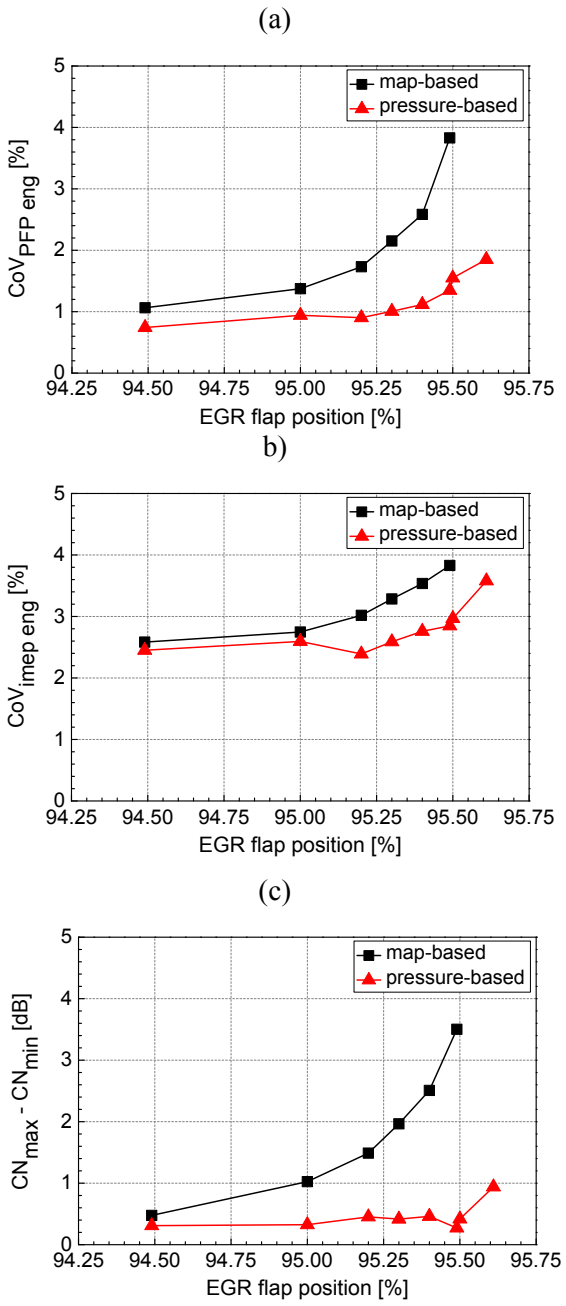

Figure 3.21 - Coefficient of variation of the peak firing pressure (a) and of the indicated mean effective pressure (b) evaluated for the whole engine, and amplitude of the dispersion range of the combustion noise (c) on EGR sweep tests in PCCI combustion mode: comparison among the map-based strategy and the pressure-based control strategy.

Disturbed pressure signal

A sinusoidal noise has been added to the pressure signals in order to replicate the behavior of a low-quality or aged in-cylinder pressure transducer and check whether the pressure-based model could still control properly the SOI_{main}. The resulting disturbed pressure signals were sent to the indicating device, namely Kistler Kibox, which calculates the MFB50. To compute the MFB50, the pressure signal is filtered out by means of a moving average filter, then the HRR curve is calculated and integrated to get the crank angle corresponding to the 50% of burned mass. In order to check the stability of the pressure-based control different sinusoidal disturbances, in particular 3 amplitudes – 0.7 bar, 1.4 bar, 2 bar – and 4 frequencies – 4 kHz, 5kHz, 6kHz, 7kHz, have been added to the pressure signal of every cylinder. Tests were performed for several working points setting the highest amplitude signal (i.e. 2 bar) within the selected range. Fig. 3.22 depicts the clean and disturbed signal for cylinder #1 and the corresponding fraction of burned mass. It was verified that the value of the resulting MFB50 is affected in a minor way by the disturbance, hence the pressure-based control preserves its stability even for this condition.

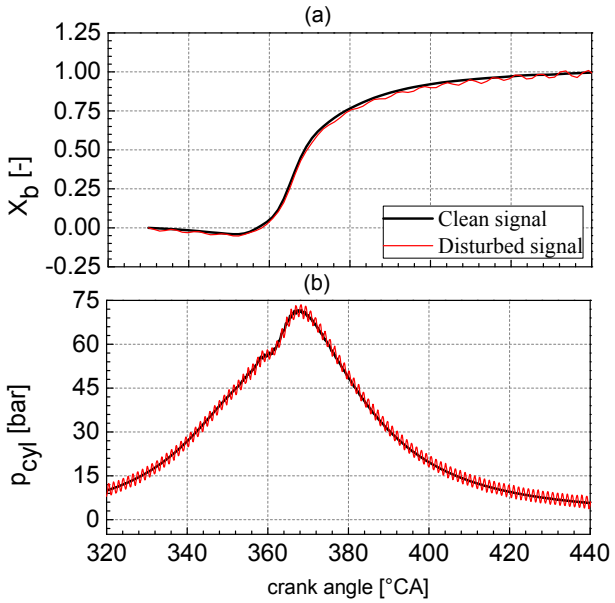

Figure 3.22 - Example of mass fraction burned X_b (a) and pressure trace (b) for cylinder #1 in the case of clean signal (black solid line) and disturbed one (red solid line). Engine working point 1400×4.4. Sinusoidal disturbance with amplitude = 2 bar and frequency = 7 kHz.

Jet fuel

Blends of Jet A1 and conventional diesel fuel (according to EN 590 regulations), whose main properties are listed in Table 3.8, have been fed to the engine to evaluate the robustness of controls. Engine mapping tests have been performed using 50%/50% blend diesel/JetA1 and a 100% JetA1 fuel implementing the three different controls. In addition a sweep of SOI/MFB50 was performed at 1400×4.4 comparing the map-based control with the pressure-based one. Although tests with different fuels did not provide appreciable differences among the controls in terms of performance and emissions, it has to be highlighted that the MFB50 is slightly influenced by the considered fuel, as depicted in Fig. 2.23 that reports the mean MFB50 versus SOI for the three considered fuels at the working point 2000×9.

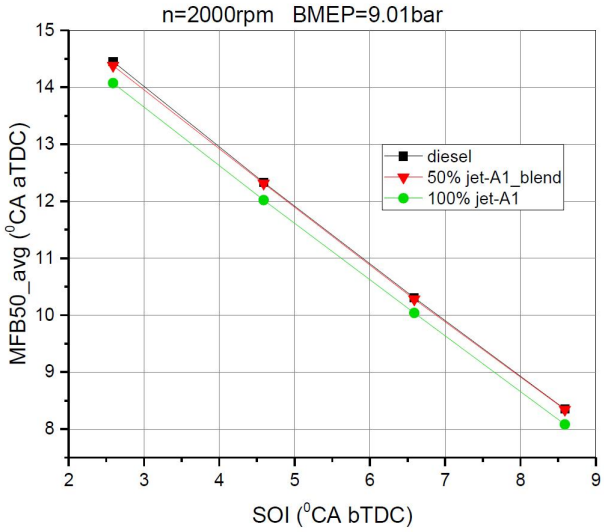

Figure 3.23 – Mean MFB50 versus SOI for the three tested fuels. Engine working point 2000×9.

The aim of these test was to check if the control methods were able to sustain a change in the fuel fed to the engine, since Jet A1 fuel has a lower price compared with diesel, so that it can be a cost-saving solution, especially for heavy-duty applications. The pressure-based control results still stable, proving its flexibility when different kinds of fuels are being fed to the engine. Therefore, considering that the differences among the tested fuels are appreciable (Table 3.8), the stability of the pressure-based control results of interest: injecting different fuels with a map-

based calibration may bring to a variation in the combustion process which may affect combustion stability and emissions. On the other hand, the pressure-based technique, by controlling the MFB50, allows to keep the same evolution of the combustion process whichever are the boundary conditions, e.g. the fuel properties/composition.

Table 3.8 - Main properties of Jet A1 and diesel EN590 fuels.

Property	Units	Jet A1	Diesel EN 590
Cetane number	-	-	53.1
Flash Point	°C	55	70
Density at 15 °C	kg/m^3	797	844
Viscosity at 40 °C	mm^2/s	1.241	2.860
Lower heating value	MJ/kg	43.3	43.4

Injector with reduced flow

A faulty injector (flow reduced by around 5%) has been mounted on cylinder #1 and a SOI sweep was performed at the two working points 1400×4.4 and 2000×9 with the map-based control and the pressure-based one. The aim of this tests was to replicate the behavior of a slight difference in terms of flow rate that can derive from ageing of the injector and consequently to test if the pressure-based control was still able to provide a good performance with respect to the map-based control. Unfortunately, no appreciable differences were found for with respect to the original injector, due to the similar nominal flow rates between the standard and the reduced flow injector. In other words, a difference of 5% on flow rate is not enough to highlight possible differences of performance between the two tested controls.

Transient Analysis

The transient analysis hereby proposed is based on the results obtained on engine load ramps at two different engine speed levels, namely 1400 rpm and 2000 rpm, and on WHTC (Fig. 3.24).

A preliminary analysis was performed to check the influence of speed, load and a combination of them on SOI_{main} and MFB50 and therefore the engine behavior on ramps of a progressively reduced time, i.e. 10, 5, 3 s. Since the MFB50 does not

vary significantly with the engine speed (Fig. 3.25), the influence of a speed variation was negligible on SOI_{main} variation. Therefore, in a successive step only fast load ramps were considered at two different speeds. The slope of the ramps were chosen to be comparable with a fast transient cycle as in WHTC.

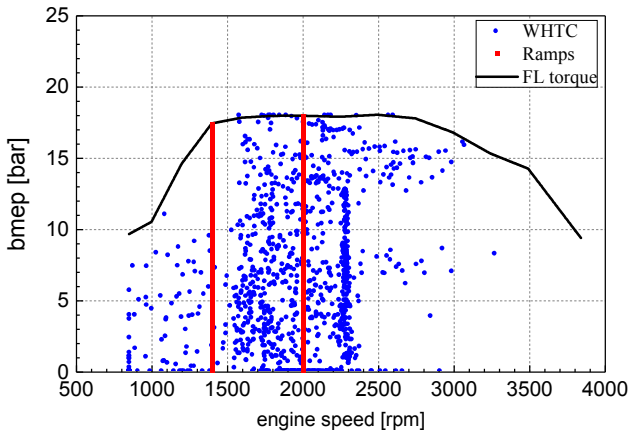

Figure 3.24 - WHTC (blue markers), load ramps (red markers) and full load curve (black solid line).

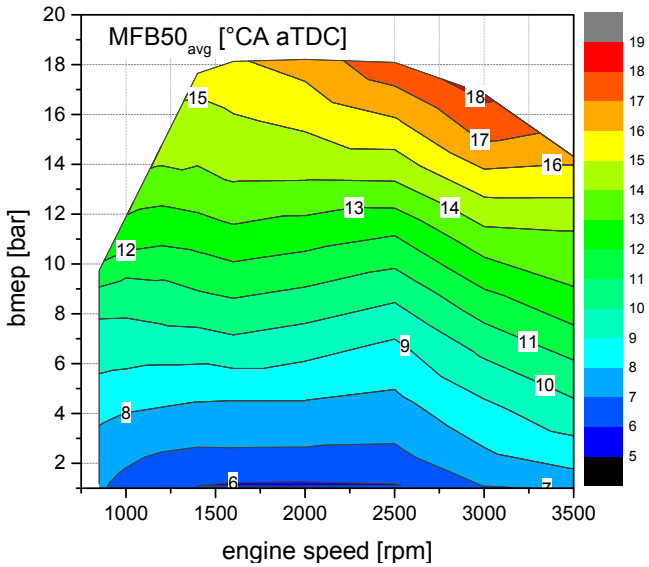

Figure 3.25 - Average MFB50 among cylinders as a function of engine speed and bmep on engine mapping tests.

As previously stated, the map-based calibration implemented in the ECU sets SOI_{main} through look-up tables according to engine speed and load, expressed as injected fuel per cycle. Afterwards, if a load-increasing transient maneuver is detected, a correction on SOI_{main} is applied taking into account the actual p_{rail} and boost pressure in order to avoid huge increase of smoke and excessive in-cylinder pressure. Considering the performed transient tests, this correction also produces a significant reduction of NO_x. In order to perform a coherent comparison between map-based control and the new ones here proposed, based on MFB50, the transient correction of the original calibration was bypassed, because at the current development status the pressure-based and model-based controls do not perform a dynamic correction based on other engine variables (e.g. p_{rail} and boost pressure). Therefore, when talking about the map-based calibration in this section it is meant the calibration without the transient correction, bypassed by setting the SOI_{main} referring to the steady-state map by means of the RP device.

A portion of the performed ramps is depicted in Fig. 3.27 in which the SOI_{main} and MFB50 are reported for the map-based control (Fig. 3.27b) the pressure-based control (Fig. 3.27c) and the model-based control (Fig. 3.27d). In all the graphs of Fig. 3.27, the orange thick line represents the MFB50 target relative to the pressure-based control, whereas the thin colored lines close to it represent the actual MFB50 values for the different cylinders. The SOI_{main} indicated with the thick red line in all the graphs represents the SOI of the main injection evaluated interpolating the steady-state map. For the map-based control (Fig. 3.27b), this corresponds to the SOI_{main} actuated in all the cylinders, while when the pressure-based control (Fig. 3.27c) is applied, the actual cylinder-by-cylinder SOI_{main} varies with respect to the map-based one (as indicated by the different colored lines close to the thick red one) in order to match the MFB50 target. In the model-based control (Fig. 3.27d) the SOI_{main}, reported with a green thin line, is calculated by means of the implemented strategy based on the estimated MFB50. It can be observed that the pressure-based model allows to limit the dispersion of the cylinder-by-cylinder MFB50 with respect to the target one, although – differently from what highlighted by steady-state tests – the target is not perfectly matched due to the highly dynamic nature of the transient operation. To further highlight this effect, Fig. 3.26 shows the amplitude of the cylinder-by-cylinder variation of the MFB50 in transient operation: with pressure-based control, the dispersion is less spread around a lower mean value compared to the map-based control. Still concerning the MFB50, the model-based control showed a similar cylinder-by-cylinder variation bandwidth as in the map-based control due to the absence of a cylinder-by-cylinder SOI_{main}

control. Moreover, it shows an undershoot behavior of the set SOI_{main} at the beginning of the load ramp and an overshoot after it (Fig. 3.27d) possibly due uncertainties in the real-time estimation of the intake O_2 necessary for the control [88] during high transient operation.

The values of fuel consumption are virtually unaffected by the considered control. Possible variations in terms of HC were difficult to be estimated as the integral value obtained at the end of the transient test was quite low (around 0.5 g upstream of the after-treatment device at the end of WHTC). Values of CO showed a certain dispersion among different repetitions, however pressure-based and model-based controls showed lower values up to 6% with respect to the map-based control. As far as NO_x are concerned, the model-based control generally showed an improvement around 1.5% with respect to the map-based one, whereas a no definite trend was always found for the model-based control. These results are obtained as average on the cumulated emissions along 5 repetitions of the considered maneuver. The reasons for a decrease in NO_x can be ascribed to possible EGR delay difference between transient and steady-state conditions, especially when a decreasing load ramp is considered, and dispersion among the cylinder not accounted for by the map-based calibration.

In general, this confirms that the proposed controls are always comparable to the standard map-based one in terms of fuel consumption and emissions, without any detrimental effect on the conventional combustion. Moreover in some cases some minor positive effects have been shown. This encourages the research in this field toward the application of this methodology to transient operation in PCCI combustion mode, where larger benefits are expected due to the significant improvements achievable on combustion stability. Furthermore, the pressure-based control technique allows to reduce the time needed for engine calibration and improves the combustion quality with engine ageing thanks to its ability to auto-compensate for any time drift or for other random or systematic variations in the boundary conditions with respect to reference ones, and therefore is considered of interest also for conventional combustion modes.

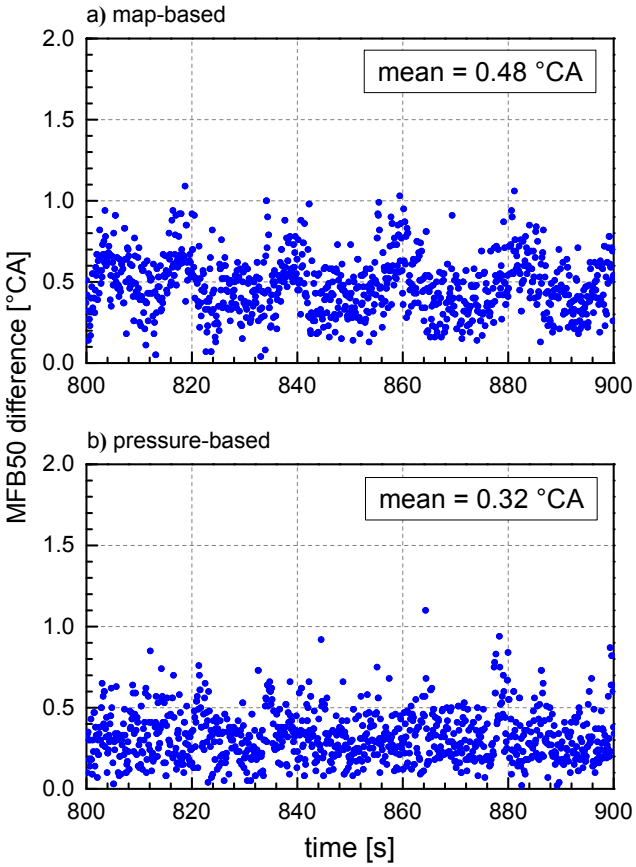

Figure 3.26 - Amplitude of the variation range of the MFB50 and related mean MFB50 variations during transient operations: comparison between the map-based (a, without SOI correction) and the pressure-based (b) controls.

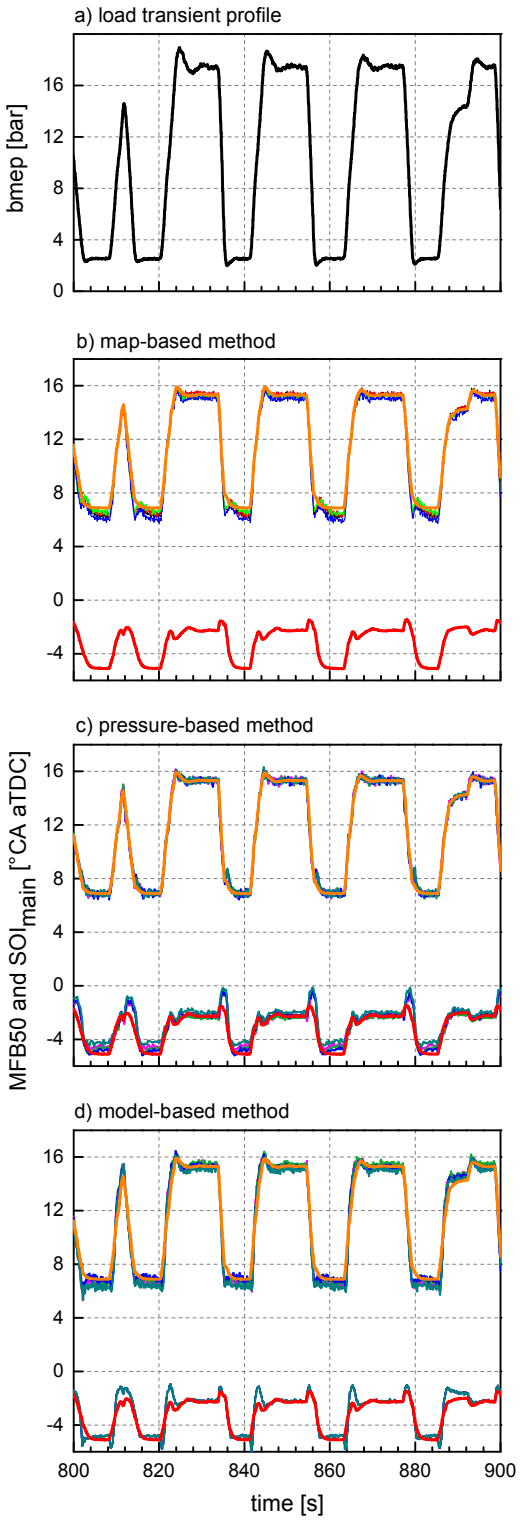

Figure 3.27 - Transient analysis: part of the reference load variation profile at 1400 rpm (a) and related MFB50 and SOImain values: comparison among the map-based (b, without SOI correction), the pressure-based (c) and the model-based (d) controls.

3.5 Final remarks

In the first part of this chapter the potentialities to simultaneously reducing Soot and NO_x emissions in diesel engine with a PCCI combustion mode have been presented for a low load working point, namely at engine speed equal to 1800 rpm and load to 1 bar . The main outcomes for the considered working point, but that can be extended to other low load points, are summarized as follows:

- PCCI combustion is obtained with a proper combination of high EGR levels and advanced combustion. A lower SOI than 16 °CA bTDC is not able to let the engine enter the PCCI combustion mode independently of the EGR level;

- It was possible to simultaneously reduce engine out NO_x and soot of 90% and 99%, respectively, of the base point values.

- Reduction in NOx and Soot are always related to important increase in HC and CO due to advanced injection in a colder and low density environment. Also bsfc and CN showed a negative increase.

- A proper calibration can be obtain through DoE to find the best trade-off among all the considered output values.

In addition to this, DoE proved to effectively support the effort of the experimenter in optimizing the engine calibration.

A further improvement of the obtained results and a simultaneous minimization of the corresponding drawbacks can be obtained considering a proper design and replacement of the standard conventional hardware with one a dedicated to PCCI combustion.

The second part showed the experimental results relative to the application of a pressure-based and a model-based real-time combustion control technique for the evaluation and the control of the MFB50. These two control approaches were compared to the conventional map-based control of the standard ECU through a set of tests carried out on a FPT F1C 3.0 L Euro VI diesel engine.

All the experimental results highlighted that the performance of the engine featuring the two combustion controls, in terms of exhaust pollutant emissions and brake specific fuel consumption, were aligned to that of the conventional map-based calibration. The main advantage in the adoption of the pressure-based and model-based techniques is the possibility to set an optimal MFB50 target map,

which would allow to control the quality of the combustion whatever surrounding conditions: EGR unbalance, fuel characteristics, injector characteristics and combustion mode (provided that a dedicated optimal MFB50 target map is developed in the latter case).

In particular, the following main results were obtained:

- For tests under steady-state conditions, the CoV_{imep} and CoV_{PFP} of each cylinder showed similar values for the three controls. However, in the case of pressure-based control an appreciable decrease in the CoV_{PFP} evaluated on the whole engine was generally found, especially at medium-high loads and speeds, in the range of 0.2 to 0.7 %. This is due to a lower dispersion of PFP among cylinders, which provided a slightly more uniform distribution of CN.

- Tests performed under PCCI combustion regime at 1600×4.4 with a high EGR rate (>60%) and advanced single injection pattern showed the best potentialities of MFB50 control methodologies to improve combustion stability reducing COV_{imep} and CoV_{PFP}, thus further extending the tolerable EGR rate.

- The pressure-based control proved to be very robust to disturbances added on purpose to the pressure signal to replicate the behavior of a low-quality or aged in-cylinder pressure transducer: the influence on the estimated MFB50 was negligible.

- Considering blends of Jet A1 and conventional diesel fuel, the pressure-based control resulted still stable, proving its flexibility when different kinds of fuels are being fed to the engine.

- In transient analysis, the pressure-based model allowed to limit the dispersion of the cylinder-by-cylinder MFB50 with respect to the target one compared to the map-based control. The model-based control showed a similar cylinder-by-cylinder variation bandwidth of MFB50 as in the map-based control due to the absence of a cylinder-by-cylinder SOI_{main} control. The values of fuel consumption were virtually unaffected by the considered control. Values of CO showed a certain dispersion among different repetitions, however pressure-based and model-based controls showed lower values up to 6% with respect to the map-based control. As regard NO_x, the model-based control generally showed an improvement around 1.5% with respect to the map-based one, whereas a no definite trend was found for the model-based control.

The pressure-based control could provide further improvements in terms of engine stability implementing an algorithm to correct the injected quantity of the main to reach a desired value of imep equal for all the cylinders.

The results here reported are pertaining to a preliminary experimental analysis on a standard diesel engine running in conventional and PCCI combustion mode. As the best potentialities of the proposed controls are related to PCCI combustion, the upcoming activity will be performed on a diesel engine purposely designed for this non-conventional combustion mode.

References

[1] IEA, 2016. “World energy outlook 2016”, IEA Publications.

[2] Vancoillie J., Demuynck J., Sileghem L., Van De Ginste M., Verhelst S., 2012, “Comparison of the renewable transportation fuels, hydrogen and methanol formed from hydrogen, with gasoline – Engine efficiency study”, International Journal of Hydrogen Energy, Volume 37, Issue 12, Pages 9914-9924, ISSN 0360-3199, https://doi.org/10.1016/j.ijhydene.2012.03.145

[3] Villante C., Genovese A., 2012, “Hydromethane: A bridge towards the hydrogen economy or an unsustainable promise?”, International Journal of Hydrogen Energy, Volume 37, Issue 15, Pages 11541-11548, ISSN 0360-3199, https://doi.org/10.1016/j.ijhydene.2012.03.066

[4] Akansu S.O., Dulger Z., Kahraman N., Veziroğlu, T.N., 2004, “Internal combustion engines fueled by natural gas—hydrogen mixtures”, International Journal of Hydrogen Energy, Volume 29, Issue 14, Pages 1527-1539, ISSN 0360-3199, https://doi.org/10.1016/j.ijhydene.2004.01.018

[5] Klell M., Eichlseder H., Sartory M., 2012, “Mixtures of hydrogen and methane in the internal combustion engine – Synergies, potential and regulations”, International Journal of Hydrogen Energy, Volume 37, Issue 15, Pages 11531-11540, ISSN 0360-3199, https://doi.org/10.1016/j.ijhydene.2012.03.067

[6] Verhelst S., 2014, “Recent progress in the use of hydrogen as a fuel for internal combustion engines”, International Journal of Hydrogen Energy, Volume 39, Issue 2, Pages 1071-1085, ISSN 0360-3199, https://doi.org/10.1016/j.ijhydene.2013.10.102

[7] Salvi B.L., Subramanian K.A., 2015, “Sustainable development of road transportation sector using hydrogen energy system”, Renewable and Sustainable

Energy Reviews, Volume 51, Pages 1132-1155, ISSN 1364-0321, https://doi.org/10.1016/j.rser.2015.07.030

[8] Patrizio P., Chinese D., 2016, "The impact of regional factors and new bio-methane incentive schemes on the structure, profitability and CO2 balance of biogas plants in Italy", Renewable Energy, Volume 99, Pages 573-583, ISSN 0960-1481, https://doi.org/10.1016/j.renene.2016.07.047

[9] Torrijos M., 2016, "State of Development of Biogas Production in Europe", Procedia Environmental Sciences, Volume 35, Pages 881-889, ISSN 1878-0296 https://doi.org/10.1016/j.proenv.2016.07.043.

[10] Zhang K., 2012, "Target versus price: improving energy efficiency of industrial enterprises in China", Doctoral dissertation, The Pennsylvania State University.

[11] Zhang W., 2010, "Automotive fuels from biomass via gasification", Fuel Processing Technology. Volume 91, Issue 8, Pages 866-876, ISSN 0378-3820, https://doi.org/10.1016/j.fuproc.2009.07.010

[12] Baratta M., d'Ambrosio S., Misul D., Spessa E., 2014, "Effects of H2 Addition to CNG Blends on Cycle-To-Cycle and Cylinder-to-Cylinder Combustion Variation in an SI Engine", J. Eng. Gas Turbines Power 136(5), 051502 doi:10.1115/ICES2012-81187.

[13] Ma F., Wang M., Jiang L., Deng J., Chen R., Naeve N., Zhao S., 2010, "Performance and emission characteristics of a turbocharged spark-ignition hydrogen-enriched compressed natural gas engine under wide open throttle operating conditions", International Journal of Hydrogen Energy, Volume 35, Issue 22, Pages 12502-12509, ISSN 0360-3199, https://doi.org/10.1016/j.ijhydene.2010.08.053

[14] Baratta M., d'Ambrosio S., Misul D., 2013, "Performance and Emissions of a Turbocharged Spark Ignition Engine Fuelled with CNG and CNG/Hydrogen Blends", SAE Paper 2013-01-0866, https://doi.org/10.4271/2013-01-0866.

[15] Bysveen M., 2007, “Engine characteristics of emissions and performance using mixtures of natural gas and hydrogen”, Energy, Volume 32, Issue 4, Pages 482-489, ISSN 0360-5442, https://doi.org/10.1016/j.energy.2006.07.032

[16] Kahraman N., Çeper B., Akansu S.O., Aydin K., 2009, “Investigation of combustion characteristics and emissions in a spark-ignition engine fuelled with natural gas-hydrogen blends”, International Journal of Hydrogen Energy, Volume 34, Issue 2, Pages 1026-1034, ISSN 0360-3199, https://doi.org/10.1016/j.ijhydene.2008.10.075

[17] Hora T.S., Agarwal A.K., 2015, “Experimental study of the composition of hydrogen enriched compressed natural gas on engine performance, combustion and emission characteristics”, Fuel, Volume 160, Pages 470-478, ISSN 0016-2361, https://doi.org/10.1016/j.fuel.2015.07.078

[18] Akansu S.O., Kahraman N., Çeper B., 2007, “Experimental study on a spark ignition engine fuelled by methane-hydrogen mixtures”, International Journal of Hydrogen Energy, Volume 32, Issue 17, Pages 4279-4284, ISSN 0360-3199, https://doi.org/10.1016/j.ijhydene.2007.05.034

[19] Açıkgöz B., Çelik C., Soyhan H.S., Gökalp B., Karabağ B., 2015, “Emission characteristics of an hydrogen-CH4 fuelled spark ignition engine”, Fuel, Volume 159, Pages 298-307, ISSN 0016-2361, https://doi.org/10.1016/j.fuel.2015.06.043

[20] Lounici M.S., Boussadi A., Loubar K., Tazerout M., 2014, “Experimental investigation on NG dual fuel engine improvement by hydrogen enrichment”, International Journal of Hydrogen Energy, Volume 39, Issue 36, Pages 21297-21306, ISSN 0360-3199, https://doi.org/10.1016/j.ijhydene.2014.10.068

[21] Thurnheer T., Soltic P., Dimopoulos Eggenschwiler P., 2009, “S.I. engine fuelled with gasoline, methane and methane/hydrogen blends: Heat release and loss analysis”, International Journal of Hydrogen Energy, Volume 34, Issue 5, Pages 2494-2503, ISSN 0360-3199, https://doi.org/10.1016/j.ijhydene.2008.12.048

[22] Gersen S., van Essen M., van Dijk G., Levinsky H., 2014, “Physicochemical effects of varying fuel composition on knock characteristics of natural gas mixtures”, Combustion and Flame, Volume 161, Issue 10, Pages 2729-2737, ISSN 0010-2180, https://doi.org/10.1016/j.combustflame.2014.03.019

[23] Bauer C.G., Forest T.W., 2001, “Effect of hydrogen addition on the performance of methane-fueled vehicles. Part I: effect on S.I. engine performance”, International Journal of Hydrogen Energy, Volume 26, Issue 1, Pages 55-70, ISSN 0360-3199, https://doi.org/10.1016/S0360-3199(00)00067-7

[24] Mathai R., Malhotra R.K., Subramanian K.A., Das L.M., 2012, “Comparative evaluation of performance, emission, lubricant and deposit characteristics of spark ignition engine fueled with CNG and 18% hydrogen-CNG”, International Journal of Hydrogen Energy, Volume 37, Issue 8, Pages 6893-6900, ISSN 0360-3199, https://doi.org/10.1016/j.ijhydene.2012.01.083

[25] Porpatham E., Ramesh A., Nagalingam B., 2008, “Investigation on the effect of concentration of methane in biogas when used as a fuel for a spark ignition engine”, Fuel, Volume 87, Issues 8-9, Pages 1651-1659, ISSN 0016-2361, https://doi.org/10.1016/j.fuel.2007.08.014

[26] Park C., Park S., Lee Y., Kim C., Lee S., Moriyoshi Y., 2011, “Performance and emission characteristics of a SI engine fueled by low calorific biogas blended with hydrogen”, International Journal of Hydrogen Energy, Volume 36, Issue 16, Pages 10080-10088, ISSN 0360-3199, https://doi.org/10.1016/j.ijhydene.2011.05.018

[27] Chandra R., Vijay V.K., Subbarao P.M.V., Khura T.K., 2011, “Performance evaluation of a constant speed IC engine on CNG, methane enriched biogas and biogas”, Applied Energy, Volume 88, Issue 11, Pages 3969-3977, ISSN 0306-2619, https://doi.org/10.1016/j.apenergy.2011.04.032

[28] Yue J., 2016, “Effect of hydrogen addition on performance of low heat value gas engine”, International Journal of Hydrogen Energy, ISSN 0360-3199, https://doi.org/10.1016/j.ijhydene.2016.03.172

[29] Arroyo J., Moreno F., Muñoz M., Monné C., Bernal N., 2014, "Combustion behavior of a spark ignition engine fueled with synthetic gases derived from biogas", Fuel, Volume 117, Part A, Pages 50-58, ISSN 0016-2361, https://doi.org/10.1016/j.fuel.2013.09.055

[30] Subramanian K.A., Mathad V.C., Vijay V.K., Subbarao P.M.V., 2013, "Comparative evaluation of emission and fuel economy of an automotive spark ignition vehicle fuelled with methane enriched biogas and CNG using chassis dynamometer", Applied Energy, Volume 105, Pages 17-29, ISSN 0306-2619, https://doi.org/10.1016/j.apenergy.2012.12.011

[31] Arroyo J., Moreno F., Muñoz M., Monné C., 2013, "Efficiency and emissions of a spark ignition engine fueled with synthetic gases obtained from catalytic decomposition of biogas", International Journal of Hydrogen Energy, Volume 38, Issue 9, Pages 3784-3792, ISSN 0360-3199, https://doi.org/10.1016/j.ijhydene.2013.01.087

[32] Lattieff F.A., 2016, "A study of biogas production from date palm fruit wastes", Journal of Cleaner Production, Volume 139, Pages 1191-1195, ISSN 0959-6526, https://doi.org/10.1016/j.jclepro.2016.08.139

[33] Chen C., Guo W., Ngo H.H., Lee D.J., Tung K.L., Jin P., Wang J., Wu Y., 2016, "Challenges in biogas production from anaerobic membrane bioreactors", Renewable Energy, Volume 98, Pages 120-134, ISSN 0960-1481, https://doi.org/10.1016/j.renene.2016.03.095

[34] Brudecki G., Farzanah R., Cybulska I., Schmidt J.E., Thomsen M.H., 2015, "Evaluation of Composition and Biogas Production Potential from Seagrass (Halodule uninervis) Native to Abu Dhabi", Energy Procedia, Volume 75, Pages 760-766, ISSN 1876-6102, https://doi.org/10.1016/j.egypro.2015.07.508

[35] Elreedy A., Tawfik A., Enitan A., Kumari S., Bux F., 2016, "Pathways of 3-biofules (hydrogen, ethanol and methane) production from petrochemical industry wastewater via anaerobic packed bed baffled reactor inoculated with mixed culture bacteria", Energy Conversion and Management, Volume 122, Pages 119-130, ISSN 0196-8904, http://hdl.handle.net/10321/2375

[36] Baratta M., d'Ambrosio S., Iemmolo D., Misul D., 2015, "Influence of different compositions of natural gas on engine performance", ASME-ATI-UIT 2015 Conference on Thermal Energy Systems: Production, Storage, Utilization and the Environment Napoli (Italy) ISBN:978-88-98273-17-1.

[37] Mirheidari S., Franchek M., Grigoriadis K., Mohammadpour J., Wang Y.Y., Haskara I., 2012, "Real-time and robust estimation of biodiesel blends", Fuel, Volume 92, Issue 1, Pages 37-48, ISSN 0016-2361, https://doi.org/10.1016/j.fuel.2011.06.060

[38] Snyder D.B., Adi G.H., Bunce M.P., Satkoski C.A., Shaver G.M., 2010, "Fuel blend fraction estimation for fuel-flexible combustion control: Uncertainty analysis", Control Engineering Practice, Volume 18, Issue 4, Pages 418-432, ISSN 0967-0661, https://doi.org/10.1016/j.conengprac.2010.01.001

[39] Milanese M., Bonansone M., 2015, "Estimation of the Composition of Methane-Hydrogen Mixtures from Engine Control Variables", SAE Technical Paper 2015-24-2493, doi:10.4271/2015-24-2493, https://doi.org/10.4271/2015-24-2493

[40] Baratta M., d'Ambrosio S., Iemmolo D., Misul D., 2017, "Method for the recognition of the fuel composition in CNG engines fed with natural gas/biofuel/hydrogen blend", Journal of Natural Gas Science and Engineering, Volume 40, Pages 312-326, ISSN 1875-5100, https://doi.org/10.1016/j.jngse.2017.01.027

[41] Catania A., Misul D., Spessa E., Martorana G., 2000, "Conversion of a Multivalve Gasoline Engine to Run on CNG", SAE Technical Paper 2000-01-0673, https://doi.org/10.4271/2000-01-0673

[42] Catania A., d'Ambrosio S., Mittica A., Spessa E., 2001, "Experimental Investigation of Fuel Consumption and Exhaust Emissions of a 16V Pent-Roof Engine Fueled by Gasoline and CNG", SAE Technical Paper 2001-01-1191, https://doi.org/10.4271/2001-01-1191

[43] Ebner H., Köck K., 2000, "New Fuel Mass Flow Meter - A Modern and Reliable Approach to Continuous and Accurate Fuel Consumption Measurement" SAE Technical Paper 2000-01-1330, https://doi.org/10.4271/2000-01-1330

[44] Larsen J.F., Wallace J.S., 1997, "Comparison of Emissions and Efficiency of a Turbocharged Lean-Burn Natural Gas and Hythane-Fueled Engine", ASME Transactions, Journal of Eng. For Gas Turbines and Power, Vol. 119, pp.218-226, doi:10.1115/1.2815553

[45] Hoekstra R. L.; Blarigan P. V.; Mulligan N., 1996, "Nox Emissions and Efficiency of Hydrogen, Natural Gas and Hydrogen/Natural Gas Blended Fuels", SAE Technical Paper 961103, https://doi.org/10.4271/961103

[46] Ma F., Wang Y., Liu H., Li Y., Wang J., Zhao S., 2007 "Experimental study on thermal efficiency and emission characteristics of lean burn natural gas engine", Int. Journal of Hydrogen Energy, vol. 32, pp.5067-5075, https://doi.org/10.1016/j.ijhydene.2007.07.048

[47] Heywood J.B., 1988, "Internal Combustion Engine Fundamentals" McGraw-Hill International Editions.

[48] Serrano J.R., Guardiola C., Dolz V., Tiseira A., Cervellò C., 2007, "Experimental Study of the Turbine Inlet Gas Temperature Influence on Turbocharger Performance", SAE Paper 2007-01-1559, https://doi.org/10.4271/2007-01-1559

[49] Misul D., Baratta M., Kheshtinejad H., 2014, "Fluid-Dynamic Modeling and Advanced Control Strategies for a Gaseous-Fuel Injection System", SAE Technical Paper 2014-01-1096, https://doi.org/10.4271/2014-01-1096.

[50] White F. M., 2010, "Fluid Mechanics", McGraw-Hill Series in Mechanical Engineering, 7th Edition.

[51] Zhu H., Bohac S., Nakashima K., et al., 2013, "Effect of fuel oxygen on the trade-offs between soot, NOx and combustion efficiency in premixed low-

temperature diesel engine combustion", Fuel, 2013, n. 112, pp. 459-465, https://doi.org/10.1016/j.fuel.2013.05.023

[52] James E., Parks, Prikhodko V., Storey J., Barone T., Lewis S., Kass M, Huff S., 2010, "Emissions from premixed charge compression ignition (PCCI) combustion and effect on emission control devices", Catalysis Today, Volume 151, pp. 278-284, https://doi.org/10.1016/j.cattod.2010.02.053

[53] Wahlin, F., 2007, "Experimental Investigation of Impinging Diesel Sprays for HCCI Combustion", Doctoral thesis, Department of Machine Design, Royal Institute of Technology, Stockholm, Sweden.

[54] Musculus M., Miles P., Pickett L., 2013, "Conceptual models for partially premixed low-temperature diesel combustion", Progress in Energy and Combustion Science, n. 39, pp. 246-283, https://doi.org/10.1016/j.pecs.2012.09.001

[55] Iwabuchi Y., Kawai K., Shoji T., Takeda Y., 1999, "Trial of New Concept Diesel Combustion System - Premixed Compression-Ignited Combustion", SAE Technical Paper 1999-01-0185, https://doi.org/10.4271/1999-01-0185

[56] Hashizume T., Miyamoto T., Hisashi A., Tsujimura K., 1998, "Combustion and Emission Characteristics of Multiple Stage Diesel Combustion", SAE Technical Paper 980505, https://doi.org/10.4271/980505

[57] Hasegawa R., Yanagihara H., 2003, "HCCI Combustion in DI Diesel Engine", SAE Technical Paper 2003-01-0745, https://doi.org/10.4271/2003-01-0745

[58] Reveille B., Kleemann A., Knop V., and Habchi C., 2006, "Potential of Narrow Angle Direct Injection Diesel Engines for Clean Combustion: 3D CFD Analysis", SAE Technical Paper 2006-01-1365, https://doi.org/10.4271/2006-01-1365.

[59] Kimura S., Aoki O., Ogawa H., Muranaka S. et al., 1999, "New Combustion Concept for Ultra-Clean and High-Efficiency Small DI Diesel Engines", SAE Technical Paper 1999-01-3681, https://doi.org/10.4271/1999-01-3681.

[60] Mueller C.J., Upatnieks A., 2005, “Dilute clean diesel combustion achieves low emissions and high efficiency while avoiding control problems of HCCI”, US DOE, 11th Diesel Engine Emissions Reduction Conference (DEER), Chicago, IL, August 2005

[61] D’Ambrosio S., Ferrari A., 2015, “Effect of exhaust gas recirculation in diesel engines featuring late PCCI type combustion strategies”, Energy Conversion and Management, n. 105, pp. 1269–1280, https://doi.org/10.1016/j.enconman.2015.08.001

[62] Han D., Ickes A., Bohac S., Huang Z., Assanis D., 2012, “HC and CO emissions of premixed low-temperature combustion fueled by blends of diesel and gasoline”, Fuel, 2012, n. 99, pp. 13–19, https://doi.org/10.1016/j.fuel.2012.04.010

[63] Cheng X., Hu Y., Yan F., Chen L., Diong S., 2014, “Investigation of the combustion and emission characteristics of partially premixed compression ignition in a heavy-duty diesel engine”, Journal of Automotive Engineering, n. 228(7), pp. 784–798, https://doi.org/10.1177/0954407013513012

[64] Chung J., Min K., Oh S., Sunwoo M., 2016, “In-cylinder pressure based real-time combustion control for reduction of combustion dispersions in light-duty diesel engines”, Applied Thermal Engineering, n. 99, pp. 1183–1189, https://doi.org/10.1016/j.applthermaleng.2016.01.012

[65] Carlucci A., Laforgia D., Motz S., Saracino R., Wenzel S., 2014, “Advanced closed loop combustion control of a LTC diesel engine based on in-cylinder pressure signals”, Energy Conversion and Management, n. 77, pp. 193–207, https://doi.org/10.1016/j.enconman.2013.08.054

[66] Willems F., Doosje E., Engels F., and Seykens X., 2010, “Cylinder Pressure-Based Control in Heavy-Duty EGR Diesel Engines Using a Virtual Heat Release and Emission Sensor”, SAE Technical Paper 2010-01-0564, https://doi.org/10.4271/2010-01-0564.

[67] Yu S., Choi H., Cho S., 2013, “Development of engine control using the in-cylinder pressure signal in a high speed direct injection diesel engine”, International Journal of Automotive Technology, vol. 14, n. 2, p. 175, https://doi.org/10.1007/s12239-013-0019-x

[68] Dong T., Liu B., Zhang F., Wang Y., Wang B., Liu P., 2017, “Control oriented modeling and analysis of gas exchange and combustion processes for LTC diesel engine”, Applied Thermal Engineering, Vol. 110, pp. 1305-1314, https://doi.org/10.1016/j.applthermaleng.2016.09.001

[69] Yang F., Wang J., Gao G., Ouyang M., 2014, “In-cycle diesel low temperature combustion control based on SOC Detection”, Applied Energy, Vol. 136, pp. 77-88, https://doi.org/10.1016/j.apenergy.2014.09.014

[70] Hillion M., Chauvin J., Grondin O., Petit N., 2008, “Active Combustion Control of Diesel HCCI Engine: Combustion Timing”, SAE Technical Paper 2008-01-0984, https://doi.org/10.4271/2008-01-0984.

[71] Catania A.E., Finesso R., Spessa E., 2011, "Predictive Zero-Dimensional Combustion Model for DI Diesel Engine Feed-Forward Control", Energy Conversion and Management, Vol. 52, pp. 3159 3175, https://doi.org/10.1016/j.enconman.2011.05.003

[72] Finesso R., Spessa E., Yang Y., Alfieri V. et al., 2015, “HRR and MFB50 Estimation in a Euro 6 Diesel Engine by Means of Control-Oriented Predictive Models”, SAE Int. J. Engines, Vol. 8, pp. 1055-1068, https://doi.org/10.4271/2015-01-0879

[73] Baratta M., Finesso R., Misul D., Spessa E., 2015, "Comparison between Internal and External EGR Performance on a Heavy Duty Diesel Engine by Means of a Refined 1D Fluid-Dynamic Engine Model", SAE Int. J. Engines 8(5):1977-1992, https://doi.org/10.4271/2015-24-2389

[74] d’Ambrosio S., Iemmolo D., Mancarella A., Vitolo R., 2016, “Preliminary optimization of the PCCI combustion mode in a diesel engine through a design

of experiments," 71st Conference of the Italian Thermal Machines Engineering Association, ATI2016, September 14-16, 2016, Turin, Italy

[75] Spessa E., D'Ambrosio S., Iemmolo D., Mancarella A. et al., 2017 "Steady-State and Transient Operations of a Euro VI 3.0L HD Diesel Engine with Innovative Model-Based and Pressure-Based Combustion Control Techniques," SAE Int. J. Engines 10(3):1080-1092, 2017, https://doi.org/10.4271/2017-01-0695

[76] d'Ambrosio S., Iemmolo D., Mancarella A., Vitolo R., 2017, "Analisi sperimentale di una combustione diesel non convenzionale - Ottimizzazione mediante l'applicazione di tecniche statistiche", La Termotecnica - ISSN 0040-3725. LXXI(3), pp. 52-56.

[77] Brooks T., Lumsden G., Blaxill H., 2005, "Improving Base Engine Calibrations for Diesel Vehicles Through the Use of DoE and Optimization Techniques", SAE Technical Paper, 2005-01-3833, https://doi.org/10.4271/2005-01-3833

[78] Simpson T., Poplinski J., Koch P., Allen J.,2001, "Metamodels for computer-based engineering design: survey and recommendations", EWC (2001) 17: 129. https://doi.org/10.1007/PL00007198

[79] Montgomery D. C., 2000, "Design and Analysis of Experiments", Wiley, 5th Edition.

[80] Benajes J., Novella R., Pastor J., Hernández-López A., Hasegawa M., de Tsuji N., Emi M., Uehara J., Martorell J., Alonso M., 2016, "Optimization of the combustion system of a medium duty direct injection diesel engine by combining CFD modeling with experimental validation", Energy Conversion and Management, 2016, Volume 110, pp. 212-229, https://doi.org/10.1016/j.enconman.2015.12.010

[81] Kamimoto T., Bae M., 1988, "High Combustion Temperature for the Reduction of Particulate in Diesel Engines", SAE Technical Paper 880423, https://doi.org/10.4271/880423

[82] Kiplimo R., Tomita E., Kawahara N., Yokobe S., 2012, “Effects of spray impingement, injection parameters, and EGR on the combustion and emission characteristics of a PCCI diesel engine”, Applied Thermal Engineering, , n. 37, pp. 165-175, https://doi.org/10.1016/j.applthermaleng.2011.11.011

[83] Hardy W. L., Reltz R. D., 2006, “A study of the effects of high EGR, high equivalence ratio and mixing time on emissions levels in a heavy-duty diesel enginefor PCCI combustion”, SAE Technical Paper 0026, 2006, https://doi.org/10.4271/2006-01-0026

[84] Asad U., Zheng M., 2009, “Efficacy of EGR and boost in single-injection enabled low temperature combustion”, SAE paper 2009-01-1126, https://doi.org/10.4271/2009-01-1126

[85] Imarisio R., Peters B., Rossi Sebastiano G. M., Pinson J., Boretto G., Buratti R., 2004, “Diesel Strategies Towards Fuel Neutral European Emission Standards”, International Symposium Diesel Engine “The NOx & PM Emissions Challenge”, ATA paper no.04A5010, Monopoli (BA), 2004

[86] Northrop W., Bohac S., Chin J., Assanis D., 2011, “Comparison of filter smoke number and elemental carbon mass from partially premixed low temperature combustion in a direct-injection diesel engine”, ASME. J. Eng. Gas Turbines Power. 2011;133(10):102804-102804-6. doi:10.1115/1.4002918

[87] Box, George E. P., Cox, D. R., 1964, "An analysis of transformations", Journal of the Royal Statistical Society, Series B 26 (2) 211-252

[88] Finesso R., Marello O., Spessa E., Yang Y, Hardy G., 2017, “Development and assessment of pressure-based and model-based techniques for the MFB50 control of a Euro VI 3.0L diesel engine”, SAE Int. J. Engines 10(4):1538-1555, https://doi.org/10.4271/2017-01-0794

[89] D'Ambrosio S., Iemmolo D., Mancarella A., Salamone N. et al., 2017, "Zero Dimensional Models for EGR Mass-Rate and EGR Unbalance Estimation in Diesel Engines", SAE Technical Paper 2017-24-0070